

Advanced Silicon-based Electrodes for Rechargeable Lithium-ion Batteries

by

Kun Feng

A thesis

presented to the University of Waterloo

in fulfillment of the

thesis requirement for the degree of

Doctor of Philosophy

in

Chemical Engineering (Nanotechnology)

Waterloo, Ontario, Canada, 2018

© Kun Feng 2018

Examining Committee Membership

The following served on the Examining Committee for this thesis. The decision of the Examining Committee is by majority vote.

External Examiner	Dr. Christina Bock
	Research Officer
Supervisor	Dr. Zhongwei Chen
	Professor
Internal Member	Dr. Eric Croiset
	Professor, PEng
Internal Member	Dr. Ali Elkamel
	Professor
Internal-external Member	Dr. Bo Cui
	Professor

Author's Declaration

This thesis consists of material all of which I authored or co-authored: see Statement of Contributions included in the thesis. This is a true copy of the thesis, including any required final revisions, as accepted by my examiners.

I understand that my thesis may be made electronically available to the public.

Statement of Contributions

This thesis is based upon a combination of published work and manuscript under submission.

Various chapters are adapted from the following list of published work, with specific reference to the published work provided within the chapter.

K. Feng, M. Li, Y. Zhang, W. Liu, A. G. Kashkooli, X. Xiao, Z. Chen, Micron-Sized Secondary Si/C Composite with In Situ Crosslinked Polymeric Binder for High-Energy-Density Lithium-ion Battery Anode.

K. Feng, M. Li, H. W. Park, W. Liu, A. G. Kashkooli, X. Xiao, Z. Chen, Conformal Formation of Carbon-TiO_x Matrix Encapsulating Silicon for High-performance Lithium-ion Battery Anode.

K. Feng, M. Li, W. Liu, A. G. Kashkooli, X. Xiao, M. Cai, Z. Chen, Silicon-based Anodes for Lithium-ion Batteries: From Fundamentals to Practical Applications. *Small* **14**, 1702737 (2018)

K. Feng, W. Ahn, G. Lui, H. Park, A. Kashkooli, G. Jiang, X. Wang, X. Xiao, Z. Chen. Implementing an In-situ Carbon Network in Si/reduced Graphene Oxide for High Performance Lithium-ion Battery Anodes. *Nano Energy* **19**, 187-197 (2016)

Abstract

The pressing environmental and ecological issues with fossil fuels, together with their long-term unsustainability have driven a mighty quest for alternative energy sources. High-performance and reliable energy conversion and storage systems play a key role in the practical application of renewable energies. Among all the current energy conversion and storage technologies, lithium ion batteries (LIBs) have successfully dominated the consumer electronics market. In addition, LIBs have also been found in the application of transportation sector such as electric bicycles, various types of electric vehicles (EVs), and even in multi-megawatt-hour systems for the utility industry. However, the state-of-art commercial LIBs are still infeasible for widespread deployment in EVs due to their energy density limit and high cost for large battery packs.

To increase the energy density of LIBs, which represents the ultimate objective of this thesis, traditional electrode materials need to be replaced by new materials with higher capacity and as-reliable performance. Silicon (Si) has been intensively studied as the anode material for LIBs because of its exceptionally high specific capacity. Compared to the widely commercialized graphite anode which displays a capacity of 372 mAh g^{-1} , Si possesses a theoretical capacity of 4200 mAh g^{-1} upon full lithiation with the formation of lithium Si alloy $\text{Li}_{22}\text{Si}_5$. However, Si-based anode materials usually suffer from large volume change during the charge and discharge process, leading to the subsequent pulverization of Si, loss of electric contact, and continuous side reactions. These transformations cause poor cycle life and hinder the wide commercialization of Si for LIBs. The lithiation/delithiation behaviors of Si, as well

as the interphase reaction mechanisms, have been progressively studied and understood. Various nanostructured Si anodes have been reported to exhibit both superior specific capacity and cycle life compared to commercial carbon-based anodes. However, some practical issues with Si anodes remain and must be addressed if to be widely used in commercial LIBs.

To tackle the practical challenges facing Si anodes and achieve our objective of boosting the energy density of LIBs, several feasible approaches have been proposed, and specifically embodied in the projects displayed in this thesis. Main considerations behind these approaches include: preventing Si structure failure, enhancing electronic conductivity, forming stable electrode/electrolyte interphase. This thesis will begin with an overview on current energy challenges and motivations, followed by thesis objective and approaches. A comprehensive literature review is presented on LIB technology fundamentals, key components, and more importantly, peer works on the lithiation/delithiation behaviors of Si, research focuses on Si anode development, including engineering of Si architectures, and construction of Si-based composites. Chapter 3 introduces several important characterization techniques that are used throughout the completion of thesis projects, including both physical and electrochemical characterizations, and device assembly methods.

In the first study, a highly efficient Si reduced graphene oxide carbon (Si-rGO-C) composite with good rGO wrapping of Si and an interconnected carbon network is developed for the first time. Adoption of Si NPs eliminates the possibility of Si structure failure. Compared with the regular Si-rGO composites with only Si NPs wrapped by rGO that have been previously reported, Si-rGO-C composite not only improves the electrical conductivity, but

also enhances structure stability. In addition to the rGO wrapping on Si NPs, the additional carbon coating on the partially exposed Si NPs provides extra protection from Si volume change that may cause detachment from rGO sheets. Carbon rods between Si-rGO flakes function as conductive bridges, creating an effective conductive network on a larger scale. The initial capacity of Si-rGO-C composite reaches 1139 mAh g⁻¹ at 0.1 A g⁻¹, many times that of graphite. In addition, capacity retention of 94% is obtained after 300 cycles at 1 C.

In the second study, a secondary micron-sized Si-based composite (MSC) is developed, with Si NPs embedded in a porous, conductive and elastic network constructed with carbon, and cured-and-crosslinked functional binder materials. The idea of combining nano-sized Si and conductive agents is extended to the construction of a well-defined spherical structure via a facile spray-drying process. With the careful heat treatment of the composite, the polymers crosslink via the dehydration reaction of functional groups and forms a robust structure. The polymeric chains are retained in the structure since a relatively mild temperature (250 °C) is selected. In addition to the structure benefits of this composite and therefore the electrochemical performance improvement over Si NPs, tap density of Si NPs is significantly improved via the formation of secondary micron-sized particles, eventually promoting the volumetric energy density of a LIB. More importantly, this facile methodology does not require a high temperature carbonization and is implemented with a highly scalable spray-drying process.

In the last study, a secondary cluster with Si NPs embedded in an amorphous carbon and TiO_x matrix (C-TiO_x/Si) is developed. This project is in furtherance of the ideas adopted in the

previous two projects, as it integrates Si NPs onto a secondary conductive network, while a better surface coating on Si is adopted for enhanced surface protection. In this project, the C-TiO_x matrix is conformally formed on the surface of Si, which not only uniformly casts a protective layer on Si, but also combines nano-sized Si into micron clusters. Thickness of the coating layer can be easily tuned, and thus a good coating quality and cluster size can be readily achieved. The amorphous and defect-rich nature of the TiO_x not only exhibits enhanced electronic conductivity over its crystalline counterparts, but also provides better elasticity and stress-release capability that can maintain the structural integrity over lithiation/delithiation of Si. The conformally-formed C-TiO_x matrix protects Si from direct and repetitive contact with electrolyte and help form a stable solid electrolyte interphase on the outer surface of the cluster.

The final chapter concludes the work in this thesis and provides recommendations for future research directions based on the scientific findings and experience gained through the completion of this thesis.

Acknowledgements

First and foremost, I would like to thank my supervisor, Professor Zhongwei Chen, for his consistent support and encouragement throughout my graduate studies. It is truly my honor to be one of your students and working closely with you on those interesting and important projects. I would also like to thank all the outstanding colleagues I have met in Chen Lab, as well as at the University of Waterloo for precious discussions, generous sharing of ideas, and many other forms of support.

I also appreciate Doctor Xingcheng Xiao, Staff Scientist at the General Motors Global Research and Development Center, for the kind guidance and valuable discussions on my projects.

I would also like to thank my Ph.D. thesis examination committee, including Professor Ali Elkamel, Professor Eric Croiset, and Professor Bo Cui from the University of Waterloo, and Doctor Christina Bock as my external examiner from National Research Council Canada for their time and contributions through this important process.

I would also like to express my sincere gratitude towards my parents for their unconditional sacrifice, and support for my decision to explore the bigger world and pursue my Ph.D. degree without too much burden or distraction. I would not have been able to make it without your precious love.

Finally, I would like to acknowledge the department of Chemical Engineering, the Waterloo Institute for Nanotechnology, and the University of Waterloo for the excellent

opportunities they have provided. I am very grateful for all their kind support and funding during my Ph.D. study, which allowed me to stay focused on my research.

Table of Contents

Examining Committee Membership	ii
Author's Declaration.....	iii
Statement of Contributions	iv
Abstract.....	v
Acknowledgements.....	ix
Table of Contents	xi
List of Figures	xiv
List of Tables.....	xviii
List of Abbreviations.....	xix
1. Introduction.....	1
1.1 The Energy Challenges and Motivations.....	1
1.2 Thesis Objective and Approaches.....	4
1.3 Thesis Outline.....	5
2. Background and Literature Review on Li-ion Batteries and Si-based Anodes	7
2.1 Li-ion Battery Fundamentals	7
2.2 Key Components in Li-ion Batteries	11
2.2.1 Anodes	11
2.2.2 Cathodes.....	15
2.2.3 Electrolytes	18
2.2.4 Binders	20
2.3 Background and Literature Review on Si-based Anodes	21
2.3.1 Reaction Mechanisms, Challenges, and Prospects of Si-based Anodes	21
2.3.2 Development of Si Morphologies	24
2.3.3 Development of Si-based Composites	26
3. Characterization Techniques	31
3.1 Physical Characterization Techniques	31
3.1.1 Scanning Electron Microscopy (SEM)	31

3.1.2	<i>Transmission Electron Microscopy (TEM)</i>	31
3.1.3	<i>Energy Dispersive X-ray Spectroscopy (EDX)</i>	32
3.1.4	<i>X-ray Diffraction (XRD)</i>	32
3.1.5	<i>X-ray Photoelectron Spectroscopy (XPS)</i>	33
3.1.6	<i>Raman Spectroscopy</i>	33
3.1.7	<i>Thermogravimetric Analysis (TGA)</i>	35
3.1.8	<i>Surface Area and Pore Analysis</i>	35
3.2	Electrochemical Evaluations	36
3.3	Full Cell Electrochemical Analyses.....	38
4.	Construction of Graphene-based Carbon Network Containing Si NPs	39
4.1	Introduction	39
4.2	Experimental Methods.....	41
4.2.1	<i>Material Synthesis</i>	41
4.2.2	<i>Physical Characterizations</i>	42
4.2.3	<i>Electrochemical Measurements</i>	43
4.3	Results and Discussions	44
4.4	Summary.....	58
5.	Formation of Micron-sized Spherical Particles from Si NPs.....	60
5.1	Introduction	60
5.2	Experimental Methods.....	61
5.2.1	<i>Material Synthesis:</i>	61
5.2.2	<i>Physical Characterizations:</i>	62
5.2.3	<i>Electrochemical Measurements:</i>	63
5.3	Results and Discussions	64
5.4	Summary.....	86
6.	Engineering a Core-shell Structure with Si Core and Amorphous C-TiO _x as Shell and Support Matrix.....	88
6.1	Introduction	88
6.2	Experimental Methods.....	90

6.2.1	<i>Material Synthesis:</i>	90
6.2.2	<i>Physical Characterization:</i>	91
6.2.3	<i>Electrochemical Measurements:</i>	91
6.3	Results and Discussions	92
6.4	Summary.....	107
7.	Conclusions and Suggestions.....	109
7.1	Conclusions	109
7.2	Recommendations	111
	References.....	113

List of Figures

Figure 1.1 a) World energy consumption by energy source in quadrillion Btu from the U.S. Energy Information Administration, b) Total U.S. greenhouse gas emissions by economic sector in 2015 from the U.S. Environmental Protection Agency.	2
Figure 2.1 Gravimetric and volumetric energy densities of several popular energy storage technologies..	8
Figure 2.2 A schematic diagram of a conventional LIB with Li metal oxide as cathode and carbon as anode. During charge, Li ions are extracted from the cathode and inserted into the anode. Whereas discharge is the reversed process of charging..	10
Figure 2.3 Crystal structure of hexagonal graphite showing the ABAB... stacking of graphene sheets and the unit cell..	13
Figure 2.4 Important formulae, structures and voltage profiles during discharge of various Li-ion battery cathodes, with all potentials versus Li reference electrodes.....	17
Figure 2.5 a) Pristine Si nanowire with rough sidewalls due to faceting, b) Partially lithiated Si nanowire with an a-Li _x Si layer surrounding the c-Si core..	22
Figure 3.1 Breakdown of a coin-type 2032 LIB cell.	36
Figure 4.1 Schematic illustration of the synthesis procedure of Si-rGO-C composite.....	41
Figure 4.2 (a) Optical images of Si-GO mixture before (left) and after (right) freeze-drying process. (b) TGA curves of Si-rGO composite with and without additional carbon coating. (c) XRD data of the as-obtained Si-rGO-C composite. (d) Raman spectra of D bands and G bands from Si-GO and Si-rGO-C composites.....	45
Figure 4.3 SEM images of a typical site of Si-rGO-C composite with a whole piece of rGO flake(a), a close view of Si-rGO-C composite including branched carbon with Si NPs wrapped with rGO sheets (b), a typical site of Si-rGO composite (c), and Si-rGO composite with higher magnification (d).....	47
Figure 4.4 (a) TEM image of Si-rGO-C composite at low magnification with the grid of TEM holder in view. (b) A zoomed-in TEM image of (a) with detailed features of Si-rGO-C. (c) Dark field TEM image of Si-rGO-C composite with higher resolution, (d) EDX mapping of element	

Si for the area marked in (c), (e) EDX mapping of element C for the area marked in (c), and (f) HRTEM image of Si-rGO-C composite with insets of increased magnification TEM image and FFT pattern of the selected area.	49
Figure 4.5 XPS spectra of C (a, b, and c) and Si (d, e, and f) for Si-GO (a and d), Si-rGO (b and e), and Si-rGO-C (c and f) composites.....	51
Figure 4.6 Charge and discharge profiles of Si-rGO-C (a) and Si-rGO (b) of first three cycles.	52
Figure 4.7 (a) CV test of the Si-rGO-C composite with 1st, 3rd, 6th and 8th cycles shown. (b) Cycling performance of Si-rGO-C, Si-rGO composites, and bare Si at 0.2C following activation. (c) Rate capability tests for Si-rGO-C and Si-rGO composites. (d) Long-term cycling performance of Si-rGO-C composite at 1C following activation.	53
Figure 4.8 (a) Impedance measurements for Si-rGO-C and Si-rGO composites after 1st and 100th discharges, (b) The equivalent circuit model.	57
Figure 5.1 a) Schematic illustration of the formation process of MSC250. b-d) SEM images of MSC250 at different magnifications. e) TEM image of MSC250. f-g) C and Si elemental mapping of the area from inset in e). h) TEM image of the edge of MSC250. i) HRTEM image of a single Si NP in MSC250, with FFT inset of the core area.....	65
Figure 5.2 Photograph of MSC250 and Si NPs with same mass of 1.8 g.	67
Figure 5.3 a and b) SEM images of Si NPs at different magnifications. c-d) TEM image Si NPs mixed with other precursors via simple mixing, and HRTEM image of a single Si NP.....	68
Figure 5.4 a) XRD patterns of MSC250 and Si NPs. b) TGA curves of MSC250, MSC200, and MSC900. c) DSC curves of MSC250, MSC200, and MSC900. d) FTIR spectra of raw polymer binders and MSC250.....	69
Figure 5.5 a) TGA curve of CMC/PAA mixture in air. b) TGA curves of MSC250, MSC200, and the corresponding derivative weight loss data.	71
Figure 5.6 Raman spectra of Si NPs, MSC250, MSC200, and MSC900.....	72
Figure 5.7 Nitrogen isotherm adsorption/desorption curves and pore size distribution graphs of Si NP (a, d), MSC250 (b, e), and MSC900 (c, f).....	73
Figure 5.8 XPS spectra of C and Si in MSC250 (a-b) and MSC900 (c-d).....	75

Figure 5.9 CV curves of first five cycles from a MSC250/Li half cell.	76
Figure 5.10 a) Charge and discharge profiles of MSC250 cell for the first three cycles. b) Charge and discharge profiles of MSC250 cell at current densities of 0.1 C, 0.2 C, 0.5 C, 1 C, 2 C, and 5 C. c) Comparison of rate capabilities of MSC250 and MSC200 cells. d) Cycling performance at 0.5 C and CE data of MSC250 for 500 cycles.....	77
Figure 5.11 First three cycles charge discharge curves of a) MSC200, and b) MSC900.	78
Figure 5.12 Long-term cycling test of MSC250 at 1C, with CE plot.....	79
Figure 5.13 Cycling performance of MSC200 and MSC900 at 0.5 C for 200 cycles, with CE plots.....	80
Figure 5.14 a) A plausible illustration of lithiation process of a MSC250 sphere. EIS spectra of MSC250, MSC200, and MSC900 electrodes, b) after first 1st charge, and c) after 100th charge.	81
Figure 5.15 SEM, STEM images, and elemental mapping graphs of C, O, Si and F of a MSC250 particle after 100 cycles.	82
Figure 5.16 a) Charge and discharge profiles of Li/NMC cell, with specific capacity as X-axis. b) Charge and discharge profiles of graphite/NMC cell, with areal energy density as X-axis. c) Charge and discharge profiles of MSC250/NMC cell, with areal energy density as X-axis. d) Cycling performance of MSC250/NMC full cell for 100 cycles at 0.1 C.	85
Figure 5.17 Charge/discharge curves of MSC250/NMC cell at current densities from 0.1 C to 1 C.....	86
Figure 6.1 Schematic illustration of synthetic procedure of C-TiO _x /Si.	92
Figure 6.2 a-c) C-TiO _x /Si cluster at magnifications of 20,000X, 50,000X, and 100,000X, respectively. d) TEM image with focus on a single Si NP on C-TiO _x /Si, e-f) C, O, Si, and Ti elemental mappings of the highlighted area in d).....	93
Figure 6.3 a-c) TEM images TiO _x /Si composites synthesized with initial TBOT:Si mass ratios of 4:1, 2:1, and 1:1, respectively.	94
Figure 6.4 SEM images of TiO _x /Si with initial TBOT:Si mass ratio of 4:1.....	95
Figure 6.5 SEM images of TiO _x /Si with initial TBOT:Si mass ratio of 1:1.....	95
Figure 6.6 SEM images of TiO _x /Si with initial TBOT:Si mass ratio of 2:1, without reflux...	95

Figure 6.7 a) XRD patterns of Si, C-TiO ₂ /Si, and C-TiO _x /Si, b) Ti 2p high-resolution XPS spectra of C-TiO _x /Si and anatase TiO ₂ , c) O 1s high-resolution XPS spectrum of C-TiO _x /Si, d) TGA graphs of C/Si, C-TiO ₂ /Si, and C-TiO _x /Si, e) nitrogen sorption isotherms of Si and C-TiO _x /Si.	96
Figure 6.8 XRD patterns of anatase TiO ₂ , TiO ₂ /Si, and TiO _x /Si after heat treatment at 800 °C.	97
Figure 6.9 TGA graph of TiO _x	98
Figure 6.10 Photographs of C-TiO _x /Si and Si NPs with same mass 0.4 g of materials after same condition of mechanical tapping.	99
Figure 6.11 Voltage profiles of a) C-TiO _x /Si and b) C-TiO ₂ /Si for first three cycles at a rate of 0.1 A g ⁻¹ . c) Cycling performance of C-TiO ₂ /Si and C-TiO _x /Si at 1 A g ⁻¹ . d) Rate capability performance of C-TiO ₂ /Si and C-TiO _x /Si at current densities of 0.1, 0.2, 0.5, 1, 2, 5, and 1 A g ⁻¹	102
Figure 6.12 a) Voltage profiles of C/Si for first three cycles in the voltage window of 0.05-1.5V at a rate of 0.1 A g ⁻¹ . b) Cycling performance of C/Si at 1 A g ⁻¹ after 5 cycles at 0.1 A g ⁻¹ ...	103
Figure 6.13 a) TEM of a C-TiO _x /Si cluster after cycling, b-f) Elemental mappings of C, O, Si, Ti, and F of the area in a), respectively.	106

List of Tables

Table 1.1 USABC goals for advanced batteries for EVs - CY 2020 commercialization.....	4
Table 2.1 List of different anode materials for Li-ion batteries.	15
Table 2.2 Several popular commercial cathode materials with their properties, adapted from Li-ion batteries: Science and Technologies.	17
Table 2.3 Electrochemical performances and characteristics of some representative Si anode materials.....	29
Table 4.1: Impedance parameters for Si-rGO-C and Si-rGO electrodes after 1st and 100th cycles.....	58
Table 5.1 BET surface areas and BJH pore volumes of Si NPs, MSC250, and MSC900.....	72

List of Abbreviations

LIBs	Lithium-ion batteries/Li-ion batteries
SEM	Scanning electron microscopy
TEM	Transmission electron microscopy
XRD	X-ray diffraction
XPS	X-ray photoelectron spectroscopy
TGA	Thermal gravimetric analysis
CNT	Carbon nanotube
CVD	Chemical vapor deposition
EDX	Energy dispersive X-ray spectroscopy
SAED	Selected area electron diffraction
FFT	Fast Fourier transform
BET	Brunauer–Emmett–Teller
BJH	Barrett-Joyner-Halenda
CV	Cyclic voltammetry
EIS	Electrochemical impedance spectroscopy
NMP	N-Methyl-2-pyrrolidone
NWs	Nanowires
NPs	Nano particles
SEI	Solid electrolyte interphase
3D	Three dimensional

EC	Ethylene carbonate
DEC	Diethyl carbonate
DMC	Dimethyl carbonate
FEC	Fluoroethylene carbonate
VC	Vinylene carbonate
PVDF	Polyvinylidene fluoride
Si-rGO	Silicon reduced graphene oxide
Si-rGO-C	Silicon reduced graphene oxide and carbon composite
GO	Graphene oxide
rGO	Reduced graphene oxide
MSC	Micron-sized secondary composite
CMC	Carboxymethyl cellulose
PAA	Polyacrylic acid
SBR	Styrene-butadiene rubber

1. Introduction

1.1 The Energy Challenges and Motivations

Mankind's high dependence on non-renewable energy has led to increasing concerns on environment, climate, and human health. According to the *International Energy Outlook (2017)* published by the U.S. Energy Information Administration, fossil fuels will continue dominating the world energy consumption in the next two decades, with petroleum and other liquid fuels being the largest energy source over the surveyed period of 1990-2040 (**Figure 1.1a**).¹ The U.S. Environmental Protection Agency summarizes that the transportation sector is one of the largest contributors in greenhouse gas emissions (Figure 1.1b).² Heavy reliance of the current transportation sector on petroleum fuels will result in further increase in greenhouse gas emission and air pollution issues. Meanwhile, the research and development on clean energy is becoming one of the prime topics of interest around the globe. On the one hand, clean energy from solar and wind has seen growing market size worldwide, leading to a strong demand for highly efficient energy conversion and storage devices for the wide utilization of clean energies. On the other hand, significant efforts have been devoted to the electrification of vehicles to reduce the reliance on petroleum, while correspondingly suitable energy storages devices are still under probe.

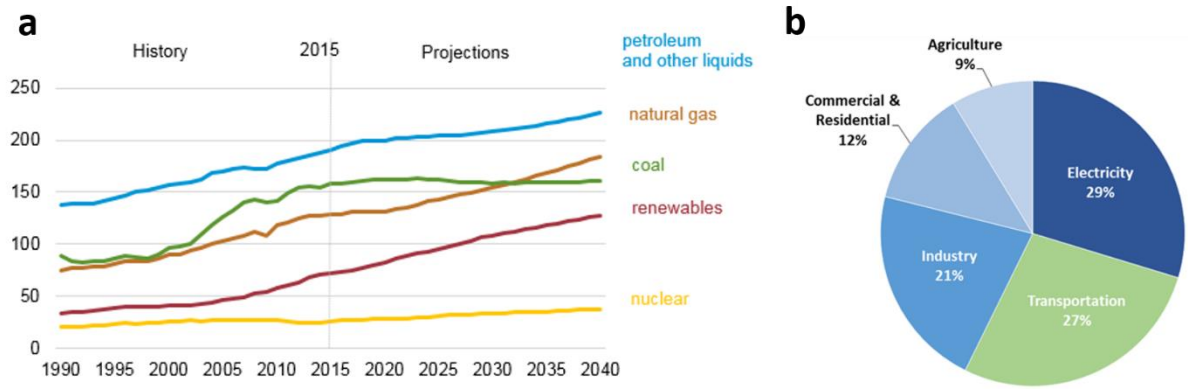


Figure 1.1 a) World energy consumption by energy source in quadrillion Btu from the U.S. Energy Information Administration,¹ b) Total U.S. greenhouse gas emissions by economic sector in 2015 from the U.S. Environmental Protection Agency.²

Lithium-ion batteries (LIBs) have been adopted as the major energy storage technology for portable electronic devices and are also being considered for vastly different markets such as grid scale energy storage. Owing to their environmental benignity, relatively high energy density and stable performance, LIBs have found application across multiple industries and largely substituted previous battery technologies such as lead acid, nickel cadmium, and nickel metal hydride batteries in many areas.^{3, 4} In the case of electric vehicles (EVs), the market size of LIBs can potentially surpass that of portable electronics. However, most EVs are not yet competent enough to replace traditional vehicles simply because of their impractically low driving ranges and high costs. The range from a single charge is dependent on the size/energy density of the battery. Increasing the size of the integrated battery not only increases the cost of an EV but also increases the mass of the whole electric vehicle, which in turn lowers the range. This dependence loop between cost, driving range, battery size and total vehicle mass introduces an optimization problem and strongly depends on the system design of EVs. EVs

with near practical ranges do exist in the market, but the high cost from the large battery pack typically renders these vehicles too expensive. In this regard, batteries with higher energy and power density, lower cost, and improved safety are in great demand. As shown in **Figure 1.2** according to the goal set by USABC (U.S. Advanced Battery Consortium LLC) to address the issue,⁵ energy density of a LIB pack system has to reach 235 Wh kg⁻¹ or 500 Wh L⁻¹ at a discharge rate of 1/3 C (1/3 C discharge rate indicates that a battery can be fully discharged in 3 hours)⁶, in addition to the requirement of 15 years' calendar life and up to 1000 cycles. These requirements and practical needs in real applications have limited the chemistry selection of current commercially available LIBs to the marginally sufficient graphite vs. Li transition metal oxides cells. Therefore, new electrode materials and chemistry that can provide drastically higher energy density and excellent cycle stability are crucial to the adaptation of next generation batteries into the EV market and beyond.

Table 1.1 USABC goals for advanced batteries for EVs - CY 2020 commercialization.⁵

End of Life Characteristics at 30°C	Units	System Level	Cell Level
Peak Discharge Power Density, 30 s Pulse	W/L	1000	1500
Peak Specific Discharge Power, 30 s Pulse	W/kg	470	700
Peak Specific Regen Power, 10 s Pulse	W/kg	200	300
Useable Energy Density @ C/3 Discharge Rate	Wh/L	500	750
Useable Specific Energy @ C/3 Discharge Rate	Wh/kg	235	350
Useable Energy @ C/3 Discharge Rate	kWh	45	N/A
Calendar Life	Years	15	15
DST Cycle Life	Cycles	1000	1000
Selling Price @ 100K units	\$/kWh	125	100
Operating Environment	°C	-30 to +52	-30 to +52
Normal Recharge Time	Hours	< 7 Hours, J1772	< 7 Hours, J1772
High Rate Charge	Minutes	80% ΔSOC in 15 min	80% ΔSOC in 15 min
Maximum Operating Voltage	V	420	N/A
Minimum Operating Voltage	V	220	N/A
Peak Current, 30 s	A	400	400
Unassisted Operating at Low Temperature	%	> 70% Useable Energy @ C/3 Discharge rate at -20 °C	> 70% Useable Energy @ C/3 Discharge rate at -20 °C
Survival Temperature Range, 24 Hr	°C	-40 to+ 66	-40 to+ 66
Maximum Self-discharge	%/month	< 1	< 1

1.2 Thesis Objective and Approaches

The ultimate objective of this thesis is to develop advanced electrodes to boost the energy density of rechargeable Li-ion batteries. In an attempt to increase the capacity on the anode side, silicon-based materials have been investigated owing to its extraordinarily high capacity. Compared to the widely used graphite anodes (372 mAh g⁻¹), silicon (Si) has a theoretical specific capacity of around 4200 mAh g⁻¹.⁷ In addition, Si's high natural abundance, environmental compatibility, low working potential (0-0.4 V vs. Li/Li⁺), and high maturity of manufacturing all make it highly desirable as an anode material for LIBs.^{8,9} However, bare Si electrodes suffer from rapid capacity loss upon cycling mainly due to the huge volume change

of Si and associated detrimental effects during charge and discharge, making it impossible for direct use in commercial batteries.

In order to circumvent the intrinsic drawbacks of Si and develop stable Si-based electrodes, Si must be carefully tailored or composited with other materials. The following strategies have been employed in this thesis for the improvement of electrode performance:

1. Adopting nanotechnology;
2. Introducing graphene and carbon nanotubes and organically integrate with Si;
3. Constructing a conductive and robust structure as a host for Si; and,
4. Forming a protective shell and matrix for Si.

1.3 Thesis Outline

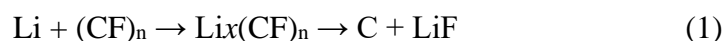
This thesis consists of 7 chapters. As already seen, this chapter introduces the energy situation and motivation, thesis objectives and approaches, and outlines the overall structure of the thesis. Chapter 2 provides a detailed background and literature review on Li-ion batteries, with focus on Si anodes and related researches. Chapter 3 provides background information on various physical and electrochemical characterization techniques, device assembly and testing protocols that have been applied throughout the thesis projects completion. Chapter 4 introduces the research on the combination of Si and reduced graphene oxide (rGO). Si NPs are first wrapped by rGO, which possesses an extraordinary in-plane electronic conductivity. An in situ formed carbon network interconnects Si/rGO flakes and contributes to the stable cycling of the final electrode. Chapter 5 highlights the development of micron-sized secondary sphere originating from Si NPs. The sphere is consisted of a conductive and robust network

formed by conductive carbon sources and cured and crosslinked polymer binders. Si NPs are secured inside the secondary sphere during lithiation/delithiation process, avoiding breaking away from the conductive network over cycling. Chapter 6 focuses on the development of a core-shell structure with Si NPs acting as core, and amorphous carbon and titanium oxide layer acting as shell and supporting matrix. The shell structure not only acts as a protective layer against growth of unstable solid electrolyte interphase (SEI) on Si, but also effectively encapsulates Si inside the secondary cluster for better structural integrity and more continuous conductive paths. Finally, Chapter 7 concludes all the work presented in the thesis, and provides recommendations for future research direction to advance the development of Si-based anodes towards practical applications.

2. Background and Literature Review on Li-ion Batteries and Si-based Anodes

2.1 Li-ion Battery Fundamentals

The concept of Li batteries can be dated back to 1970s, when Matsuchita Electric developed the $\text{Li}/(\text{CF})_n$ battery,¹⁰ which undergoes the reaction mechanism shown in Equation (1):



Since then, the reactivity of Li with many elements has been surveyed and a variety of Li primary batteries were developed, including Li/iodine and Li/MnO₂ cells.¹¹ Molten salt systems using Li were major attempts for rechargeable Li batteries at early stages. Molten Li and molten sulfur were used as anode and cathode, respectively, as the earliest Li sulfur batteries. Later, Li metal alloys such as LiAl, and metal sulfides including FeS replaced molten Li and sulfur due to the latter's harsh requirement on reaction conditions and equipment. During the 1970s and 1980s, with the development of intercalation chemistry for example, Li intercalation in the layered dichalcogenides, trichalcogenides and related derivatives, and layered oxides, more feasible rechargeable Li batteries were created.¹²⁻¹⁴ Wide commercialization of modern Li-ion batteries took place after Sony combined the LiCoO₂ cathode and a carbon anode in 1991.¹⁵ The combination of LiCoO₂ and carbon is still commonly used in current LIBs. Since 1990s, more Li metal oxides, such as spinel-structured LiMn₂O₄, olivine-structured LiFePO₄, layered oxides with blend metals like LiNiMnCoO₂ were developed and adopted in different types of LIBs to meet various demands.¹⁶⁻¹⁸ In the meantime, various carbon materials (graphite, hard carbon, and soft carbon,) have been found

to be suitable as LIB anodes with advantages including high abundance, low cost, and stable performance.^{19, 20}

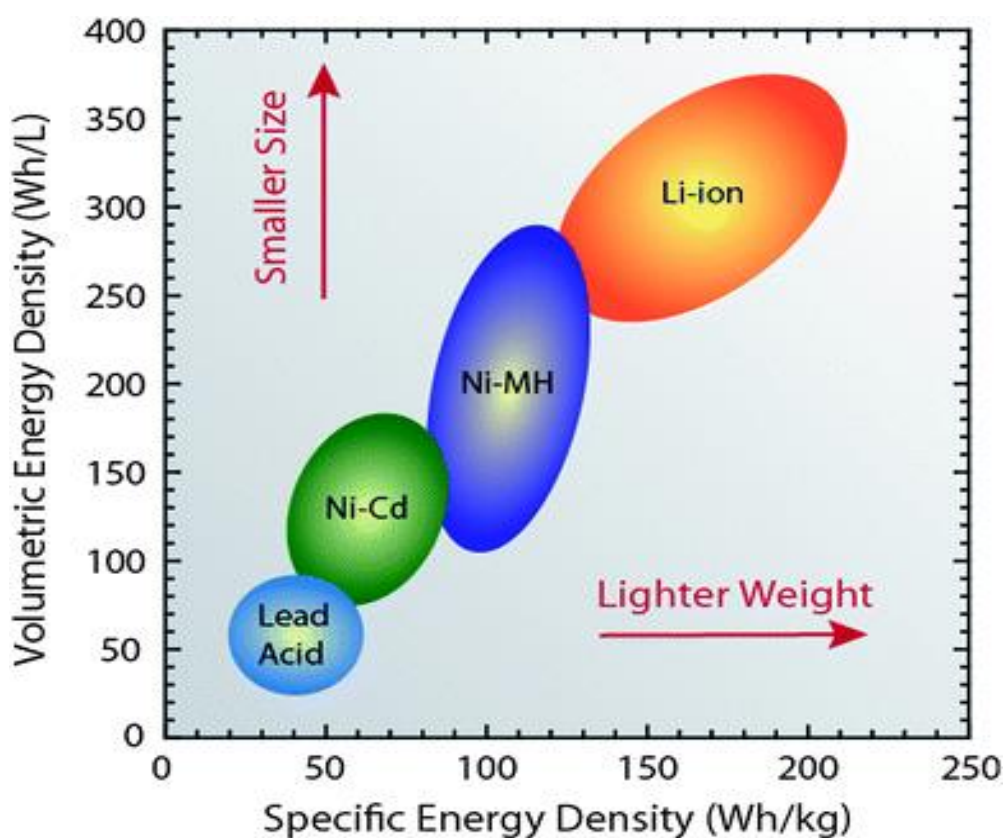


Figure 2.1 Gravimetric and volumetric energy densities of several popular energy storage technologies.²¹ Reprinted with permission from Nature Publishing Group.

Li is the lightest metal in the world (Atomic mass of Li is 6.94, and its density is 0.53 g cm^{-3}). In addition, Li has the highest electropositive potential (-3.04 V versus standard hydrogen electrode). These characteristics promote the status of Li in electrochemical energy storage as it can facilitate the design of batteries with extraordinary high energy densities.²¹ **Figure 2.1** compares the specific gravimetric energy densities and specific volumetric energy densities of several popular rechargeable battery technologies. The general goal of LIB research is to push the limit of LIBs to the upper right corner of the chart. Applications of LIBs, including portable

electronic devices, especially electric vehicles, are extremely demanding in energy density for their energy storage systems. Improvements of LIB energy density will require weight reduction on components in batteries.

Figure 2.2 is a schematic representation of the composition and operation of a typical LIB. A LIB typically consists of an anode with relatively low electrode potential vs. Li^+/Li , a cathode with high electrode potential, both of which soaked in a Li-ion rich electrolyte and separated by an electron-insulating and Li-ion permeable separator. Graphite and other carbon materials are the most widely used anode materials for LIBs due to their high abundance, low cost, and stable performance in Li storage. Common cathode materials include Li metal oxides (LiCoO_2 , LiMn_2O_4 , LiNiMnCoO_2), Li metal phosphates (LiFePO_4), etc. Like graphite anodes, the above cathode materials also undergo reversible intercalation or insertion reactions during the charge and discharge process in LIBs. Most commercial LIBs vastly contain electrolytes that consist of Li salts dissolved in aprotic solvents. For example, a common electrolyte consists of a solution of Li hexafluorophosphate (LiPF_6) dissolved in carbonate-based solvents such as a mixture of ethylene carbonate (EC) and dimethyl carbonate (DMC). Separator is a layer of Li-ion permeable membrane that prevents the direct contact between anode and cathode. While the separator and electrolyte are important components of a cell, research and development in electrode materials bear more practical significance because the major cost and weight of a LIB stem from the electrodes. In addition, performance of a LIB is largely dominated by the quality of electrodes. A capacity increase in anode and cathode can thus contribute to an overall increase in LIB's energy density, decrease the required mass/volume of battery pack, and allow for the crucial wide deployment of LIBs in vehicles.

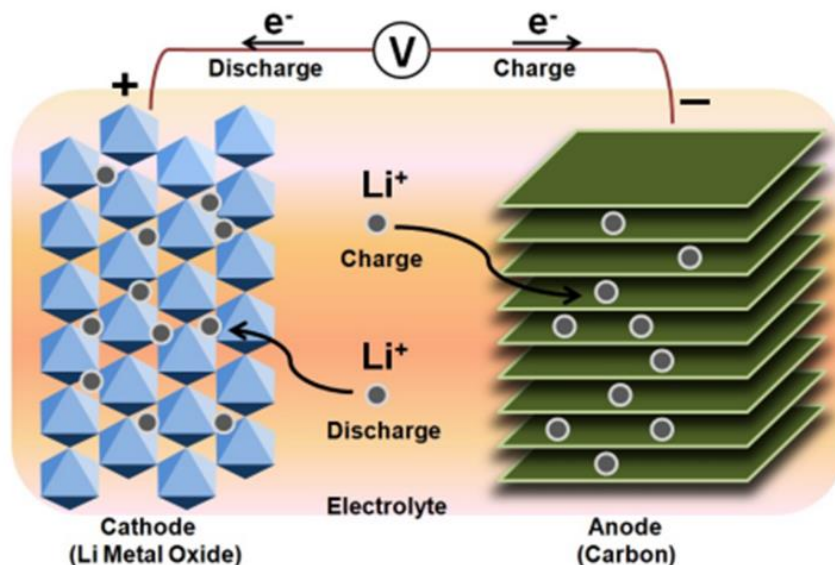
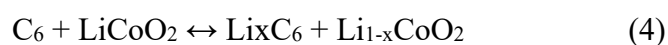
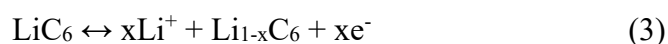
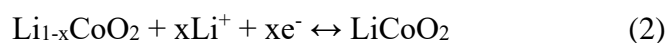


Figure 2.2 A schematic diagram of a conventional LIB with Li metal oxide as cathode and carbon as anode. During charge, Li ions are extracted from the cathode and inserted into the anode. Whereas discharge is the reversed process of charging.⁸ Reprinted with permission from Wiley.

During charging, Li ions are extracted from the cathode and inserted into the anode. Battery voltage rises and electrical energy is transformed to chemical energy. Discharge is the reverse process, during which the chemical energy is released as electricity, powering the load in the external circuit. Cathode reaction, anode reaction, and overall reaction for a $\text{LiCoO}_2/\text{graphite}$ based LIB are as follows:²²



Cathode reaction is the deintercalation and intercalation of Li ions in the layered structure

of $\text{Li}_{1-x}\text{CoO}_2$. The x value in Equation (2) is usually controlled to vary from 0 to 0.5 during charge and discharge due to that excess deintercalation of Li ions can destabilize the lattice of $\text{Li}_{1-x}\text{CoO}_2$.²³ Graphite anode undergoes intercalation mechanism as well and the electrode reaction is shown in Equation (3). The overall reaction is shown in Equation (4). With x in the range of 0 to 0.5, a LiCoO_2 /graphite cell usually provides a voltage range of 3.0-4.2 V, and a major discharge plateau at around 3.7 V.

In a conventional LIB, electrode materials, both anode and cathode, are composed of an active material, a binder (*e.g.* polyvinylidene fluoride-PVDF, styrene butadiene rubber-SBR), and a conductive additive such as carbon black. They are first mixed together and form slurry prior being cast onto metal foils. Copper foils and aluminum foils are used as both substrates and current collectors for anodes and cathodes, respectively.²⁴ Selection of electrode materials and loading of active materials on current collectors vary, depending on the designated application of LIBs. The thickness of cast electrode material can be up to around 200 μm on a thin metal foil (10-20 μm) in a typical high energy density LIB. However, the thick electrode design may lead to challenges for Li ion diffusion and electron transport, which are vital for high power Li-ion cells. The balance of parameters (electrode composition, thickness, potential range, *etc.*) in battery design, the determining factors in battery performance, are largely selected according to the final application of LIBs.²⁵

2.2 Key Components in Li-ion Batteries

2.2.1 Anodes

Graphite is a type of carbon allotrope with a layered structure. On a single-layered plane

(also known as a graphene sheet), carbon atoms are located at the vertices of numerous honeycomb-like lattices. Graphene sheets are bonded to the neighboring sheets via weak van der Waals forces, as shown in **Figure 2.3**. Lithium ions intercalate into the interstitial spaces between graphene layers during lithiation process. As the most widely used anode material for LIBs, graphite has several advantages that explain its domination in the market of LIBs anodes. First, graphite is abundant in nature and cheap to obtain. Second, graphite shows good capability in storing Li by forming LiC_6 upon full Li intercalation (Theoretical capacity: 372 mAh g^{-1}). Third, graphite anodes can form a stable SEI, which will help graphite anodes maintain good stability over extended cycling. In addition, the low working potential (0-0.3 V vs. Li/Li^+) of graphite can help contribute to overall high energy density of a LIB. Despite the evolution of cathode materials from layered oxides, to spinel oxides, olivine oxides, and blend layered oxides *etc.*, for more than two decades after the wide commercialization of LIBs, carbon has always been a main source for LIB anode materials.

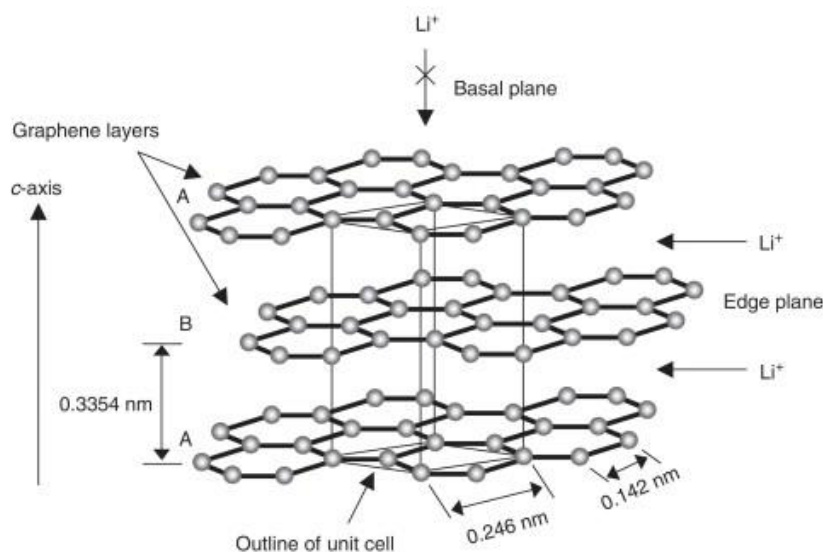


Figure 2.3 Crystal structure of hexagonal graphite showing the ABAB... stacking of graphene sheets and the unit cell.²⁶ Reprinted with permission from Elsevier.

However, the theoretical capacity of graphite is only 372 mAh g⁻¹, which cannot fulfill the increasing demand from lighter, but powerful electronic devices and electric vehicles, which require batteries with much higher energy density.²⁷

The use of Li metal in a rechargeable battery system can be dated back to one of the earliest Li-battery concepts in 1970s.²⁸ The research on Li metal for practical application is still of great interest due to its ultra-high theoretical capacity (3860 mAh g⁻¹) and lowest electrochemical potential (-3.05 V) versus standard hydrogen electrode (SHE), both of which can contribute to its extremely high energy density as a LIB anode.^{29, 30} However, Li metal has yet to be adopted as anode for commercial rechargeable Li batteries. There are several major challenges hindering the commercial application of Li metal in LIBs. First, continuous dendritic Li forms on the surface of the Li electrode poses a potential hazard, where the dendritic Li may pierce the separator and cause an internal short circuit and a subsequent thermal runaway. Second, the

volume change of the Li anode is significant since it is “hostless” during the plating/stripping process. Third, the continuous growth of unstable SEI on the surface of the Li metal electrode results in low Coulombic efficiency (CE), which is unfavorable for commercial applications. There have been emerging efforts trying to solve the problems associated with Li metal in recent years. For example, Yi Cui *et al.* reported a nanostructured carbon thin film placed between the Li electrode and electrolyte, and the thin layer avoids direct contact of liquid electrolyte and Li metal, which alleviates the phenomenon of uncontrolled dendrite formation and unstable SEI.³¹ In another report, Li metal is defect-induced plated into the porous graphene network, and the graphene network with caged Li metal prevents severe dendrite formation and facilitates long-term cycling of the Li metal-based electrode.³²

Alloying reaction can take place between Li and a wide spectrum of metallic and semi-metallic elements. Alloying materials have attracted much research interest due to their higher capacity and low electrochemical potential compared to other types of materials. Group IV elements such as Si and Ge are widely studied alloying anode materials.^{33, 34}

Apart from graphite, Li, and alloy anodes, many other anode materials have been examined over the development of Li batteries for the past half century. Most of them can be categorized as intercalation anodes, conversion anodes, and materials undergoing combined mechanisms. Intercalation is a reversible insertion and extraction process of guest ions or molecules in the host architecture. During an intercalation reaction, only small changes in structural properties of the host are observed. The host undergo a so-called topotactic transition, which is a thermally/chemically reversible process.³⁵ A typical intercalation anode material is graphite.

Other intercalation compounds include rutile and anatase TiO_2 , $\text{Li}_4\text{Ti}_5\text{O}_{12}$, *etc.*^{36, 37} Another type of candidate anode materials is the conversion reaction type anodes. Typically, a transitional metal compound (MX_y) is converted to metal M and the corresponding Li salt or oxide. Common conversion anode materials include Fe_2O_3 , Co_3O_4 , CuO , *etc.*³⁸⁻⁴⁰

There are also some materials that undergo combined mechanism when reacting with Li. For example, CoFe_2O_4 and SnO_2 exhibit both conversion and alloying behaviors in the electrochemical reactions with Li.^{41, 42} A brief list of different types of anode materials is displayed in Table 2.1.⁴³

Table 2.1 List of different anode materials for Li-ion batteries.⁴³ with permission from Springer.

	Anode material	Theoretical specific capacity (mAh g^{-1})	Potential, V vs Li/Li^+
Li	Li metal	3862	0
Carbon	Graphite	372	0.1
Alloy	Al (LiAl)	993	0.35
	$\text{Sn}(\text{Li}_{21}\text{Sn}_5)$	948	0.42-0.66
	Sb (Li_3Sb)	660	0.9
	$\text{Si}(\text{Li}_{4.4}\text{Si})$	4200	0.5
	Cu_6Sn_5 ($\text{Li}_{22}\text{Sn}_5 + 6\text{Cu}$)	605	0.1
Conversion	Co_3O_4	890	2.0
Spinel	$\text{Li}_4\text{Ti}_5\text{O}_{12}$ ($\text{Li}_7\text{Ti}_5\text{O}_{12}$)	175	1.56

2.2.2 Cathodes

Cathode materials have been playing very important roles in the development of LIBs since the introduction of early LIBs. They have evolved from dichalcogenides, trichalcogenides and related materials to the later layered oxides, olivine oxides and phosphates, which have

been widely adopted in commercial LIBs. LiCoO_2 , whose effectiveness as LIB cathode material was discovered by J. B. Goodenough group in 1980, was used in first commercialized LIBs.⁴⁴ Later on, cathode materials with advantages in different aspects have been developed and successfully adopted in commercial applications. LiMn_2O_4 and LiFePO_4 are two typical cathode materials, with spinel and olivine structures, respectively. They are made from more abundant and less expensive Mn and Fe metals.^{45, 46} Mixed metal oxides, reportedly offering higher electrochemical potentials or higher capacities, have also been developed and gained intensive popularity, including $\text{LiNi}_{1-y}\text{Co}_y\text{O}_2$, $\text{LiMn}_{1-y}\text{Co}_y\text{O}_2$, and $\text{LiNi}_{1-y-z}\text{Mn}_y\text{Co}_z\text{O}_2$.⁴⁷⁻⁴⁹ **Figure 2.4** outlines the formulae, crystal structures, discharge profiles versus Li reference electrode. **Table 2.2** summarizes the voltages, capacities, and some other important properties of several common cathode materials.

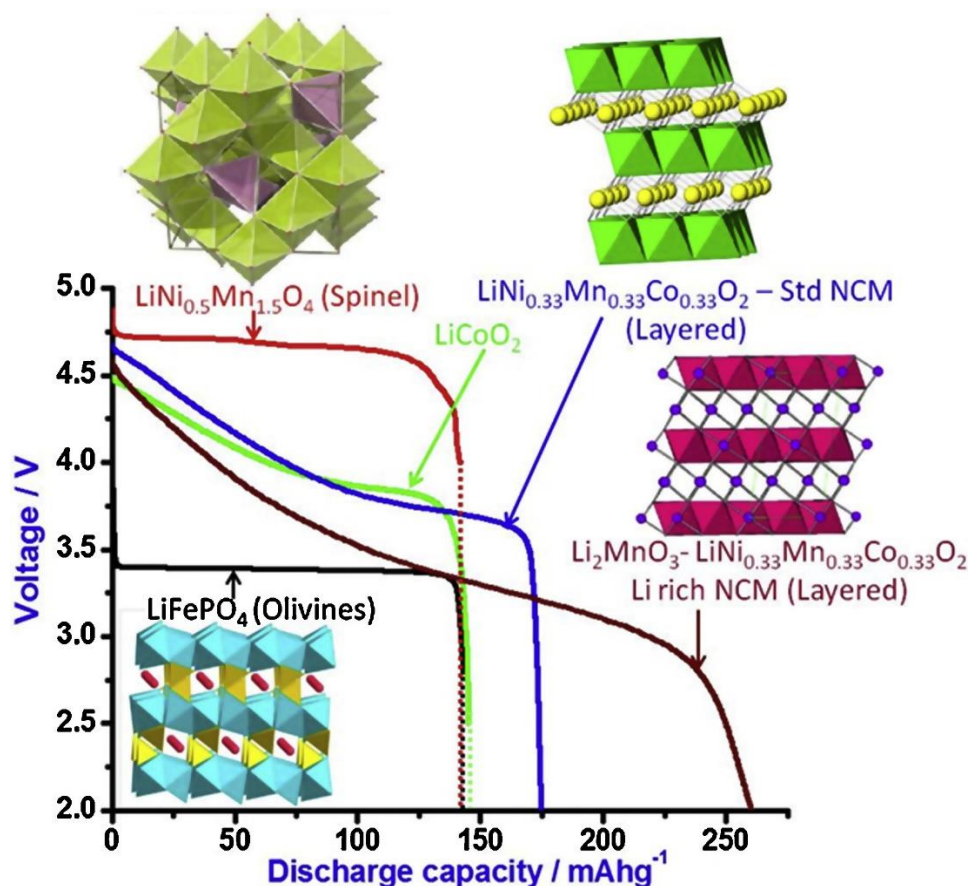


Figure 2.4 Important formulae, structures and voltage profiles during discharge of various Li-ion battery cathodes, with all potentials versus Li reference electrodes.⁵⁰ Reprinted with permission from Elsevier.

Table 2.2 Several popular commercial cathode materials with their properties, adapted from Li-ion batteries: Science and Technologies from Ref⁴³, with permission from Springer.

Material	Structure	Shape of the discharge curve	Average potential vs. Li ⁺ /Li (V)	Practical capacity (mAh g ⁻¹)	Safety	Cost
LiCoO ₂ (LCO)	Layered	Flat	3.9	160	Fair	High
LiNi _{0.8} Co _{0.15} Al _{0.05} O ₂ (NCA)	Layered	Sloping	3.8	200	Fair	Fair
LiNi _{1/3} Mn _{1/3} Co _{1/3} O ₂ (NMC)	Layered	Sloping	3.8	170	Good	Fair
LiMn ₂ O ₄ (LMO)	Spinel	Flat	4.1	110	Good	Low

LiFePO ₄ (LFP)	Olivine	Flat	3.45	160	Good	Low
---------------------------	---------	------	------	-----	------	-----

2.2.3 Electrolytes

During the operation of a rechargeable Li battery, electric current is conducted via electrons in the external circuit, while the charge carriers in the internal circuit are Li ions. Li ions migrate between cathode and anode during charge and discharge process. And the medium in which Li ions mass transfer is conducted is called electrolyte. There are several basic requirements for a LIB electrolyte. First, it must be able to retain the electrode/electrolyte interface during cycling. Second, an electrolyte should have adequate Li ion conductivity ($1 \times 10^{-4} \text{ S cm}^{-1}$) over the temperature range of battery operation. Third, the electric conductivity should be at extremely low level to avoid the battery from self-discharge and short circuit. In addition, an electrolyte must be chemically stable over the potential window of a battery. Other properties such as cost, environmental friendliness, and safety, are also in consideration in the quest of a suitable electrolyte.²⁴ Different electrolyte systems have been developed in order to fulfill various applications. A popular genre of electrolytes is organic liquid electrolytes composed of carbonate-based solvents and a Li salt, *e.g.* electrolytes of LiPF₆ in EC+DMC or in EC+DEC (diethyl carbonate). They are reported to be stable at potential range from 1-4.7 V, with good Li ion conductivity. In addition, they can help form SEI at the interface of electrolyte and electrode. EC is ubiquitously used in LIBs because it has high dielectric permittivity (89.78, 25 °C) that can facilitate the dissolution of LiPF₆. However, the melting point of EC is too high (36.4 °C) for it to be used as electrolyte solvent without the addition of other solvents. DMC is a commonly used co-solvent due to its low viscosity and good compatibility with EC. In

addition, the combination of EC and DMC results in a synergistic effect that was not fully expected by researchers beforehand. The mixture can endure wider electrochemical window, and have lower melting point than both of the solvents. In this sense, the merits of both EC and DMC, especially the good solvation power of LiPF_6 in EC, low viscosity of DMC that favors ion transport, can be fully exploited without sacrificing one another. Some other linear carbonates such as DEC, and EMC (ethyl methyl carbonate) are later discovered as suitable electrolyte solvents in addition to DMC. These solvents have similar electrochemical properties with DMC, while have lower melting points and higher boiling points.

It is undeniable that carbonate-based electrolytes are mostly sensitive to water, and highly flammable, which could be a potential safety hazard.⁵¹⁻⁵³ Other types of electrolytes have also been proposed with some specific properties, including room temperature ionic liquids,^{54, 55} inorganic liquid electrolytes, solid state electrolytes, hybrid electrolytes, *etc.*⁵⁶⁻⁵⁸

In the thesis work, commercial electrolytes with 1M LiPF_6 in EC/DMC or EC/DEC are used for non-Si electrodes. Fluoroethylene carbonate (FEC) is added to above commercial electrolytes to obtain electrolytes for Si electrodes. The presence of FEC additive in a Si-based LIB is reported to be beneficial for the stabilization of Si electrodes. In FEC-free electrolytes, the decomposition of EC and LiPF_6 and the formation of Li_2CO_3 and ROCO_2Li are primary contributors to the generation of SEI. While for the LiPF_6 /EC+DMC electrolyte with FEC additive, it is found that both EC and vinylene carbonate (VC) (resulting from FEC) contribute to the SEI formation. The surface films formed in this case contain both VC polymerization and EC reduction products. This helps provide better passivation layers with lower overvoltage

and impedance in the lithiation/delithiation process in contrast to those FEC-free electrolytes. It also explains the enhanced electrochemical performance of Si electrodes in FEC-containing solutions over FEC-free electrolytes.⁵⁹

Other electrolyte additives, including succinic anhydride,⁶⁰ Li bis(oxalate)borate (LiBOB),⁶¹ Li difluoro(oxalato)borate (LiDFOB),⁶² have also been reported to increase both cycle life and CE of Si electrodes.

2.2.4 Binders

A binder in an electrode acts like a glue that hold the electrode ingredients together and firmly attach them to the current collector. Although the mass ratio of binder material in an electrode is much lower than that of active material, it plays a key role in maintaining the structure integrity of electrode and good contact between electrode material and current collector.⁶³ Depending on the active materials used in an electrode, different binders are selected according to their properties. Carboxymethyl cellulose (CMC) was first reported to be the binder for graphite anodes.⁶⁴ Other binders like poly(acrylic acid) (PAA), have also been reported to be combined with graphite.⁶⁵ CMC binder was also found to be more effective than polyvinylidene fluoride (PVDF) in Si anodes by researchers, and it was proposed that CMC binder may act as a surface modifier for Si and help form a stable SEI on Si surface and improved cycling performance.⁶⁶ In addition, some researchers suggested that the full stretching of CMC in aqueous slurry facilitates the build-up of conductive network around Si and the chemical bonding between CMC and Si also contributes to the good performance.^{67, 68} Among the binders that have been reported to provide better performance in Si electrodes,

including CMC, styrene butadiene rubber (SBR), Nafion, PAA and carboxymethyl chitosan, they all have strong dipole or charge that has been found to interact with hydroxyl groups on the Si surface.⁶⁹⁻⁷¹ For most cathode materials, PVDF has been proved to be an excellent binder. Other binders including CMC and SBR have also been utilized to reduce the reliance on PVDF, which is an organic-solvent based binder.⁷²

2.3 Background and Literature Review on Si-based Anodes

2.3.1 *Reaction Mechanisms, Challenges, and Prospects of Si-based Anodes*

A series of Si-Li phases exists in the process of thermal alloying of Si and Li, including crystalline phases of LiSi, Li₁₂Si₇, Li₁₃Si₄, and Li₂₂Si₅. These crystalline phases tend to be more kinetically stable than the corresponding amorphous phases due to their lower formation energy. However, these crystalline phases are not always favorably formed during the actual electrochemical lithiation of Si. One atomic model of crystalline Si lithiation reported by Liu et al. vividly revealed ledge peeling process the Si (111) atomic facet by Li ions.⁷³ Through the lattice-scale in situ TEM imaging, layer-by-layer formation of Li_xSi alloy at the reaction interfaces was captured. A Si nanowire (Si NW) with a diameter of 130 nm, and a <111> growth direction is used for lithiation (**Figure 2.5a**). Upon lithiation, an amorphous Li_xSi shell is first developed on the surface of the nanowire. Progressive migration of the sharp amorphous/crystalline interface during solid-state amorphization the Si NW is displayed in Figure 2.5b. The amorphous/crystalline interface has only ~1 nm thickness with a unique contrast between the amorphous and crystalline phases. After the full lithiation of the Si NW,

the volume of the wire increases by $\sim 280\%$.

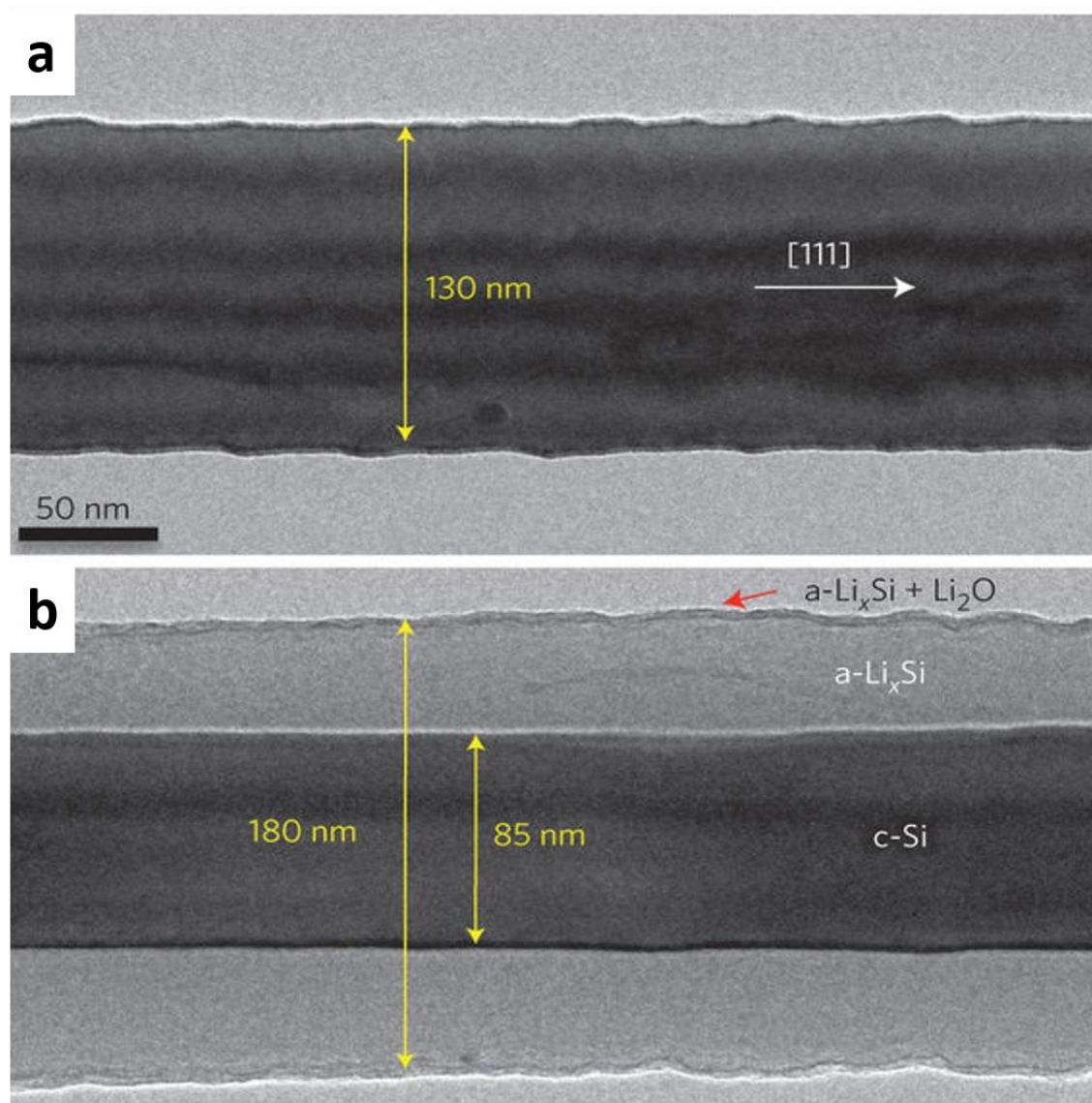


Figure 2.5 a) Pristine Si nanowire with rough sidewalls due to faceting, b) Partially lithiated Si nanowire with an a-Li_xSi layer surrounding the c-Si core.⁷³ Reprinted with permission from Nature Publishing Group.

It should be noted that with the assistance of many in situ characterization techniques, such as in situ NMR,⁷⁴ in situ AFM,⁷⁴ and in situ SEM,⁷⁵ the understanding of reaction mechanisms of Si in LIBs is becoming more approachable.

One inevitable challenge with Si anodes, as well as other alloy-type anode materials, is their poor cycling stability due to the large volume change and the resulted effects during charge and discharge. Upon full lithiation, the volume of Si can expand to about three times of its original value. The significant volume change poses a serious challenge for Si electrodes to retain their morphology and electrode structure over cycling.

In order to engineer against these problems, one must first investigate and understand the underlying natural phenomenon that is occurring. As such, a lot of previous work has been allotted to uncover the exact failure modes of Si anodes. The large volume change of Si during lithiation/delithiation causes electrode failure mainly through the following three mechanisms.

- 1) Large volume changes in the bulky films and particles lead to high internal stress on Si, causing pulverization of Si morphology. This phenomenon is common with several other alloy-type anode materials.

- 2) Upon constant volume change and pulverization, much of the active material loses electrical contact with its neighboring unit, conductive network, and current collector, and causes self-isolation of the active material and loss of electrical conductivity.

- 3) Large volume changes and pulverization of Si inevitably cause the repetitive growth and formation of an unstable SEI layer. During the first lithiation step, electrolyte decomposes on the surface of Si anode and forms a self-passivating SEI layer. This SEI layer is majorly composed of polycarbonates, Li-based salts and oxides. It causes minimal Li-ion conduction resistance, but significantly limits electron flow. A thin passivating SEI layer can protect electrolyte from direct contact with Si and avoid further decomposition.⁹ With the fracture of

Si, fresh SEI continuously forms on the newly exposed Si surfaces. The formation of a stable SEI has been reported to be crucial for the long cycling of Si electrodes, however, excess continuous growth of SEI consumes significant amount of Li ions in electrolyte and further blocks electron conduction pathways, which finally deactivates Si from further reversible electrochemical reactions.⁷⁶ Apart from the electrode degeneration issues of Si, the huge volume change poses severe challenges for the design and fabrication of multi-stack LIBs with Si anodes, as the significant volume change of Si anodes may lead to the deformation of a full cell battery.⁷⁷

2.3.2 Development of Si Morphologies

Nanostructured or nanoscale Si materials have better capability in accommodating the volume change of Si due to their larger specific surface area and higher average binding energy per atom at the surface.⁷⁸ These materials can thus minimize the stress from volume change on them and avoid cracking or pulverization of their structures, and reduce irreversible capacity and enhance cycling stability.⁷⁹ The order of stress experienced by Si materials is also dependent on the morphology and crystallinity. On the one hand, according to the isoperimetric inequality of geometry, spheres have the least surface area compared to those in more complex shapes with the same volume. Stress on spheres are usually isotropic, while materials with higher dimensions such as Si nano thin films and NWs, have been reported to experience anisotropic volume changes due to both morphological properties and stress induced by adhesion to current collector.^{80, 81} In addition to changes in morphology, there have also been reports about the crystallinity and size effects of Si on the structural stability during volumetric changes. Crystalline Si transforms to amorphous Si alloy during the first lithiation process.⁸²

Formation of amorphous Li/Si alloy is beneficial for its mechanical stability due to the experienced isotropic mechanical stress rather than anisotropic upon volume changes.

Compared to the solid particles of Si, 0 dimensional hollow Si spheres and porous Si particles can provide better accommodation for volume change due to larger specific surface area and greater tolerance for tensile stress^{83, 84, 85}

The small diameter of 1-D Si nanostructures largely avoids the initiation of fracture that can occur in bulk or micron-sized materials, and helps demonstrate good accommodation for stress and volume changes. In addition, 1-D Si nanostructures possess good conductivity with more continuous conductive paths, and better electrical contact between active material and conductive network or substrate. Widely studied 1-D Si materials include Si nanowires (NWs),⁸⁶ Si nanofibers,⁸⁷ Si nanotubes.⁸⁸ Unlike particulate Si, which can be prepared via mechanical milling, synthesis of 1-D Si structures usually requires more complex chemical processes.

Si thin films have received much attention in the application of LIB anodes due to the much-improved electrochemical performance, as well as their simple electrode configuration.⁴ One should note that while literature demonstrated a promising example of Si thin film for LIB anodes, the commercial LIB electrodes usually bore an areal capacity of 1.5-2 mAh cm⁻², which required the thickness of Si thin films to be a few micrometers.⁸⁹ The problem of Si areal mass loading had as expected, posed a notable challenge for the practical application of Si thin films in commercial LIBs.

3-D Si-based anode materials are of great interest as they can absorb the advantages of

nanostructures from 0-D to 2-D, while extend these merits to a 3-D scale. The inherent features of nanostructures such as nano-sized Si, nano pores on both Si structures and Si composites, can help avoid Si pulverization. In addition, these features can also provide necessary space for volume change to maintain the electrode integrity, and facilitate electrolyte diffusion inside the 3-D structures.

Integrating nano-sized Si with micron-sized host/frameworks is another plausible approach because Si can be well distributed in the secondary structure, and the embedding of Si is usually accomplished simultaneously with the formation of micron-sized Si composite. The accessory materials and the reaction conditions can be easily controlled to tune the morphology of secondary particles. Compared to pure Si nano structures, micron-sized secondary Si structures usually present a higher tap density, which is a crucial factor in the design of practical LIBs. Methods for the fabrication of micron-sized Si structures include spray-dry,⁹⁰ nebulized-spray-pyrolysis,⁹¹ CVD,⁹² etc, and the raw material selection for the formation of secondary structure can be broad.

2.3.3 Development of Si-based Composites

Apart from the quests for different morphologies of Si, Si-based composites are another focus for the development of high-performance Si anodes. Si-based composites have been widely studied to overcome the difficulties of Si anodes resulting from the intrinsic properties of Si. As previously discussed, notorious issues with Si anodes arise from the significant volume changes, including electrode structure degradation, loss of contact points between active material and conductive network, and unstable SEI formation. It is impossible to tackle

all these issues by solely engineering Si morphologies. Different carbon-based conductive additives have been proven to be essential for the electrode conductivity improvements in LIB electrodes and as a result, the electrochemical performance of electrode. These conductive materials have also been found to be vital for the improvement of Si electrodes, not only by the enhancement of the electrical conductivity of Si electrodes, but also in some cases, buffering the volume change of Si during lithiation process, and stabilizing the SEI. With the presence of conductive additives in the slurry composition, nano-sized Si achieved further performance improvements, benefiting from better electrical conductivity and accommodation for volume change.^{93, 94} However, simple addition of conductive agents cannot provide an intact and robust matrix protecting Si and stabilizing SEI, and thus the performance improvement is limited. Tremendous efforts have been made to create more efficient conductive and protective networks.

Before the thriving of research on various Si morphologies, the combinations of Si particles with carbonaceous materials were found to be an effective approach to improve Si anodes. A carbon-based matrix support cannot only provide a conductive network for the Si active material, but also accommodate the mechanical stress of the active phase over the up-take and release of Li in Si. One widely-used method for the mixing of Si and carbon materials is high-energy ball milling, in which Si and carbon precursors are milled in a jar filled with inert gas. Solution-based mixing is another commonly used method for the construction of Si/C composites. A pyrolysis step is usually followed to carbonize the carbon-containing micro molecules or polymers.⁹⁵

Beyond the improvement of Si anodes by addition of carbon via simple mixing or pyrolysis of carbon precursors, Si/carbon composites have been advanced with more delicate core-shell design, and the introduction of void space in between Si and carbon. The Si/C core-shell design was first proposed and realized in order to solve the electrical conductivity issue, and the repetitive SEI growth on the surface of Si. Various Si morphologies have been adopted in the design of core-shell/yolk-shell Si/C composites, combining the advantage of both versatile Si morphologies and structures.⁹⁶⁻⁹⁸

Fundamentally speaking, graphene is a monolayer carbon allotrope with 2-D morphology. Carbon atoms are chemically bonded in a hexagonal pattern similar to that of a planar honeycomb. Although the existence of 2-D monolayer graphene crystal was widely accepted by scientists, it was not until 2004 that the miraculous superstar material made its inception.⁹⁹ In just over a decade, graphene has attracted tremendous attention and research interests from a wide spectrum of areas owing to its spectacular electronic, mechanical, and surface properties.¹⁰⁰⁻¹⁰² By applying different synthetic routes, graphene with different characteristics and properties can be prepared for various applications. In the case of LIBs, graphene has demonstrated good capability in reversibly storing Li,^{103, 104} as well as improving the performance of both cathode and anode materials.^{105, 106} With an excellent electrical conductivity and superb mechanical properties, graphene has also been able to greatly relieve the symptoms with Si anodes.

CNT is another emerging star in a wide spectrum of applications, including drug delivery,^{107, 108} energy conversion and storage,¹⁰⁹⁻¹¹¹ environmental applications,^{112, 113} etc. Like graphene,

CNTs have also attracted intensive research interest in the combination with Si. CNTs can not only provide very good conductivity to LIB electrodes as a conductive agent, but also provide effective conductive network for Si when integrated with Si as Si/CNT composite.

In addition to the exhaustive survey on Si/C composites, researchers have also explored merits of Si/metal alloys and Si/metal oxide composites as LIB anodes. Alloy metals can play unique roles in Si alloy anodes, along with their ability to reversibly store Li.¹¹⁴ Li inactive metals have also been reported by researchers and attempted in commercial LIBs.^{115, 116} Unlike alloys, Si/metal oxide composites usually render a core-shell structure. Similar to the previous concept with Si/C core-shell composites, a layer of coating layer on Si can serve to prevent direct physical contact of Si with the electrolyte.

Table 2.3 outlines various Si morphologies, structures, and composites as LIB anodes. Synthesis methods of different types of Si anodes are provided along with their capacity and cycling information. To fairly judge the promise of a material, many more factors should be taken into consideration. Therefore, it is desirable that researchers in this field put more emphasis on the practical aspects of new materials developed. These aspects may include cost, electrode and fabrication details, full-cell LIB data, etc.

Table 2.3 Electrochemical performances and characteristics of some representative Si anode materials.

Categories of Si		Synthesis method	Cycling stability			
			Specific capacity (mAh g ⁻¹)	Cycle number	Current/rate	Ref.
Nano-sized Si	Hollow Si	CVD and HF etching of template	1420	700	C/2	85
	Porous Si	Mg reduction of silica and acid treatment	1200	600	C/2	83
	Si nanowire	CVD on substrate	3500	20	C/5	86
	Si nanofiber	Electrospinning and magnetron sputtering	1821	1000	C/5	87
	Si nanotube	CVD of Si and template removal	2000	50	C/5	88
	Si nano film	Vacuum evaporation and deposition	3000	1000	12 C	89
Micron-sized Si	3-D porous Si	Thermal annealing and etching of butyl-capped Si gels and SiO ₂	2800	100	1 C	117
	Pomegranate-like secondary Si	Si@SiO ₂ cluster formation and etching	1160	1000	C/2	118
Si/C composites	Simple Si/C composite	Pyrolysis of polymers with Si	1200	30	C/10	119
	Yolk-shell Si/C	SiO ₂ and carbon coating, before removal of SiO ₂	1500	1000	1 C	120
	Si/graphene	Freeze-drying	840	300	1.4 A g ⁻¹	121
	Si/CNT	Growth of CNT on substrate and sputtering of Si	2502	100	C/5	122
Other Si composites	Si/conductive polymer	In situ polymerization on Si	550	5000	6 A g ⁻¹	123
	Si/metal alloy	Evaporation and deposition of Si and Ge	1600	50	Up to 2 C	114
	Si/metal oxides	Solution formation of Li ₄ Ti ₅ O ₁₂ on Si	1000	1000	1 C	124

3. Characterization Techniques

3.1 Physical Characterization Techniques

3.1.1 Scanning Electron Microscopy (SEM)

Scanning electron microscopy (SEM) is a powerful imaging tool used to investigate morphology and topological features of micro- and nano-structured materials. It involves illuminating samples with a powerful beam of electrons, and projecting images based on the collected secondary or backscattered electrons.¹²⁵ The image resolution is similar to the size of the utilized electron beam and can reach nanometer scale. In the proposed project, SEM will be utilized to investigate the distinct nanostructures of the fabricated electrode materials. Preparation of samples for SEM imaging involves spreading the powder sample onto carbon tape that is attached to a aluminum sample holder stub. This stub can then be placed into the SEM machine, followed by evacuation of the sample chamber and subsequent imaging.

3.1.2 Transmission Electron Microscopy (TEM)

Transition electron microscopy (TEM) allows in-depth imaging of samples at nanometer scale, whereby high-resolution TEM imaging can approach sub-nano resolution. Samples are illuminated by a high-energy electron beam with constant current density, which is generally produced by field emission techniques and passed through several condensers to focus it upon a very small site of interest. When the electrons encounter the sample, they will be scattered either elastically or inelastically and collected. Based on electron diffraction theory, the signals from the collected diffracted electrons can be processed to produce an image. With such high resolution, TEM is effective in determining nanostructures, atomic arrangements, exposed

crystal facets and defects within the structure.

3.1.3 Energy Dispersive X-ray Spectroscopy (EDX)

Energy dispersive x-ray spectroscopy (EDX) capabilities are commonly incorporated into SEM and TEM devices, and can be carried out concurrently with common imaging techniques. EDX involves bombardment of electrons onto a material's surface which results in the emission of X-rays collected by a detector. The energy of the emitted x-rays and their corresponding intensity are characteristic of certain elements, allowing their appropriate identification and quantification in the sample being investigated. Elemental mapping is also an interesting technique that can be utilized; it involves analyzing the X-rays emitted from localized positions on the sample. Variations in the emitted X-ray intensities will indicate variations in the specific atomic contents at those locations and can be used to map the concentrations of different elements over the entirety of the sample being investigated.

3.1.4 X-ray Diffraction (XRD)

X-ray diffraction (XRD) is a versatile characterization technique, which allows the determination of crystal structure. The X-rays from the source interact with the sample to produce diffraction patterns at the angles corresponding to specific crystal planes. The X-ray source is swept over a range of angles and the diffracted X-rays at specific angles are collected and processed by the detector. The angle of diffraction is related to the specific crystal orientation of the sample by Bragg's law as shown by Equation (5) below,

$$2d \cdot \sin\theta = n\lambda \quad (5)$$

where n , λ , d , and θ represent the order of the spectrum (any integer), the wavelength of the X-rays, the spacing between diffracting planes, and the incident angle, respectively. The diffraction pattern at specific angles obtained by XRD can be compared to the theoretical diffraction pattern calculated by the crystal planes to help identify the material. Having said this, sharp XRD patterns cannot be produced with amorphous materials as they do not have ordered crystal planes that interact with X-rays to produce diffracted patterns. In this research, XRD is used to identify materials and confirm their crystal structures and changes, which can guide the analysis of electrochemical performance as well as the improvement in experimental procedures.

3.1.5 X-ray Photoelectron Spectroscopy (XPS)

X-ray photoelectron spectroscopy (XPS), also known as electron spectroscopy for chemical analysis (ESCA), is an elemental characterization technique allowing investigation of elemental composition, empirical formula, chemical state, and electronic states of a material. This technique works by irradiating X-ray on the sample to induce emission of electrons by the photoelectric effect. The detected kinetic energy and the number of electrons from the samples surface are analyzed to produce a pattern with intensity versus binding energy. The specific binding energy of the electron acts as the fingerprint for identifying the composition of the sample with the intensity corresponding to the quantity of elements. In this research, XPS is used to identify composition and chemical state of sample surfaces. Carbon 1s peak is used to calibrate the XPS results before the analysis of other elements.

3.1.6 Raman Spectroscopy

Raman spectroscopy is a spectroscopic technique used to detect a sample's vibrational, rotational and other low-frequency modes. When a sample is radiated by a monochromatic laser beam, both elastic scattering (Rayleigh scattering) and inelastic scattering (Stokes and Anti-stokes) are generated, while only the inelastic scattering is used in Raman spectroscopy to give Raman signals. Samples for Raman spectroscopy may exist in solid, liquid and gaseous phases. A Raman set-up typically consists of several key components including a radiation source (usually a laser generator), a sample illumination system and light collection optics, a wavelength selector (filter or spectrophotometer) and a detector, frequently functioned by a charge coupled device, photo multiplier tube or photo diode array.

In a Raman spectroscope, illumination laser can be in ultra-violet, visible, and near-infrared region according to the specific requirement of different samples. Scattered light is condensed by a lens and then sent through an interference filter or spectrophotometer to obtain the Raman spectrum of a sample. Around 99.999% of the scattering in a normal Raman spectroscope is Raman-inactive Rayleigh scattering, and only the rest 0.001% is inelastic Raman scattering, which makes it very difficult for a detector to filter the useful signal from all the scattering radiation. This requires special treatment on the signals to distinguish the target Raman signal from other useless signals. Several categories of instruments including laser stop apertures, tunable filters, notch filters, spectrometric systems, double and triple are used to separate high-quality Raman spectra from strong Rayleigh scattering. In the presented thesis, many materials are carbon-based composites, which can be well characterized with Raman spectroscopy.

3.1.7 Thermogravimetric Analysis (TGA)

Thermogravimetric analysis (TGA) is used to measure thermal properties of a sample by increasing the sample's temperature at a set rate in a specific atmosphere. A typical TGA apparatus contains a precise balance, a thermo-tolerant sample pan, and a programmable furnace. It can provide information of a sample such as its melting point, boiling point, dehydration temperature, combustion temperature, and composition of a sample with several components. For example, in this thesis, the mass ratio of Si in Si-rGO composites can be obtained by a TGA test. The sample is put into a TGA burning chamber in atmosphere, and the final temperature is set to be 900 °C. The ramp rate is set to be 10 °C per min. As the temperature increases, rGO is first burned away, since it has a lower burning temperature than Si. There is a steep drop on the mass-temperature curve, and from the minimum of the curve the mass ratio of Si in the whole composite can be determined. Since the sample only contains two ingredients, the mass ratio of rGO can also be obtained by deducting the mass ratio of Si from 100%.

3.1.8 Surface Area and Pore Analysis

In this thesis, surface and pore analyses of electrode materials are of vital importance. Named after Stephen Brunauer, Paul Hugh Emmett, and Edward Teller, BET theory was developed to explain the sorption of gas molecules on solid surfaces. Typically, specific surface area of a solid material can be obtained via BET analysis of isotherm data from the nitrogen adsorption/desorption conducted at 77K, the boiling point of N₂ gaseous adsorbate. Volume change of Si during charge discharge poses unique challenges to the development of stable Si

anodes. Dedicate control of surface area and engineering of pores can be effective in countering the side effects of the inevitable volume change. Pore volume and pore size distribution can be obtained from the adsorption/desorption isotherms using different methods, such as Barrett-Joyner-Halenda (BJH) method.

3.2 Electrochemical Evaluations

To evaluate the electrochemical properties of the synthesized material, Li-ion coin cells (CR2032) are fabricated. Breakdown of a coin cell is shown in **Figure 3.1**. Electrode fabrication methods and electrode compositions in this thesis may vary based on materials and the actual requirements. Typically, all ingredients are mixed together with a solvent, forming a homogeneous slurry. The slurry is cast onto a copper foil current collector for anode, and aluminum foil for cathode. The copper foil or aluminum foil with electrode material is subsequently dried in a vacuum oven, cut into the desired electrode shape, and transferred into an argon-filled glovebox, in which coin cells are fabricated.

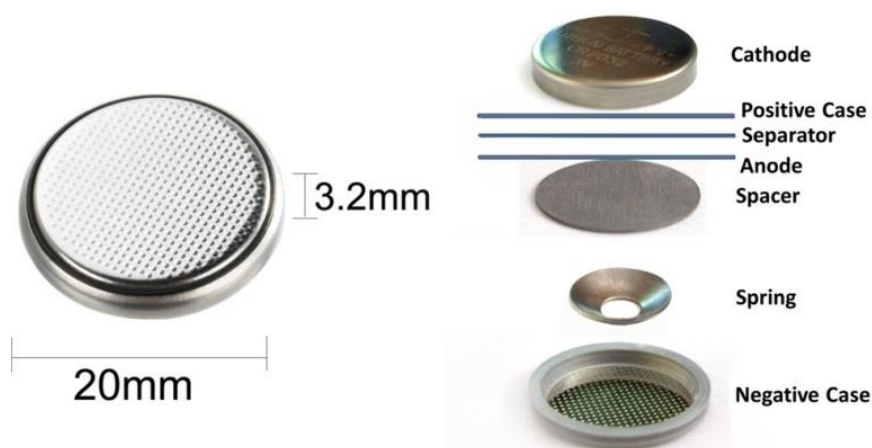


Figure 3.1 Breakdown of a coin-type 2032 LIB cell.

Electrochemical tests including galvanostatic charge and discharge, which can obtain the

profile data of charge and discharge process and cycling performance. Rate capability data of an electrode can be obtained when different currents are applied in the charge and discharge tests. Fresh-made coin cells are often started with a low current, e.g. 0.1 A/g on a battery tester to obtain the approximate capacity of the cells. Charge and discharge profiles can provide capacity, plateau information and voltage window of a cell. High currents of up to several amps per gram can be applied depending on the quality and requirement of an electrode material. Cyclic voltammetry (CV) is a potentiodynamic electrochemical measurement technique used to analyze the redox properties of the sample. CV measurements are done by sweeping the potential of the working electrode linearly at a certain scan rate within a desired potential window. For Si anodes, voltage window is usually set to be ~0.01-1.5 V, and the scanning rate is usually below 0.5 mV s⁻¹. The measured current over a potential window is the characteristic of the material's redox property (Li insertion and extraction in this case), which can be compared to the theoretical values. This enables identification of redox reactions in an electrode and degree of reversibility. In this research, CV is used to confirm the potentials at which Li insertion and extraction take place. The position and intensity of peaks and peak shifts over cycling can reflect the composition and change in electrode materials. Electrochemical impedance spectroscopy (EIS) is used to study the internal resistance of batteries to evaluate the property of electrode materials, SEI layer, and electrolytes by applying the corresponding Nyquist model and evaluating various parameters. Electrochemical workstation from Princeton Applied Research are utilized to perform EIS tests. Coin cells from a same project are clamped with same cell fixture. In a typical EIS test, amplitude of the perturbation voltage is set to be 10 mV, and the frequency range is 1 M Hz-0.1 Hz. All EIS measurements are done at open

circuit after the discharge to the lower cut-off voltage. For each coin cell, repeated tests are carried out to eliminate errors (overlapping impedance spectra from the same sample).

3.3 Full Cell Electrochemical Analyses

A half-cell rechargeable Li battery usually consists of a working electrode and a piece of Li chip as its counter and reference electrode. For the evaluation of both cathode and anode, Li is an ideal reference for its good reliability and consistency. And it is of great convenience for researchers working on different materials to compare their performance using the universal reference. The configuration of a full-cell Li battery resembles that of a half cell in terms of battery components. The main difference is that the Li reference is replaced with an actual anode or cathode. In this thesis, Si-based anode materials were first evaluated in half cells coupled with Li. With the mature development of Si anodes, commercial cathode materials such as $\text{LiNi}_{1/3}\text{Mn}_{1/3}\text{Co}_{1/3}\text{O}_2$ (NMC) could be adopted to assemble full cells with Si, and deliver the data of energy density that might be comparable to commercial products.

4. Construction of Graphene-based Carbon Network Containing Si NPs

4.1 Introduction

This chapter is reprinted in adapted form from the article below,¹²⁶ with permission from Elsevier.

Kun Feng, Wook Ahn, Gregory Lui, Hey Woong Park, Ali Ghorbani Kashkooli, Gaopeng Jiang, Xiaolei Wang, Xingcheng Xiao, Zhongwei Chen. Implementing an in-situ carbon network in Si/reduced graphene oxide for high performance Li-ion battery anodes. *Nano Energy* **19**, 187-197, (2016).

To tackle the notorious volume change and other associated issues with Si electrodes as introduced in Chapter 2, several strategies have been proposed by researchers. One of the potential solutions is to design various nano-structured Si electrodes. Nano-sized Si can better accommodate mechanical strain during lithiation/delithiation process, and avoid cracking and fragmentation. Improved cycling stability has been demonstrated with mechanically-milled nanostructured particles, and chemically synthesized nanostructures including nanowires, nanotubes, nanoporous structures, and core-shell nanostructures. Another effective strategy to improve Si's performance in batteries is to build an efficient conductive network for Si. Si/C, Si/Graphene, Si/CNT and Si/conductive polymers have been reported to exhibit enhanced performance compared to bare Si. Although these results have shown some promise, there are some significant issues regarding their synthesis. Many of these procedures are highly complex and expensive. For example, the synthesis of Si nanowires (Si NWs) usually requires complex

procedures and dangerous precursors such as silane gas. Template growth of Si usually involves multi-step template synthesis and removal steps, adding to the cost of the final Si product. All these factors make it hardly possible for these materials to be widely commercialized.

RGO has been intensively studied in the electrochemical field because of its unique structure and superior physical properties including conductivity, mechanical strength and flexibility. It has recently been combined with Si to form composite anode materials in LIBs.¹²⁷ Wrapping rGO around Si NPs significantly improves the electrochemical performance of Si NPs in terms of both cycle and rate performance. However, despite the good contact between rGO and Si, the composite still fails to maintain long-term stability. Reported Si-rGO composites generally suffered considerable degradation after certain cycles.¹²⁸ The degradation of the above Si-rGO anode can be explained by the fact that many of these composites are synthesized using physical mixing, which does not lead to strong chemical bonding between Si and rGO. In addition, the size of rGO sheets is usually much larger than that of Si NPs. These make it difficult to homogeneously wrap Si NPs with rGO. Poor wrapping of Si with rGO and migration of Si NPs from rGO during cycling result in most of the reported unsatisfactory performances.

In this project, we present a highly efficient Si reduced graphene oxide carbon (Si-rGO-C) composite with good Si wrapping and thus improved electrochemical performance compared to commercial Si NPs and regular Si-rGO composite. In order to take advantage of both carbon coating and rGO wrapping, a facile freeze-drying method and a subsequent chemical vapor deposition (CVD) process were conducted using commercially available Si NPs. Si NPs were

well embedded onto the GO layers, and the sponge-like composite served as the precursor of the next step carbon incorporation. The following advantages of the obtained Si-rGO-C composite were first proposed and proved based on the electrochemical performances presented in the context. First, a layer of carbon on exposed Si NPs provides enhanced electron conductivity between particles and other rGO flakes with wrapped Si NPs. Second, the carbon rods between the rGO flakes create an effective conductive network in the whole electrode, helping electrons transfer from one rGO sheet to another and eventually to the current collector. Moreover, the flexibility of rGO and the carbon network can also help restrain the electrode morphology change during cycling, avoiding significant detachment of the active material from the conductive network and helping to maintain contact between the electrode material and the current collector. Various physical and electrochemical measurement techniques were adopted to characterize the samples.

4.2 Experimental Methods

4.2.1 Material Synthesis

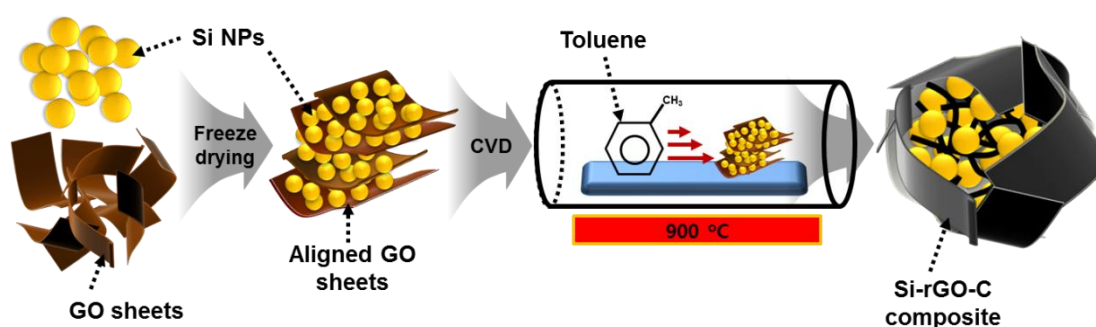


Figure 4.1 Schematic illustration of the synthesis procedure of Si-rGO-C composite.

Experimental procedures constructing the Si-rGO composite resemble our previous

work.¹²⁹ The schematic illustration of the synthesis procedure of Si-rGO-C composite is shown in **Figure 4.1**. Si NPs (Nanostructured & Amorphous Materials Inc, USA. Average diameter 70 nm) and GO (Prepared using a modified Hummer's Method) were separately dispersed in distilled de-ionized water (DDI 18 M MΩ·cm) in a sonicator bath (Fisher Scientific FS220, USA) for 5 hours. The mass ratio of Si NPs to GO was 2:1. Two dispersions were subsequently mixed together and sonicated for another 5 hours to achieve a homogeneous solution. The final mixture was rapidly frozen with liquid nitrogen and placed in a freeze-dryer (Labconco Freezone 1, USA). The sponge-like Si-GO composite was then transferred into a quartz tube in a CVD system (Thermal Product Solutions, Lindberg Blue M 1200°C Small Tube Furnace, USA). 10% hydrogen (H₂) in argon (Ar) gas was used to purge the system at a rate of 140 cm³ min⁻¹ for 20 minutes. The rate of the gas was subsequently adjusted to 70 cm³ min⁻¹ for the reaction until the furnace cooled down to room temperature. The furnace was set to ramp from room temperature to 900 °C in 15 h and held at this temperature for 3 h. Toluene was used as the carbon source in the CVD reaction. After 2.5 h at 900 °C, toluene was injected with a syringe pump at a rate of 0.05 mL min⁻¹ for 10 minutes for the carbon growth. The furnace was shut down immediately and cooled down naturally to room temperature. Si-rGO composite without carbon coating was synthesized using the same method but without the CVD step.

4.2.2 *Physical Characterizations*

The weight ratio of total carbon content was examined by thermal gravimetric analysis (TGA) (TA Instrument Q500, USA). A 5-mg sample was used in the analysis. The sample was heated up to 850 °C at a ramping rate of 10 °C min⁻¹, and the test was conducted in air

atmosphere. X-ray diffraction (XRD) (monochromatic Cu K- α X-rays, 0.154 nm wavelength, Inel XRG 3000 Diffractometer, France) was used to examine the crystallinity of Si after the high-temperature reduction of rGO and the CVD carbon coating process. X-ray photoelectron spectroscopy (XPS) (Thermo Scientific K-Alpha, USA) was conducted with Si-GO, Si-rGO, and Si-rGO-C samples to study the change of GO and the growth of carbon. The morphology of the composite was studied by field emission scanning electron microscopy (FESEM) (Zeiss Ultra Plus, UK) and transmission electron microscopy (TEM) (FEI Philips CM300, USA).

4.2.3 Electrochemical Measurements

A slurry for the electrode was prepared with 80 wt% as-synthesized active material and 20 wt% sodium carboxymethyl cellulose (NaCMC) binder. Traditional conductive additives such as super-P were eliminated to increase the ratio of active material in electrodes. NaCMC was first dissolved in water to form a 2 wt% solution. The slurry was cast onto a thin and flat copper foil with a doctor blade. The foil was subsequently placed in a regular oven at 80 °C for 2 hours and then transferred to a vacuum oven overnight to evaporate the solvent from the slurry and foil. Electrodes were punched from the foil and pressed. The average loading of the Si-rGO-C composite on copper foil was 1.1 mg cm⁻². CR 2032 coin cells were fabricated inside an argon-filled dry glovebox (Labstar 10, Mbraun, USA) where both oxygen and water content were maintained below 0.5 ppm. The electrolyte consisted of Li hexafluorophosphate (LiPF₆) dissolved in a solvent containing 45% dimethyl carbonate (DMC), 45% ethylene carbonate (EC), and 10% fluorinated ethylene carbonate (FEC). Li metal was used as both a counter electrode and a reference electrode. A polypropylene membrane (PP2075, high porosity, 20 μ m

micro porous, Celgard, USA) was used as the separator. Cycling tests and rate capability tests were conducted using a battery testing system (BTS 3000, Neware, China). Cyclic voltammetry (CV) was performed using an electrochemical work station (Versa Stat MC, Princeton Applied Research, USA). The battery was scanned between 0.05 V to 1.5 V using a scan rate of 0.1 mV s⁻¹. Batteries of the control group (Si-rGO) were also fabricated and tested using same testing procedures. All electrochemical tests were conducted at room temperature. All measurements were based on the gravimetric mass of entire composite (Si-rGO, Si-rGO-C). A five-cycle activation/aging process at 100 mA g⁻¹ was applied to all cells except for cells fabricated for CV tests.

4.3 Results and Discussions

A versatile freeze-drying method was used to obtain a well-aligned structure of GO with Si NPs. Ice as a template not only forms in-situ inside the composite, but also fills the microchannels and helps keep aligned/ordered porous structures. In addition, ice can be easily removed by a low temperature sublimation process. Its low cost and environmental friendliness make it a suitable template reagent for large scale production of the Si-GO composite.¹³⁰ **Figure 4.2a** shows that the dried Si-GO composite is a low-density sponge-like material with a well-maintained size and shape. The sponge-like structure is also well maintained after the carbon coating process, while the color of the composite turns to black after the reduction of GO to rGO and the growth of additional carbon.

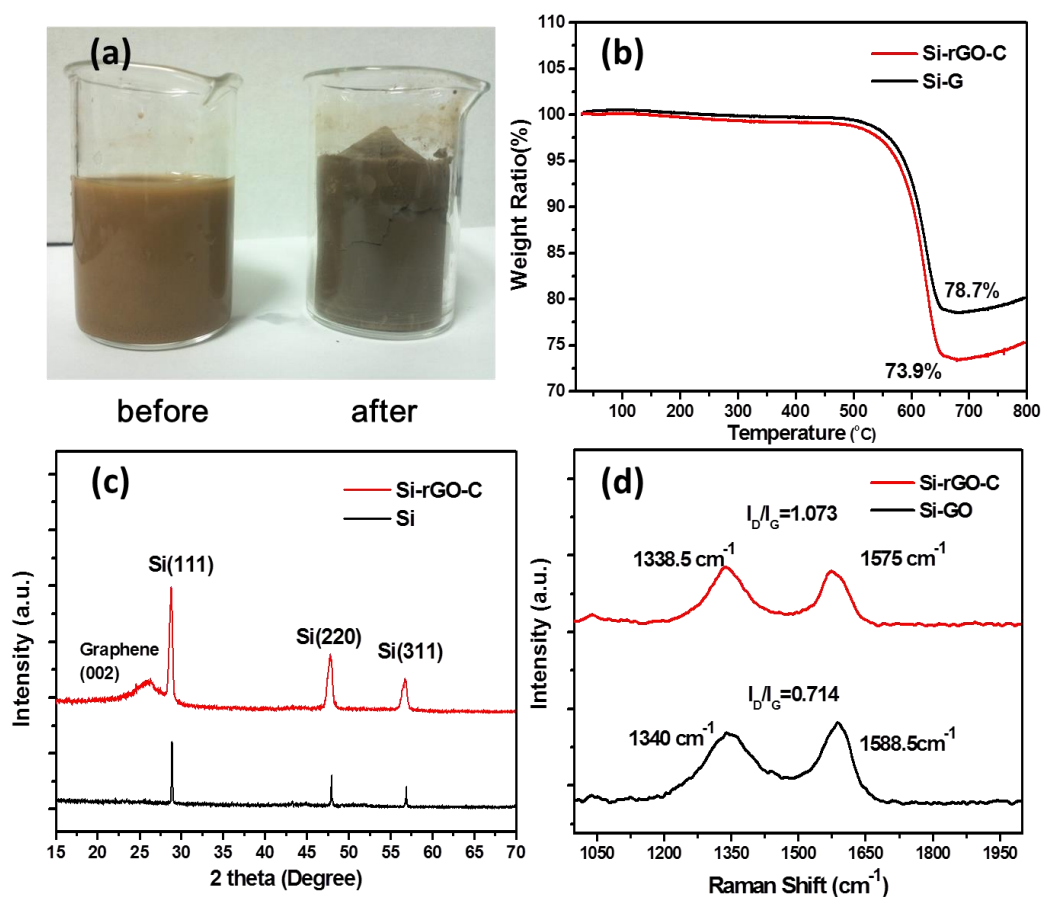


Figure 4.2 (a) Optical images of Si-GO mixture before (left) and after (right) freeze-drying process. (b) TGA curves of Si-rGO composite with and without additional carbon coating. (c) XRD data of the as-obtained Si-rGO-C composite. (d) Raman spectra of D bands and G bands from Si-GO and Si-rGO-C composites.

TGA analyzes the total amount of carbon content in the final product, including both rGO and added carbon. It is shown in Figure 4.2b that the total carbon content in Si-rGO-C is 26.1%. Without the CVD carbon coating process, the Si-rGO composite contains 21.3% carbon, which is attributed purely to rGO. The overall added carbon by CVD in the Si-rGO-C is calculated to be 5.7%. The characteristic peaks of crystalline Si from XRD in Figure 4.2c corresponds to cubic Si (JCPDS 27-1402) and confirms that Si NPs maintain their crystallinity after vigorous mixing in aqueous solution and treatment at high temperatures, verifying there is no side

reaction during the synthesis procedure. A broad peak at around 26° confirms that GO is successfully reduced to rGO. No other peaks can be observed from the XRD result, suggesting that no side product such as Si carbide is formed during the process.

Raman spectroscopy is capable of investigating crystal structures of carbonaceous materials. D and G bands ($\sim 1350\text{ cm}^{-1}$ and $\sim 1580\text{ cm}^{-1}$, respectively) are well-known characteristic peaks for carbonaceous materials; they represent the defects/disorder and graphitized structure of carbon, respectively.¹³¹ I_D/I_G ratio is a value commonly used to estimate the relative amount of defects in a carbonaceous sample. This is because the G-band is associated with E_{2g} breathing mode of sp^2 carbon atoms in the conjugated structure, while the D-band is associated the A_{1g} breathing mode at domain boundaries (specifically from armchair edge defects). As shown in Figure 4.2d, the ratio of I_D/I_G increases from 0.714 to 1.073 after the high temperature treatment, which means the defects/disorder in the carbon material increase with the reduction of GO and the implementation of additional carbon. This indicates that the rGO-carbon matrix contains a significant amount of disordered sp^2 carbon, which may be due to the GO reduction process that can partially break the sheets and increase the amount of edge defects. The reduction of GO to rGO can therefore lead to a higher electron conductivity, and higher porosity Li diffusion, which can improve the overall rate capability and stability of the electrode.¹³²

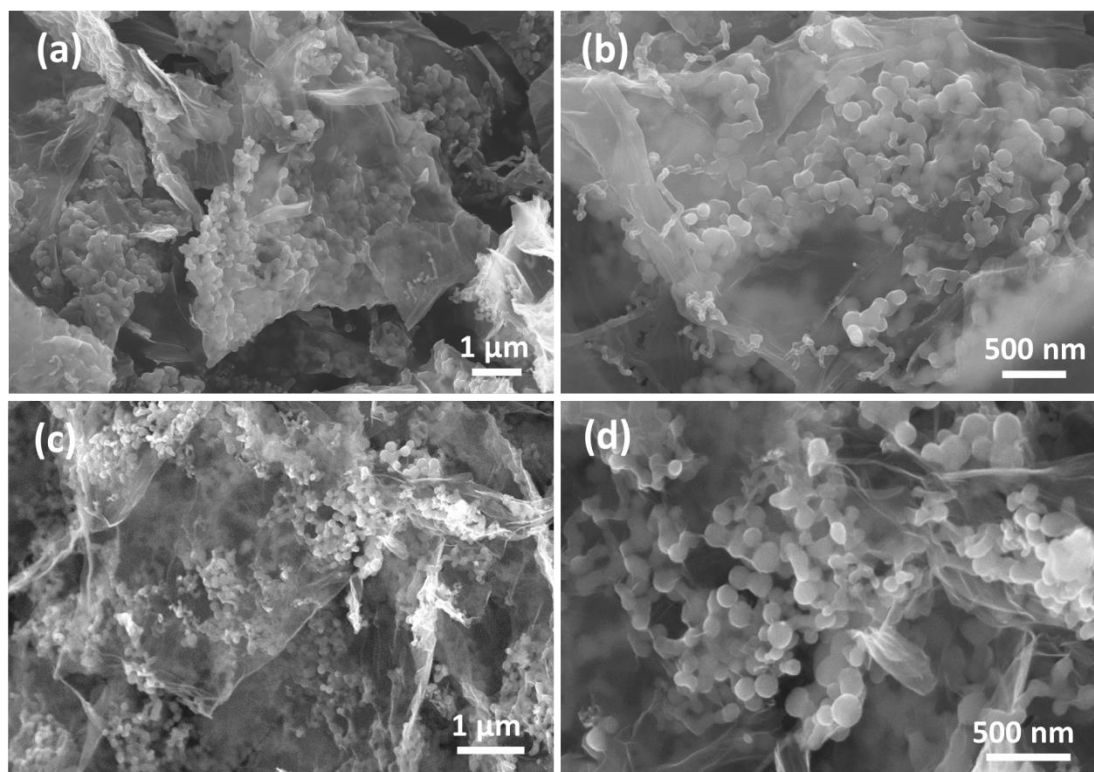


Figure 4.3 SEM images of a typical site of Si-rGO-C composite with a whole piece of rGO flake(a), a close view of Si-rGO-C composite including branched carbon with Si NPs wrapped with rGO sheets (b), a typical site of Si-rGO composite (c), and Si-rGO composite with higher magnification (d).

The morphology of Si-rGO composite with and without CVD carbon coating was obtained with SEM and is shown in **Figure 4.3**. Figure 4.3a shows that the size of a typical rGO sheet wrapping the Si NPs is between 1 and 10 μm . The sheet with Si NPs is interconnected with other sheets by both overlapping sheets and carbon branches. These additional electron pathways provide the composite with enhanced conductivity on a macroscopic level. Figure 4.3b shows the carbon branches with an average length of several hundred nanometers, and a diameter of 30-40 nm. Most of the carbon branches are closely embedded onto the rGO sheets and some also intertwine with Si NPs. The branches at the edge of the rGO sheets successfully

bridge the gaps between these sheets, which may provide better electron conductivity in the composite. In comparison, Si-rGO composite without carbon coating in Figure 4.3c has no carbon branches in between rGO sheets or Si NPs. Si NPs on the rGO sheets appear to be more dissociative from the rGO sheets, while Si NPs in the Si-rGO-C composite are tightly implanted onto the rGO sheets and added carbon. Figure 4.3d is a typical view of Si-rGO composite with the initial Si:GO ratio of 2:1. It can be observed that the Si NPs aggregate on the rGO sheets, with no additional carbon shown.

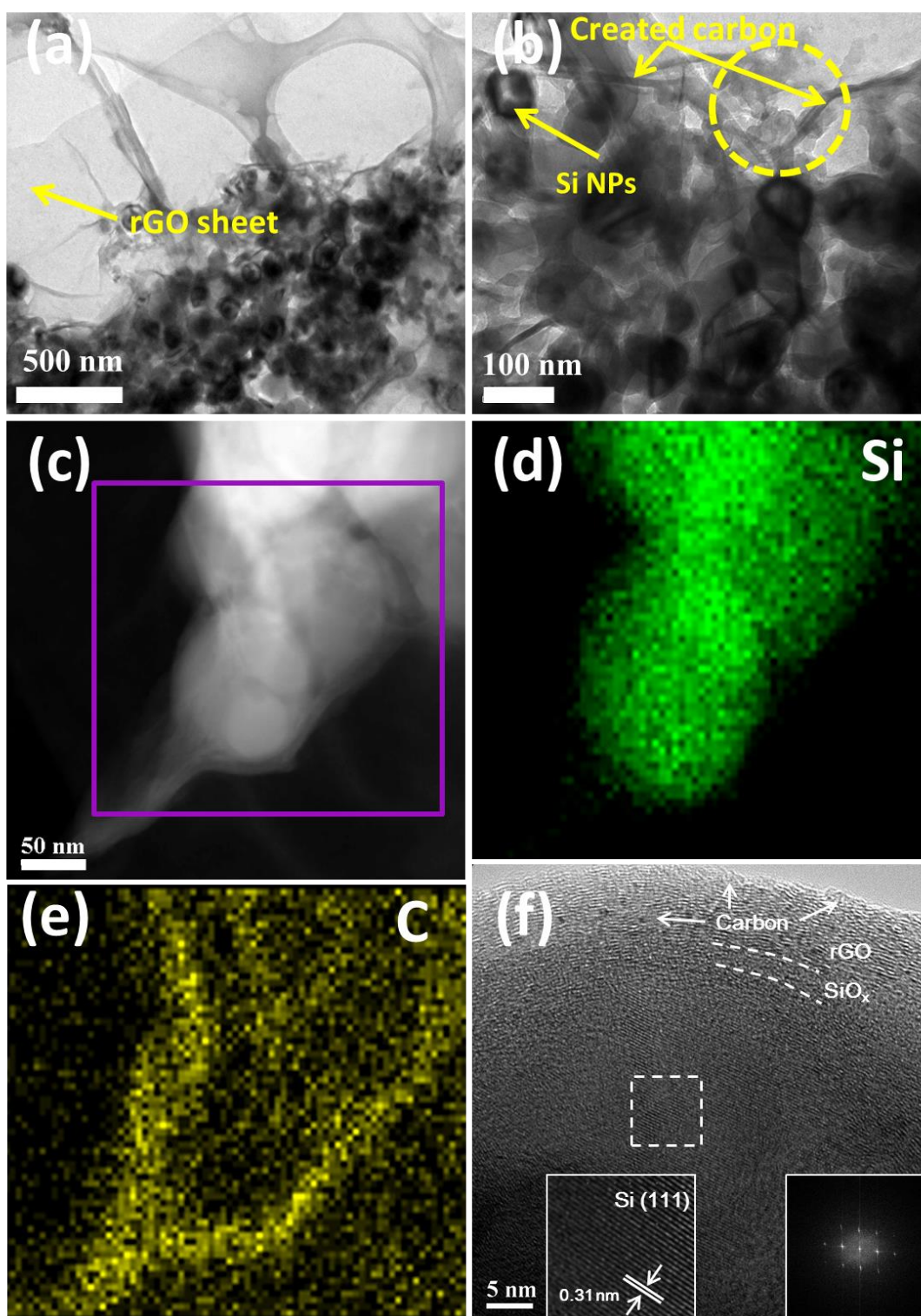


Figure 4.4 (a) TEM image of Si-rGO-C composite at low magnification with the grid of TEM holder in view. (b) A zoomed-in TEM image of (a) with detailed features of Si-rGO-C. (c) Dark field TEM image of Si-rGO-C composite with higher resolution, (d) EDX mapping of element

Si for the area marked in (c), (e) EDX mapping of element C for the area marked in (c), and (f) HRTEM image of Si-rGO-C composite with insets of increased magnification TEM image and FFT pattern of the selected area.

A typical part of the Si-rGO-C sample was shown in the low-magnification TEM image in **Figure 4.4a**, the area with Si NPs appears darker compared to the area with only flattened rGO layer. Figure 4.4b clearly shows the existence of created carbon branches and stuffed carbon on the rGO sheet and in between the Si NPs. Figure 4.4c shows an area of Si-rGO-C composite with only a few particles in view, from which EDX element mapping of Si and carbon is revealed in Figure 4.4d and Figure 4.4e, respectively. Stronger signals from Si come from areas where particles overlap. Element mapping of carbon in Figure 4.4e provides a clear distinction between areas of different carbon densities. The relatively brighter signal from the edges of Si NPs demonstrates that carbon and rGO enclose Si along the arc of spheres, further confirming good contact and wrapping of both rGO and carbon on Si NPs. Figure 4.4f is the high resolution TEM (HRTEM) image of the Si-rGO-C composite. The d-spacing of the (111) plane is 0.31 nm, and the fast Fourier transform (FFT) from the inset confirms that the crystallinity of the Si NPs is mostly retained. A thin layer of amorphous SiO_x (around 4 nm) can be observed from the HRTEM image as well. rGO is closely attached to the SiO_x shell, with amorphous carbon deposited on the surface of the composite.

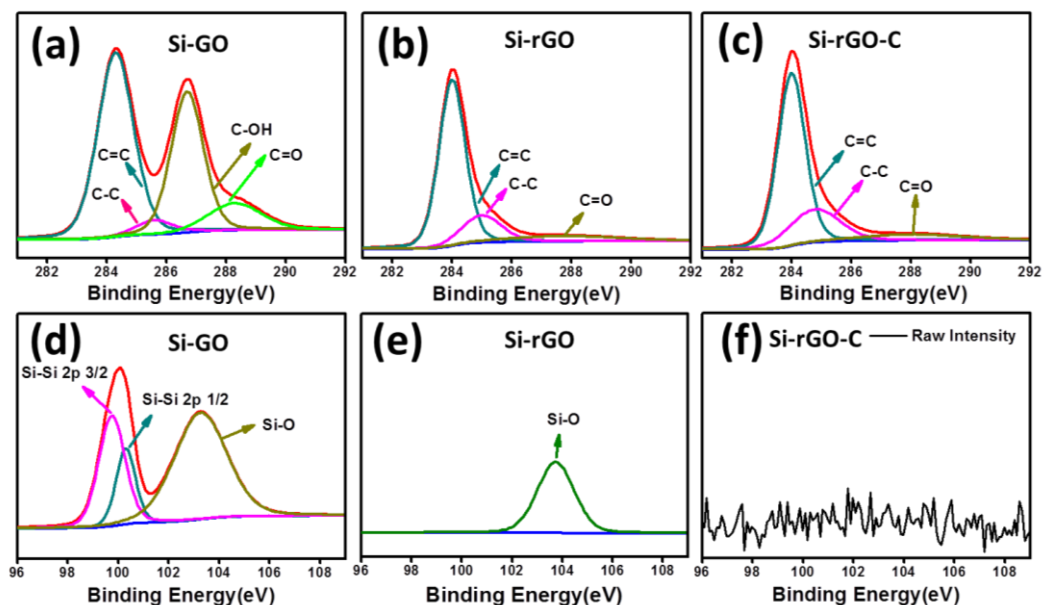


Figure 4.5 XPS spectra of C (a, b, and c) and Si (d, e, and f) for Si-GO (a and d), Si-rGO (b and e), and Si-rGO-C (c and f) composites.

To further investigate the change of GO during the high temperature process and confirm the successful implantation of carbon into Si-rGO composite, X-ray photoelectron spectroscopy (XPS) was conducted with Si-GO, Si-rGO, and Si-rGO-C samples. Gaussian-Lorentzian fitting and Shirley background correction were adopted for all spectra except for Si-rGO-C, where no obvious Si signal was detected. As shown in **Figure 4.5a**, the C 1s peak at 284.7 eV and C 1s peak at 286.7 eV represent the chemical state of sp^2/sp^3 C-C bonding and C-O bonding respectively.¹³³ C=O peak is observed at around 288.5 eV. The intensity ratio of C-C bonding over C-O bonding increases dramatically upon the high temperature reduction process (Figure 4.5 b and c). As shown in Figure 4.5d, both elemental Si peaks of Si 2p_{1/2} and 2p_{3/2} and Si-O peaks can be easily found in Si-GO composite. Only one Si-O peak can be observed in the spectra of Si-G (Figure 4.5e), while no obvious Si signals are shown in Si-rGO-C spectra (Figure 4.5f). This could be explained by the partial oxidation of Si NPs and thus the

increase of SiO_x layer during the reduction of GO. The diminished Si signal in Si-rGO-C spectra is attributed to the thickness increase of carbon shell on Si NPs as the XPS adopted can only detect a few nanometers from the surface of the sample. This also confirms the good wrappability of carbon on the surface of Si NPs. The carbon shell around Si NPs can help form a stable SEI and protect the material from severe structure deterioration during cycling and result in the improved performance of Si-rGO-C over Si-rGO.

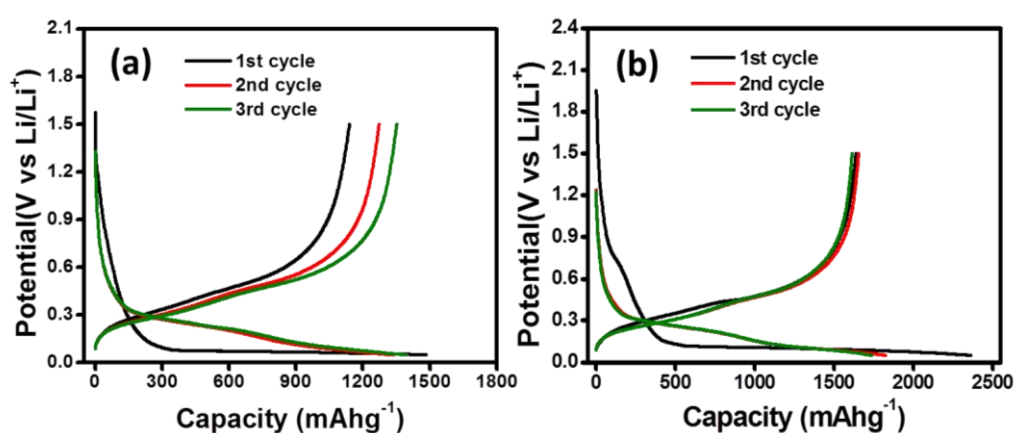


Figure 4.6 Charge and discharge profiles of Si-rGO-C (a) and Si-rGO (b) of first three cycles.

Charge and discharge profiles of the Si-rGO-C composite are shown in **Figure 4.6a**. The gravimetric capacity of Si-rGO-C increases to 1352 mAh g^{-1} from its initial value of 1139 mAh g^{-1} . Here the Si-rGO-C electrode material contains 80% of active material (80% active material, 20% binder), while the reference Si-rGO electrode only contains 70% of Si-rGO (20% binder, 10% carbon black). Thus the specific capacity of Si-rGO-C electrode based on the whole electrode material is calculated to be 911.2 mAh g^{-1} for the first discharge and $1081.6 \text{ mAh g}^{-1}$ in the third cycle. All other values of gravimetric capacity were calculated based on the mass of Si-rGO-C, Si-rGO, or bare Si for direct comparison among active materials. The capacity increase of Si-rGO-C cell continued for more than 30 cycles, and the phenomenon is detailed

in the discussion of cycling performance below. The discharge profile changes from a very flat plateau at around 0.1 V to a slowly descending curve from 0.3 V to the low cut-off voltage. This is due to the transformation of the crystalline Si to the amorphous Si after Li insertion and extraction process.¹³⁴ Figure 4.6b shows the charge and discharge profiles of Si-rGO without additional carbon. During the first three cycles, the charge capacity of the Si-rGO electrode is almost stabilized at 1630 mAh g⁻¹, with no observable increase in capacity. The capacity difference between the first discharge and charge is 344.1 mAh g⁻¹, (23.2%) for Si-rGO-C, and 724.7 mAh g⁻¹ (30.7%) for Si-rGO. These results show that the Si-rGO-C electrode has a higher CE than Si-rGO in first cycle, providing a higher Li utilization rate.

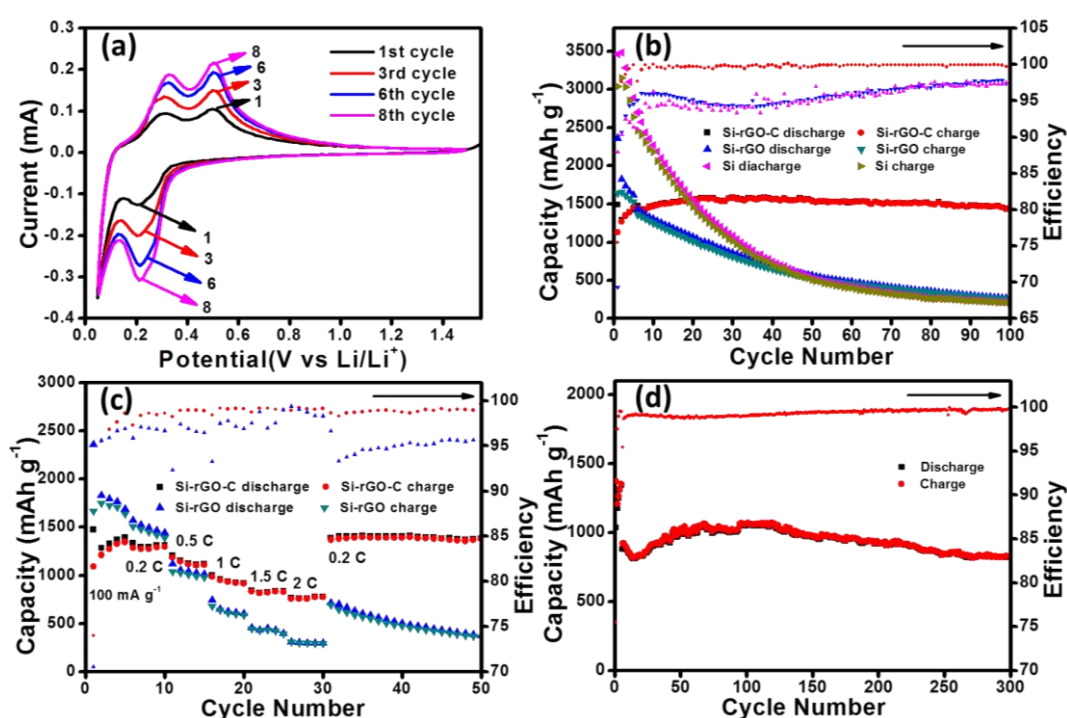


Figure 4.7 (a) CV test of the Si-rGO-C composite with 1st, 3rd, 6th and 8th cycles shown. (b) Cycling performance of Si-rGO-C, Si-rGO composites, and bare Si at 0.2C following activation. (c) Rate capability tests for Si-rGO-C and Si-rGO composites. (d) Long-term cycling performance of Si-rGO-C composite at 1C following activation.

The charge and discharge behavior of the Si-rGO-C electrode was further investigated using a CV test, shown in **Figure 4.7a**. The first broad cathodic peak at around 0.22 V corresponds to the lithiation of crystalline Si and the formation of amorphous Li_xSi .¹³⁴ In the anodic scan, the two peaks at 0.31 V and 0.5 V are due to the reversible delithiation of the active material. From the second cycle, the positions of both anodic and cathodic peaks remain almost unchanged, indicating that the lithiation/delithiation processes are highly reversible. The strengthening peaks in the following cycles are in agreement with the charge and discharge profiles and the cycling data that show a capacity increase during the initial cycles. This phenomenon is attributed to the gradual kinetic activation of Si upon Li alloying/dealloying.

The cycling data of the Si-rGO-C and Si-rGO composites are shown in Figure 4.7 b and c. It is noted that the batteries are tested 5 cycles at 100 mA g^{-1} for initial stabilization procedure of each composite. According to the capacities of batteries after activation/aging process, the 1 C rates of Si-rGO-C and Si-rGO are determined to be 1400 mA g^{-1} and 1600 mA g^{-1} , respectively.

Cycling tests were conducted to obtain the cycling and rate performance of Si electrodes. As shown in Figure 4.7b, it should be noted that the capacity of Si-rGO-C increases in the initial 25 cycles from its initial value of 1139 mAh g^{-1} to a maximum of 1570 mAh g^{-1} (a 38% increase). After 100 cycles, the capacity of the Si-rGO-C composite remains at 1445 mAh g^{-1} , which is much higher than its initial capacity. Si-rGO shows a higher capacity than Si-rGO-C in the first few cycles. However, Si-rGO is quickly surpassed by Si-rGO-C due to its dramatic degradation after only five cycles. A cell made from commercial Si NPs is maintained at 100

mA g⁻¹ throughout the test. Although the initial discharge capacity of bare Si NPs reaches around 3500 mAh g⁻¹, the stability is much worse than the other two materials.

The areal capacity of the Si-rGO-C electrode is around 1.6 mAh cm⁻², based on the specific gravimetric capacity after 100 cycles at 0.2 C and the areal mass loading of active material on the substrate. The electrode density was measured to be 0.92 g cm⁻³ from the mass, area, and thickness of the electrode. And the volumetric specific capacity was calculated to be 1373 mAh cm⁻³ based the electrode density and the areal capacity. Although the electrode density is lower than that of commercial graphite electrode (1.4 g cm⁻³), the volumetric specific capacity of Si-rGO-C electrode is much higher than that of graphite electrode (490 mAh cm⁻³).⁹⁸ This can lead to a significant advantage in volumetric energy density for Si-rGO-C electrode considering the similar operating potentials of Si full cells and graphite full cells.

Figure 4.7c reveals the rate capability of the Si-rGO-C and Si-rGO composites. After initial activation at 100 mA g⁻¹ for 5 cycles, the electrodes are tested at 0.2 C, 0.5 C, 1 C, 1.5 C, 2 C, and then 0.2 C again. The capacity of the Si-rGO-C electrode continues increasing until it is stabilized at 0.2 C with a capacity of 1290 mAh g⁻¹. Gradual decline of the cell's capacity can be observed with the increase of charge and discharge rates. However, Si-rGO-C stabilizes at higher rates (e.g. 1.5 C and 2 C). At 2 C (2.8 A g⁻¹), the electrode presents a capacity of 770 mAh g⁻¹. When the cell is tested at a lower rate of 0.2 C, it recovers its capacity of 1380 mAh g⁻¹ and remains highly stable. In comparison, the Si-rGO composite degrades quickly even at low rates of 100 mA g⁻¹ and 0.2 C. The capacity of Si-rGO falls below that of Si-rGO-C when the charge and discharge rate is raised to 0.5 C. The difference in capacity between the two

composites continues to increase at higher C rates. When the rate is set back to 0.2 C, the capacity of Si-rGO (691 mAh g⁻¹) is approximately half that of the Si-rGO-C composite. At this point, Si-rGO-C still performs stable cycling while Si-rGO continues to decay at 0.2 C. Figure 4.7d illustrates the long-term cycling performance of the Si-rGO-C electrode at 1 C after initial activation at 100 mA g⁻¹. Phenomena similar to that of the cell at 0.2 C are observed. After 300 cycles, the cell still retains a capacity of 840 mAh g⁻¹, which corresponds to 79% retention compared to its peak capacity and 94% retention compared to its original capacity at a rate of 1 C.

The CEs for Si-rGO-C cells increase from around 75% in first cycle to more than 99.5% for both cycling tests and 99% for rate test, while batteries from bare Si and Si-rGO present much lower coulombic efficiencies. The high and stable coulombic efficiency of Si-rGO-C cells can be attributed to the stable structure of the electrodes and minimized side reactions during cycling. But it is interesting to notice that the initial coulombic efficiency for bare Si electrode is higher than that of Si-rGO-C. The relatively low initial irreversible capacity of bare Si electrode can be explained by the fact that bare Si electrode contains a lower ratio of carbon, which contributes to much of the irreversible capacity in first cycle.

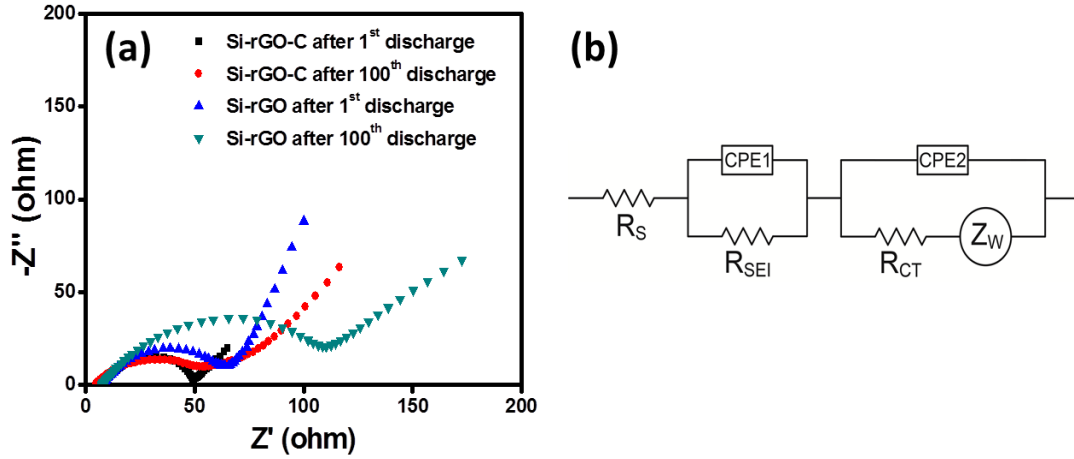


Figure 4.8 (a) Impedance measurements for Si-rGO-C and Si-rGO composites after 1st and 100th discharges, (b) The equivalent circuit model.

To further understand the effect of additional carbon on the electrochemical performance of Si-rGO-C composite in LIBs, electrochemical impedance spectroscopy (EIS) measurements were conducted after 1st and 100th discharges of both Si-rGO-C and Si-rGO composites at 0.2 C (**Figure 4.8a**). The equivalent circuit model is shown in Figure 4.8b. The high frequency x -intercept corresponds to the equivalent series resistance, R_s . The value represents Ohmic resistance, with contributions from electrical contact resistance in the outer circuit, current collectors, electronic conductivity of electrodes, and ionic conductivity of bulky electrolyte. The semi-circle corresponds to the combined SEI resistance (R_{SEI}) and charge transfer resistance (R_{CT}). R_{SEI} measures the ionic diffusion resistance of Li^+ in the SEI layer and is the main parameter of interest. R_{CT} represents the charge transfer resistance of the electrode/electrolyte interphase. CPE1 and CPE2 represent the capacitance of the SEI layer and the electrode/electrolyte interphase, respectively. The low frequency tail is associated with the Warburg diffusion impedance (Z_W) from the Li-diffusion process.¹³⁵

Table 4.1: Impedance parameters for Si-rGO-C and Si-rGO electrodes after 1st and 100th cycles.

Electrode	R_s/Ω	R_{SEI}/Ω	R_{CT}/Ω
Si-rGO-C 1 st discharge	7.291	37.1	3.623
Si-rGO-C 100 th discharge	4.454	49.58	18.5
Si-rGO 1 st discharge	7.911	59.95	1.013
Si-rGO 100 th discharge	7.695	116.1	64.98

The fitted impedance data can be seen in **Table 4.1**. R_s values for all electrodes are similar because the same fabrication procedure and battery components were used. R_{SEI} of the Si-rGO-C composite after 1st discharge is 37.1 Ω , and the value slightly increases to 49.58 Ω after 100 cycles. R_{SEI} of Si-rGO electrode increases from 59.95 Ω to 116.1 Ω from 1st discharge to 100th discharge. These results show that the Si-rGO-C electrode maintains a much more stable SEI layer than Si-rGO upon cycling. The final value of R_{CT} for Si-rGO-C is smaller than that of Si-rGO, and the change of Si-rGO-C's R_{CT} upon cycling is much smaller than that of Si-rGO, indicating that the incorporation of additional carbon can help maintain the electrode's structure and ensure the rapid electron transfer during the electrochemical Li insertion/extraction process. These results reveal that the addition of carbon into Si-rGO successfully provides efficient and stable electron and ion conductive pathways.

4.4 Summary

In summary, a Si-rGO-C composite was designed with Si NPs well wrapped by an rGO/carbon hybrid. The Si-rGO-C composite successfully resolved the problem by facilitating

the wrapping of Si NPs and interconnecting rGO flakes by CVD carbon implantation. CVD carbon coating enhances battery performance by forming carbon branches on rGO and Si, which facilitates electron transport in the electrode. The additional carbon also provides structure integrity to the composite, and helps form a stable SEI layer over repeated lithiation/delithiation process. The composite successfully delivered improved cycling performance compared to Si-rGO composite. The Si-rGO-C obtained a capacity of 840 mAh g⁻¹ (94% retention) after 300 cycles at 1 C. Rate capability testing further presented a capacity of 770 mAh g⁻¹ at 2 C. These results bring forward the idea of obtaining the benefits of Si nanonization, while mitigating the negative effects of nanotechnology. However, adoption of rGO will most likely pose as a problem for wide commercial application. Based on these concepts/design criteria, the other two projects were conceived and will now be presented.

5. Formation of Micron-sized Spherical Particles from Si NPs

5.1 Introduction

As introduced in Chapter 2 and Chapter 4, the recent rapid development of nano-sized Si materials, such as Si nanowires¹³⁶, nanotubes¹³⁷, has effectively mitigated the mechanical failure and improved the cycle efficiency.^{4, 138} Various Si composites, especially Si-carbon composites, have also been demonstrated to have extended cycle life.¹³⁹ Carbon coating/filling¹⁴⁰, graphene encapsulation^{126, 129}, Si-C core-shell/yolk-shell designs^{141, 142}, and other reported strategies have been suggested as a few other effective approaches to address the issues with Si anodes, including volume change, conductive point loss, and SEI instability.¹⁴³ However, the practical application of these delicately engineered nanostructures and elaborate composites remains challenging since they usually involve very high processing cost and difficult to be scaled up. Moreover, nano-sized Si or Si composites are often plagued with low tap density, large contact area with electrolyte, and low CE.¹⁴⁴ It is highly desirable to fully take advantage of the benefits from nanostructures and composite designs, while circumventing the disadvantages (discontinuous electrical conductive pathways, fabrication complexities and high cost) of nanonization. Magasinski et al. reported a hierarchical bottom-up approach in the synthesis of a Si/C nanocomposite.⁹² Nano Si was first deposited on carbon black via CVD using silane. A second carbon CVD step was carried out to assemble the intermediate product into secondary granules. Inspired by pomegranate structure, Liu et al. synthesized a spherical Si/C composite via an evaporation-driven self-assembly method.¹¹⁸ Si NPs are well embedded inside the interconnected carbon spheres that form the micron-sized particles. A watermelon-like Si/C microsphere composite was reported by Xu et al. via a spray-

drying process, followed by a subsequent calcination and carbon deposition at 900 °C.¹⁴⁵ Flake graphite and Si NPs are encapsulated inside a carbon shell in the synthesized microspheres. While these techniques all attempt to mitigate the disadvantages of nanonization, their high production temperatures will undoubtedly be a burden for any commercial applications.

To circumvent those issues discussed above, we have successfully developed a novel secondary micron-sized Si-based composite (MSC), with Si NPs (diameter ~70 nm) embedded in a porous, conductive and elastic network constructed with carbon, and cured-and-crosslinked functional binder materials. This design embodies several key advantages as a LIB anode material. (1) Si NPs utilized as primary capacity contributor fully addresses the pulverization issue plaguing Si anodes; (2) Carbon network formed by carbon nanotubes and conductive carbon provides both sufficient contact points with Si and long-range conductive paths throughout the spheres; (3) Crosslinked functional binder contributes to the stability and robustness of the secondary structure via both physical and chemical bonding; (4) Volume expansion of Si over lithiation/delithiation can be well accommodated by voids inside the structure; (5) Tap density of the nano-sized Si is significantly improved via the formation of secondary micron-sized particles. More importantly, this facile one-step methodology does not require high temperature carbonization and is implemented with a highly scalable spray-drying process.

5.2 Experimental Methods

5.2.1 Material Synthesis:

All chemicals in this work were used as received. Nano-sized Si NPs were first dispersed

with CMC and PAA in distilled de-ionized (DDI) water. Conductive carbon Ketjenblack and CNTs were dispersed in DDI water in a separate container. Both dispersions were sonicated and stirred for 5 h to avoid agglomeration and achieve good dispersion. After that, the two dispersions were mixed together and stirred for another 2 h before being subjected to the spray-drying process. A peristaltic pump was used to feed the spray drying machine. A tube furnace with inert argon atmosphere was used to heat-treat samples at temperatures of 200, 250, and 900 °C. The ramp rate of the furnace was programmed to be 2 °C per minute, and the heating plateau for each temperature was set to be 3 h. The yield of the synthesis of MSC250 was between 40-50%.

5.2.2 Physical Characterizations:

Thermal gravimetric analysis (TGA, Q500, TA Instrument) was conducted to determine the content of Si in the composites. TGA was performed in air atmosphere with an initial temperature of 30 °C and final temperature of 800 °C, and the ramp rate was 10 °C/min. Differential scanning calorimetry (DSC, Q2000, TA instruments) was conducted to study the thermal behavior of polymers that were utilized in this work. Fourier-transform infrared spectroscopy (FTIR, Nicolet 6700, Thermo Scientific) was used to detect functional groups in samples. Raman spectroscopy of samples was obtained from a Bruker Senterra device, using a 532 nm laser. The surface area and pore volume of the synthesized materials were measured by Brunauer-Emmett-Teller (BET) and Barrett-Joyner-Halenda (BJH) methods, respectively, using a surface area and porosimetry analyzer (Micromeritics ASAP 2020). X-ray photoelectron spectroscopy was applied to study the binding energies of some chemical bonds

and electronic structures in MSC composites. SEM used to observe the morphology of samples in this work was Zeiss Ultra Plus. TEM (JEOL 2010F) was used to further study the morphology, especially at high resolutions. An energy-dispersive X-ray spectroscopy (EDX) device coupled with the TEM was used to obtain the element mapping, as well as a rough quantitative element analysis of several key elements, such as Si, C, and O.

5.2.3 *Electrochemical Measurements:*

The electrochemical performances of MSC250 as well as control samples were analyzed in coin cells using Li as both a counter and reference electrode. Electrodes for coin cells were fabricated by casting the slurry consisting of 80 wt% active material, 10 wt% super-P conductive carbon, and 10 wt% CMC binder dissolved in water onto a copper foil substrate. After casting, the copper foil was preheated in a 60 °C oven for 2 h and then transferred into a 100 °C vacuum oven and dried for 12 h. Disk-like electrodes (12 mm diameter) were cut from the cast copper foil and carefully pressed. The mass of active material was taken for each electrode before the fabrication of coin cells in argon-filled glovebox (Mbraun, H₂O, O₂ less than 0.5 ppm). The electrolyte used in this project was a 1 M Li hexafluorophosphate (LiPF₆) solution with solvent composition of 27% ethylene carbonate (EC): 63% diethyl carbonate (DEC): 10% fluoroethylene carbonate (FEC) by volume. The separator placed in between cathode and anode in this work was a type 2400 polypropylene membrane from Celgard. Fresh coin cells were aged at room temperature for 12 h before being subjected to various tests. Galvanostatic charge/discharge tests were performed on a Neware battery testing system at room temperature. The voltage window for all Si half cells was 0.01-1.5 V, and the initial

current density for all cells was set to be 0.1 A g^{-1} . C-rates of all materials are defined by the stabilized discharge capacity at 0.1 A g^{-1} of each material. CV and potentiostatic EIS curves were obtained from a Princeton Versastat electrochemical workstation. The scanning rate of CV was 0.1 mV s^{-1} , and the voltage window was 0.01-1.5 V, starting from open circuit voltage. The frequency range of the EIS tests was from 1 MHz to 0.1 Hz, and the amplitude of the perturbation voltage was 10 mV. To evaluate the properties of MSC250 electrodes in full-cell LIBs, commercial cathode, with an average areal loading of 19.8 mg cm^{-2} and nominal capacity of 170 mAh g^{-1} was utilized to pair up with the MSC250 anode. The areal loading of the MSC250 anode was controlled to be 2.8 mg cm^{-2} to have negative/positive ratio (N/P ratio) of ~ 1.1 . The electrode cutting and drying process, as well as the coin-cell fabrication process is identical to that of half-cell fabrication.

5.3 Results and Discussions

A brief schematic illustration of the fabrication process and the obtained MSC composite is shown in **Figure 5.1a**. First, Si NPs along with the water-soluble PAA and sodium CMC polymers are dispersed in water. Si NPs exhibit good hydrophilicity and disperse well in the system, without significant sedimentation. CNTs and Ketjenblack carbon (KB) are vigorously stirred and sonicated in heated water (60°C) to reduce agglomeration. These two mixtures are subsequently mixed together and alternatively sonicated and stirred until all components are well dispersed. The mixture is then subjected to a continuous spray-drying self-assembly process, with feed being charged to the drying chamber by a peristaltic pump. The obtained MSC powder is then placed in a furnace at 250°C for binder polymers to cure and crosslink.

The final product, denoted as MSC250 is collected with a yield of 40-50%, and later used directly as electrode active material. For comparison, three control samples were prepared under different conditions. A lower temperature of 200 °C was used in the curing process, with other parameters being the same, and the product is named as MSC200. The last control sample is based on MSC, which undergoes an annealing process in argon atmosphere at 900 °C. This sample is denoted as MSC900.

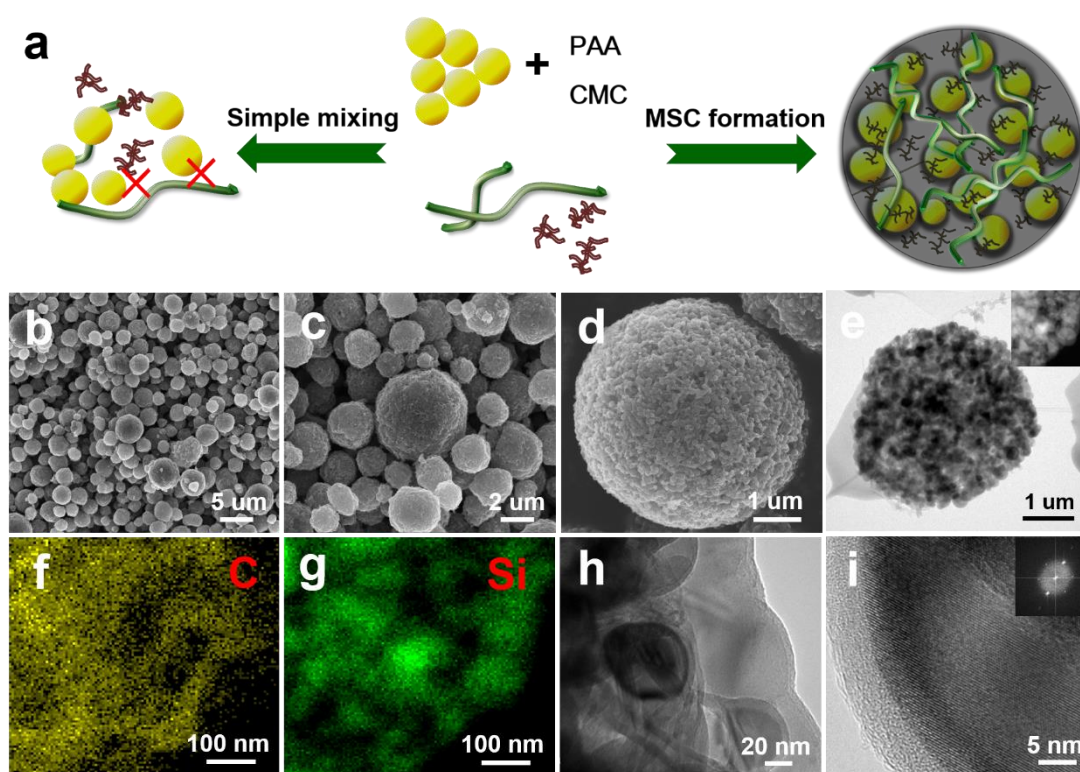


Figure 5.1 a) Schematic illustration of the formation process of MSC250. b-d) SEM images of MSC250 at different magnifications. e) TEM image of MSC250. f-g) C and Si elemental mapping of the area from inset in e). h) TEM image of the edge of MSC250. i) HRTEM image of a single Si NP in MSC250, with FFT inset of the core area.

As shown in the scanning electron microscopy (SEM) imaged in Figure 5.1 b and c, most

MSC250 particles are near-spherical and have a diameter range of 1-6 μm . Multi-sized particles provide better stacking in electrodes over uniform particles since vacancies among particles can be effectively reduced and excellent fluidity of powders can be achieved. This helps improve the electrode density, as well as volumetric capacity since more active materials can be loaded on current collector compared to nano Si. The volumetric density of the MSC250 electrodes is measured to be 1.1 g cm^{-3} , much higher than that of bare Si electrode, with an volumetric density of only 0.3 g cm^{-3} . The rough surface observed from the SEM and transmission electron microscopy (TEM) images (Figure 5.1 d and e) provides good contact with electrolyte as well as neighbouring conducting units. Energy-dispersive X-ray spectroscopy (EDX) obtained from the same area of the inset confirms universal existence of carbon element and even distribution of Si NPs Figure (5.1 f and g). In a higher-resolution TEM image (Figure 5.1h), Si NPs can be seen entangled with CNTs with conductive carbon scattered around Si particles. High-resolution TEM (HRTEM) image focusing on a single Si NP (Figure 5.1i) reveals an amorphous layer of SiO_2 on the surface of Si NP, covered by the outmost thin polymer layer. Ordered crystal lattice in the core of the particle and the fast Fourier transform (FFT) inset confirm the reserved crystallinity of Si after synthesis.

The secondary structure derived from Si NPs, and the near-normalized size distribution of these particles can effectively increase the tap density. Tap density of MSC250 is measured to be 0.76 g cm^{-3} , which is much higher than that of Si NPs (0.18 g cm^{-3}); visual comparison of packed MSC250 and Si NPs with the same mass is displayed in **Figure 5.2**.

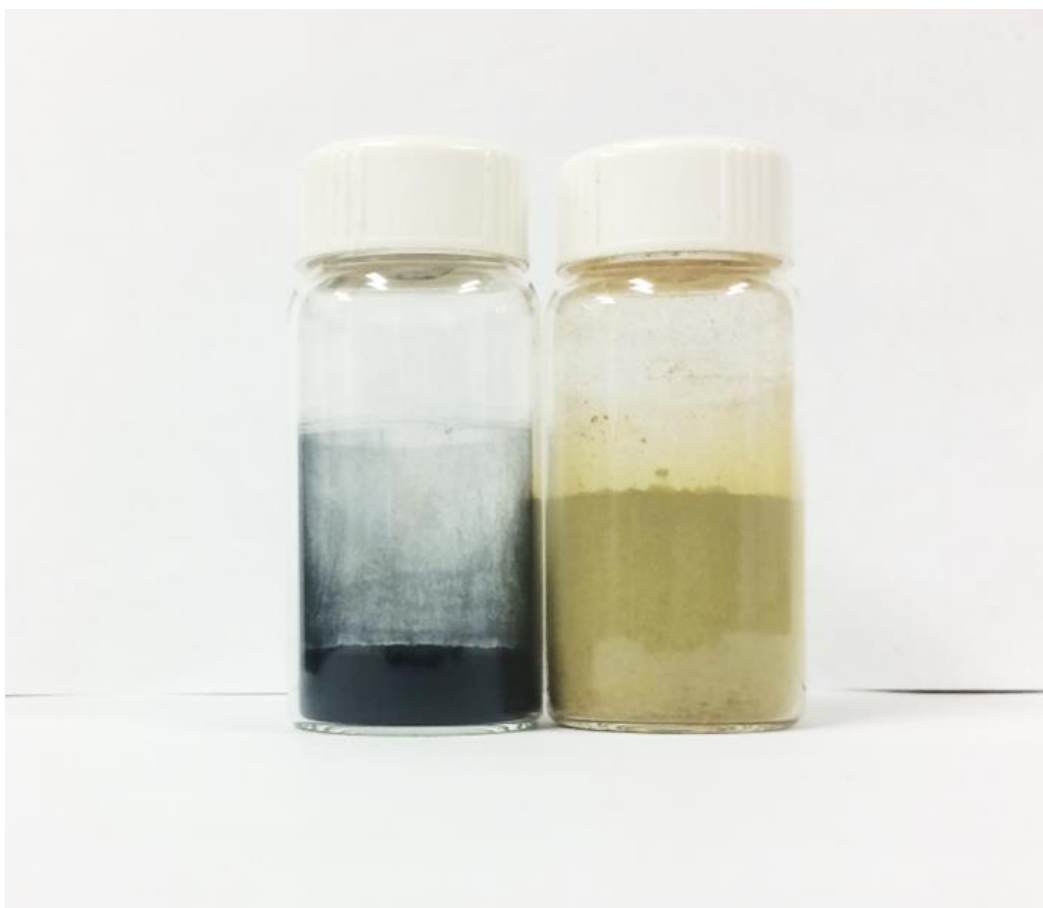


Figure 5.2 Photograph of MSC250 and Si NPs with same mass of 1.8 g.

SEM images and TEM images of Si NPs are provided in **Figure 5.3**. Diameters of most particles are below 100 nm. SiO₂ layer with thickness of ~6 nm on a Si NP can be observed from TEM of a sample prepared via simple mixing of all precursors.

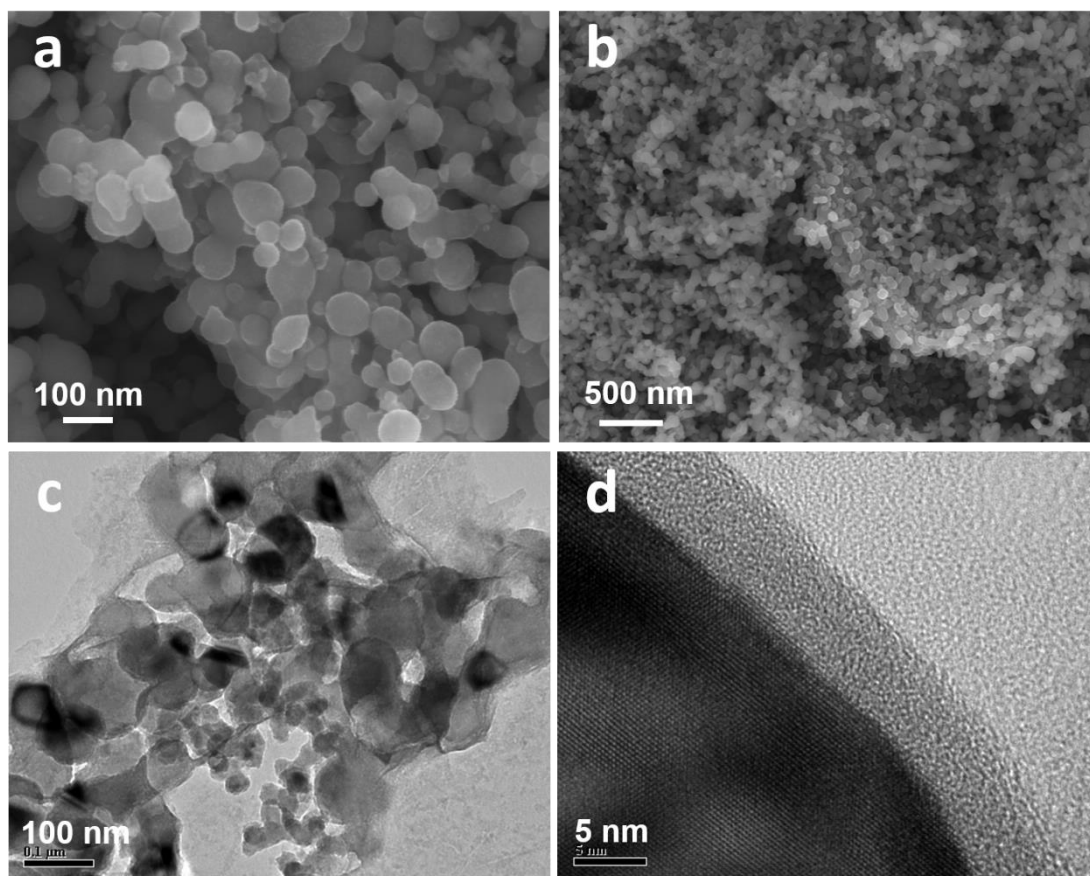


Figure 5.3 a and b) SEM images of Si NPs at different magnifications. c-d) TEM image Si NPs mixed with other precursors via simple mixing, and HRTEM image of a single Si NP.

No significant thickening of the SiO₂ outer shell is observed in MSC250, which proves that Si can survive the spray-drying condition without being further oxidized. This is also confirmed by X-ray diffraction (XRD), as shown in **Figure 5.4a**, which compares MSC250 and bare Si diffraction peaks. Si characteristic peaks remain unchanged in MSC250, with the appearance of a broad peak around 26 ° from embedded carbon. It is worthwhile to mention that the synthetic method does not involve harsh conditions. The 250 °C curing process provides the energy to nebulize the dispersion, turn the binder polymers to be water insoluble, and hold all components together. This process does not need carbonization. The electronic conductivity of the composite is mainly contributed by KB and carbon nanotubes, which

provide abundant short-range and long-range conductive channels. This strategy avoids high-temperature carbonization, simplifies fabrication process, and saves energy.

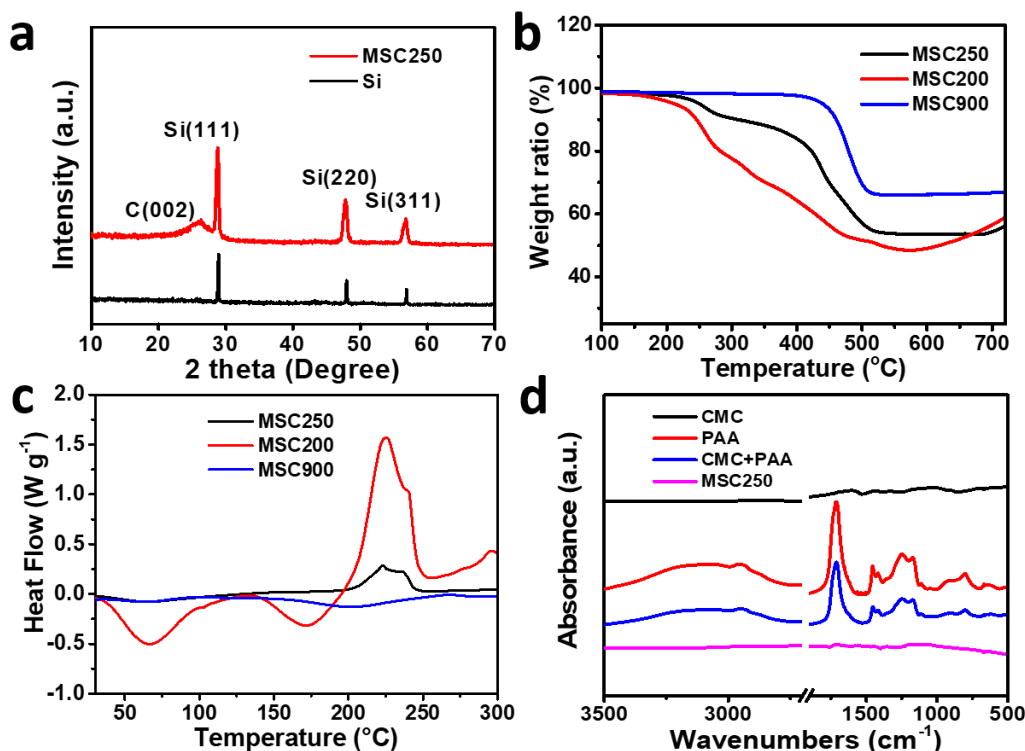


Figure 5.4 a) XRD patterns of MSC250 and Si NPs. b) TGA curves of MSC250, MSC200, and MSC900. c) DSC curves of MSC250, MSC200, and MSC900. d) FTIR spectra of raw polymer binders and MSC250.

To study the thermal properties and composition of MSC250, thermal gravimetric analysis (TGA) and differential scanning calorimetry (DSC) are conducted with MSC250, control samples, and raw materials. MSC250, MSC200, and MSC900 are analysed in air by TGA with a heating rate of 10 $^{\circ}\text{C}$ per minute from 30 $^{\circ}\text{C}$ to 800 $^{\circ}\text{C}$. As displayed in Figure 5.4b, TGA determines that the Si content in the product is 55%, much higher than the Si ratio of 38% calculated based on the masses of all precursors. This indicates that Si is enriched in the composite after the synthesis. This is probably due to Si NPs with hydrophilic surface acting

as nuclei for the formation of secondary particles, and water-soluble binders precipitate on Si surface along with other ingredients. The first onset of mass loss of MSC250 and MSC200 curves begins at around 200 °C. Less mass loss between 200 °C and 250 °C can be observed with the MSC250 sample compared to that of the MSC200, suggesting the substantial esterification and crosslinking reactions that take place during the formation of MSC250. Another sharp drop of the sample weight occurs slightly before 400 °C. Oxidation of carbon and the remaining polymeric structure initiates slightly above 400 °C and fully completes under 550 °C, as no significant weight loss can be observed from the profiles after 550 °C. MSC900 shows a less complex profile, since the content is mainly Si and C. TGA graph of raw PAA/CMC mixture is displayed in **Figure 5.5a**, the abrupt weight change in the temperature range of 200-250 °C further confirms the major chemical reaction process that takes place in this temperature range. As shown in Figure 5.4c, MSC250, MSC200, MSC900 are studied with a DSC (in the temperature range of 10-300 °C). DSC detects obvious heat absorption of MSC200 between 50 °C and 125 °C, which can be attributed to the glass phase transition enthalpy change of CMC and PAA. There is a second endothermic behaviour associated with MSC200 from 130-200 °C, mainly due to the melting phase transition of CMC and PAA polymers. This behaviour is absent in the MSC250 curve, further confirming that the higher heating temperature causes crosslinking of the polymers and therefore irreversible thermal property change.⁷⁰ A distinct exothermic peak centering at 225 °C, together with another less significant exothermic peak at around 240 °C, corresponding to the crosslinking esterification process, can be observed with both MSC200 and MSC250. The much lower intensity of exothermic peaks from MSC250 can be explained by the fact that there are less functional

groups in MSC250 for esterification after the 250 °C treatment. Derivative weight loss data are plotted in the same graph with TGA results of MSC250 and MSC200 in Figure 5.5b, where significant weight loss of MSC200 can be observed in the temperature range of 200-250 °C.

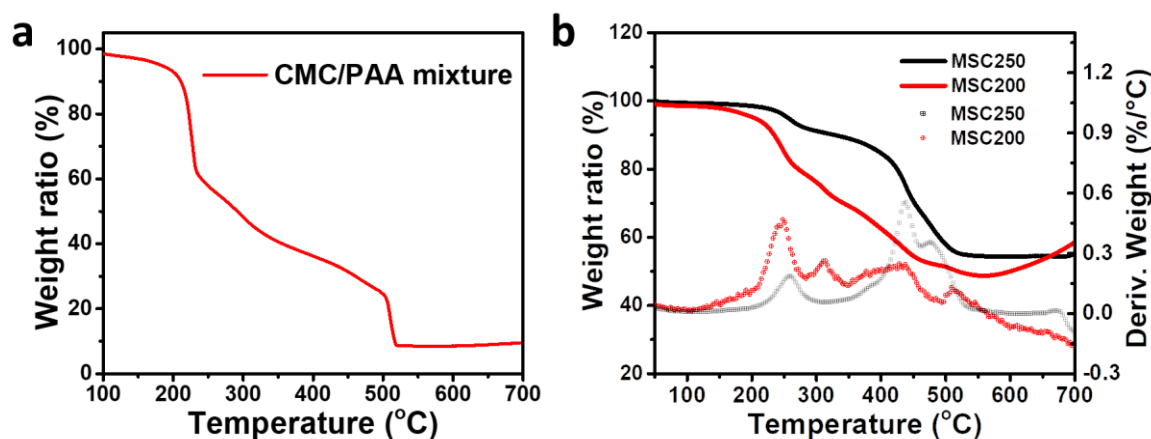


Figure 5.5 a) TGA curve of CMC/PAA mixture in air. b) TGA curves of MSC250, MSC200, and the corresponding derivative weight loss data.

FTIR spectra of raw polymers and the MSC250 are displayed in Figure 5.4d. Compared to CMC, PAA contains more IR responsive groups. The broad band from 3675 cm^{-1} to 3060 cm^{-1} reflects the stretching frequency of hydroxyl ($-\text{OH}$) group and hydrogen bonding from PAA. The strong signal at band 1710 cm^{-1} corresponds to the stretching vibration of carbonyl ($-\text{COO}-$) group. Alkyl $-\text{CH}$ stretching and bending can be evidenced by the signal band centred at 2950 cm^{-1} , and 1450 cm^{-1} respectively. CMC/PAA mixture exhibits similar absorbance pattern to that of PAA alone. The FTIR spectrum of MSC250 shows weaker signal strength compared to that of polymers. This is probably due to the reduced abundancy of IR responsive groups in the composite after the treatment; polymers being constrained inside the composite may also lead to the reduced exposure to IR illumination. Weak $-\text{COO}-$ signal can still be spotted, overlapping with the strong peak at 1710 cm^{-1} from the polymer mixture. Raman

spectra of MSC250, MSC200, MSC900, and bare Si NPs are obtained and shown in **Figure 5.6**. Both Si and C signals are present in MSC250 curve. With Si and carbon as main component, MSC900 shows distinct Si signal and characteristic D and G band of carbon. However, these characteristic carbon peaks are absent in the MSC200 curve, which might be due to aggregation, sedimentation, and inhomogeneous distribution of carbon materials in the evaporation process.

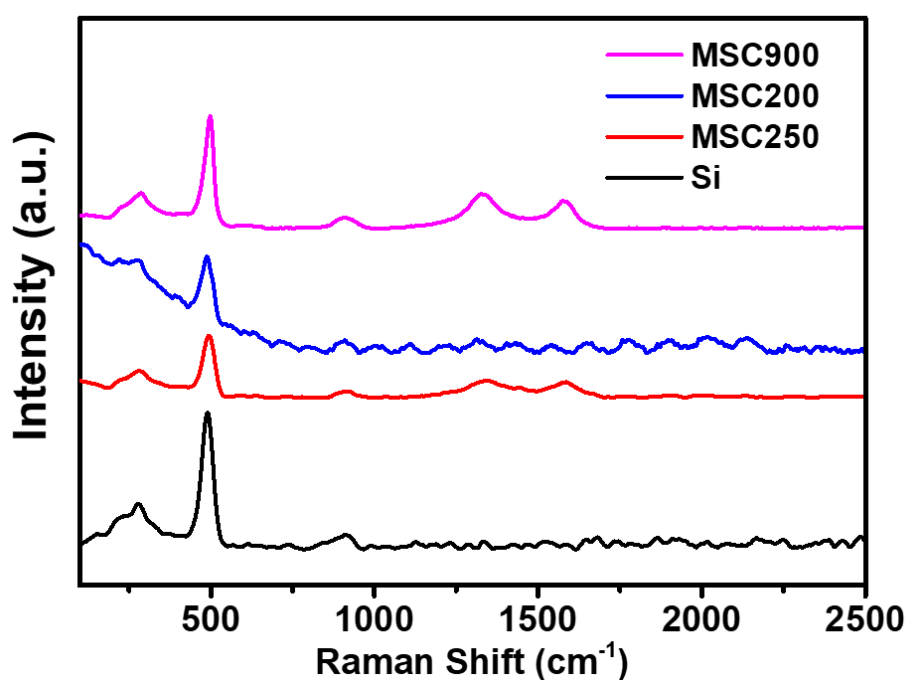


Figure 5.6 Raman spectra of Si NPs, MSC250, MSC200, and MSC900.

Table 5.1 BET surface areas and BJH pore volumes of Si NPs, MSC250, and MSC900.

	BET surface area	BJH pore volume
Si NPs	76.7 m ² g ⁻¹	0.28 cm ³ g ⁻¹
MSC250	202 m ² g ⁻¹	0.55 cm ³ g ⁻¹
MSC900	456m ² g ⁻¹	0.75 cm ³ g ⁻¹

Nitrogen isotherm adsorption/desorption data of MSC250 indicate a BET surface area of

over $200 \text{ m}^2 \text{ g}^{-1}$. Both mesopores and macropores exist with an average size around 50 nm (Figure 5.7). These pores can act as a buffer to prevent damage to the MSC250 structure from Si volume change over cycling, effectively relieving the breathing effect of Si electrode. MSC900 and Si NPs are measured as well, and their nitrogen isotherm curves and pore-size distribution results are provided in Figure 5.7. BET surface areas and Barrett-Joyner-Halenda (BJH) pore volumes of Si NP, MSC250, and MSC900 are summarized in Table 5.1. Si NPs contain few micro/mesopores. Increases in both BET surface area and BJH pore volume can be observed with MSC250 over Si NP. MSC900 has the highest specific surface area and pore volume amongst the three, which can be ascribed to the high surface areas of carbon materials, and more voids from the total removal of polymer.

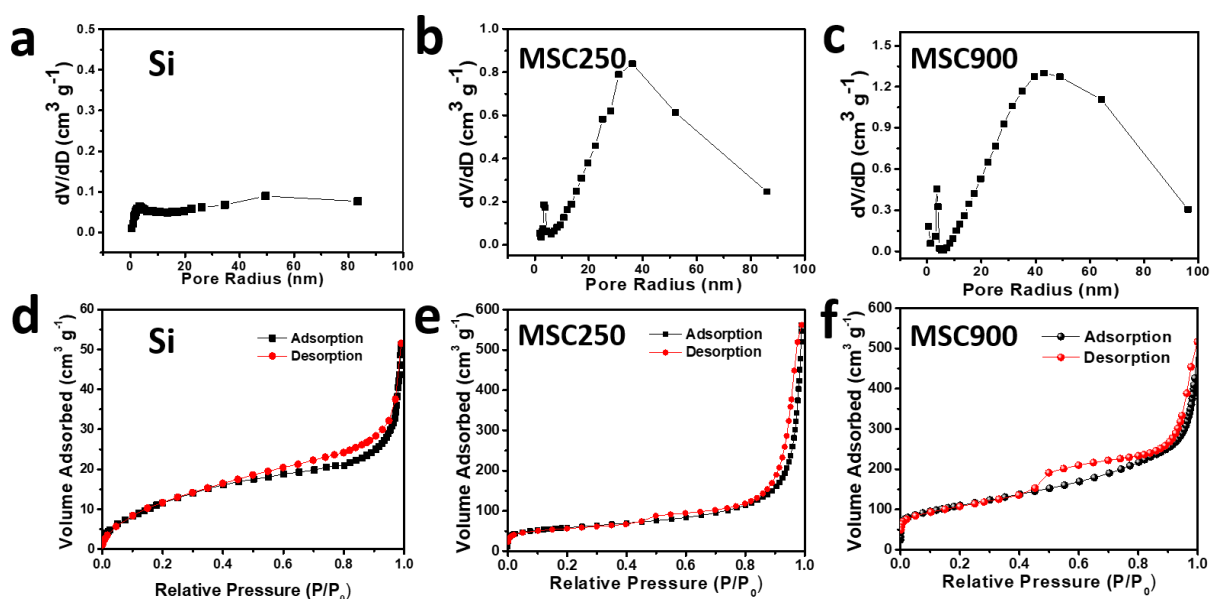


Figure 5.7 Nitrogen isotherm adsorption/desorption curves and pore size distribution graphs of Si NP (a, d), MSC250 (b, e), and MSC900 (c, f).

MSC250 and MSC900 samples were surveyed with X-ray photoelectron spectroscopy (XPS) to study the binding energies of C and Si element. Figure 5.8 a and b are XPS spectra

of C and Si in MSC250; Figure 5.8 c and d are XPS spectra of C and Si in MSC900. The XPS C peak at 289 eV and 287 eV, respectively corresponding to the C=O and C-O functional groups diminish after heat treatment. The covalent bonding between binder and active material, which has been previously identified as a critical factor affecting the electrochemical performance of Si-based electrodes, is retained in MSC250 during the spray-dry process.¹⁴⁶ Another notable difference between Figure 5.8 a and c is that sp^3 C peak significantly decreases. The above changes can be attributed to the breakdown of polymeric chains and loss of sp^3 , which leaves the heat-treated MSC900 no chemical bonding, but physical forces holding together all the components. The apparent increase of SiO₂ peak in Figure 5.8d compared to Figure 5.8b reveals that the ratio of SiO₂ to Si increases after heat treatment. This unfavorable increase of SiO₂ might be due to the oxidation of Si by O element in the polymer binder and can lead to the decrease of capacity of the composite.

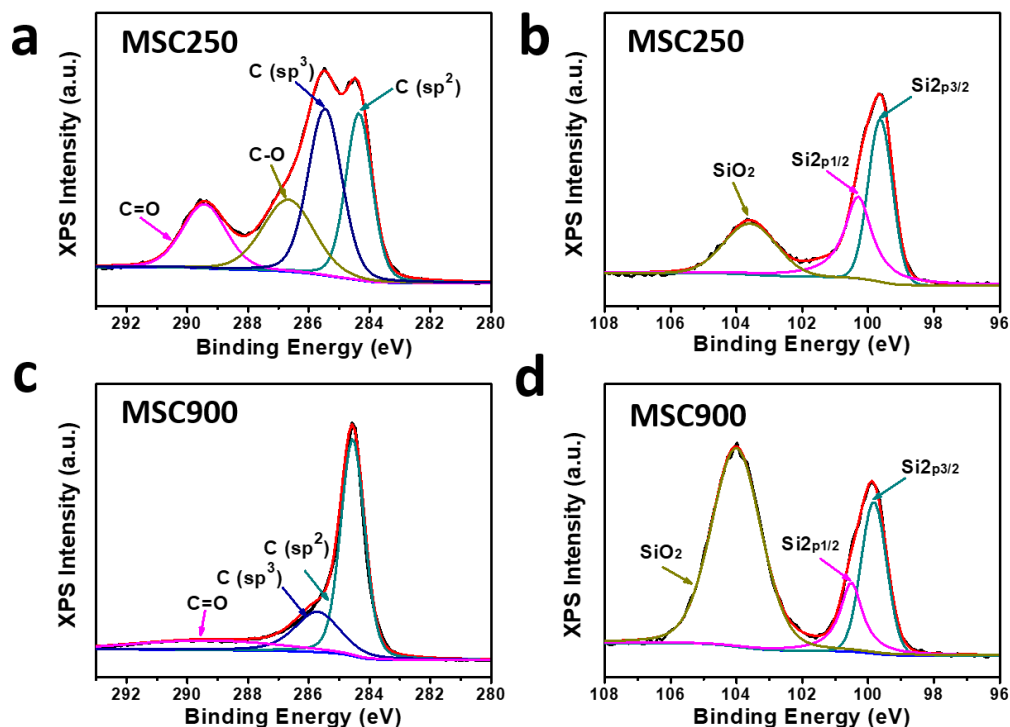


Figure 5.8 XPS spectra of C and Si in MSC250 (a-b) and MSC900 (c-d).

To investigate the electrochemical properties of the MSC250 electrodes, CV and constant current charge/discharge tests were performed. During the initial sweep to 0.01 V in CV (**Figure 5.9**), a broad peak can be observed from 1.15 V, and this is due to the combined effect of irreversible lithiation of functional groups from polymeric binders and the formation of SEI layer.^{147, 148} This broad peak disappears in the subsequent cycles, suggesting the good stability of the formed SEI. The apparent cathodic peaks from 0.27 V can be ascribed to the formation of various Li-Si phases. It is obvious that the peak intensity increases over cycles, which corresponds to the activation process of the electrode.

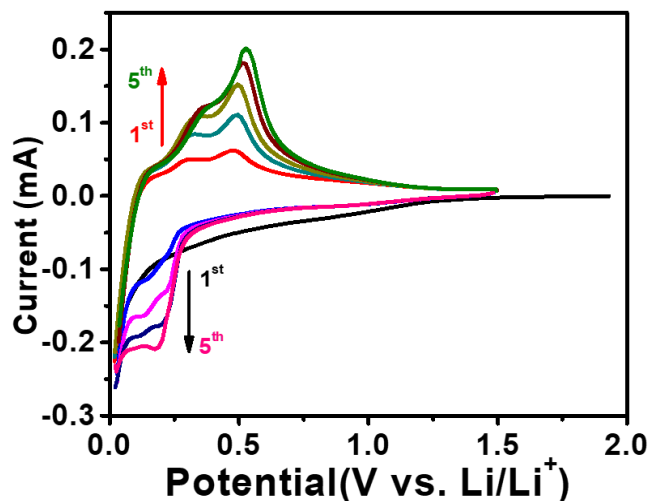


Figure 5.9 CV curves of first five cycles from a MSC250/Li half cell.

This phenomenon can be observed in the charge-discharge curves as well (**Figure 5.10a**), with increased specific capacity in the initial cycles. It is noteworthy that despite the apparent increase in the specific capacity of the electrode, the peak positions maintained mostly unchanged, suggesting the good reversibility of the electrode material.¹³² The initial Coulombic efficiency (CE) of MSC250 was 80.9%, with a first charge capacity of 1555.5 mAh g⁻¹, calculated based on the mass of MSC250. The corresponding irreversible capacity ratio is denoted as Q_{ir} and the value is displayed in each charge/discharge profile figure of different electrodes for better clarification. The areal capacity of this electrode can reach as high as 4 Ah g⁻¹, with electrode mass loading of 2.8 mg cm⁻².

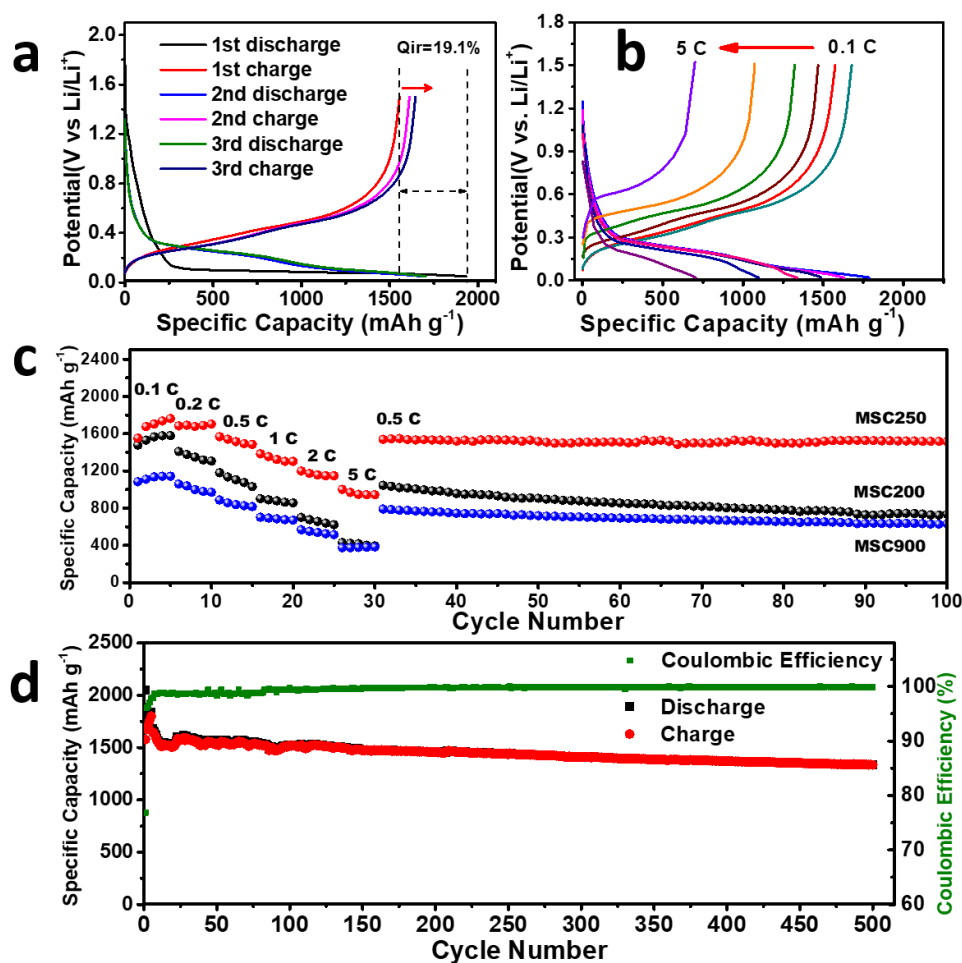


Figure 5.10 a) Charge and discharge profiles of MSC250 cell for the first three cycles. b) Charge and discharge profiles of MSC250 cell at current densities of 0.1 C, 0.2 C, 0.5 C, 1 C, 2 C, and 5 C. c) Comparison of rate capabilities of MSC250 and MSC200 cells. d) Cycling performance at 0.5 C and CE data of MSC250 for 500 cycles.

Compared to MSC200 shown in **Figure 5.11a**, MSC250 electrode shows higher initial CE, which can be due to the cured polymer binder in MSC250, and thus better structural integrity. Higher Si content in MSC250 might have contributed to the slight advantage in specific capacity of MSC250 over MSC200. High-temperature annealed MSC900 shows a lower initial charge capacity of 908 mAh g^{-1} (Figure 5.11b), probably due to the increased SiO_2 content on the surface of Si. The initial CE is 71.1%, lower than that of both MSC250 and MSC200, which

can result from the much higher surface area in the composite, as shown in Table 5.1.

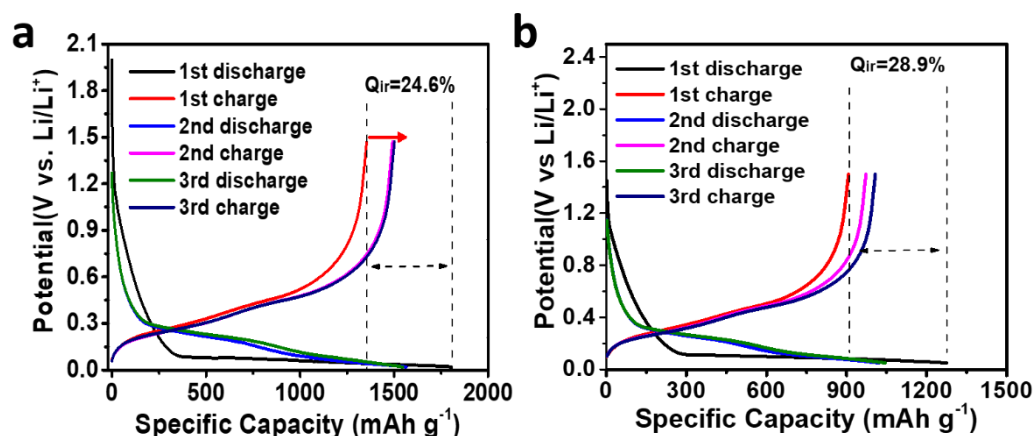


Figure 5.11 First three cycles charge-discharge curves of a) MSC200, and b) MSC900.

To evaluate the electrode performance of MSC250 at multiple rates, the current densities were ramped from 0.1 C to 5 C in 5 charge and discharge cycle increments before undergoing stability testing at a constant 0.5 C, as displayed in Figure 5.10b. Despite some decrease in capacity with increasing rates, the charge and discharge profiles resemble each other at different rates. The plateau positions are consistent except the ones at 5 C, which indicates minor polarization at rates up to 2 C, and thus good rate capability of the electrode. Cycling performances of MSC250, MSC200 and MSC900 under multiple rates are displayed in Figure 5.10c. MSC250 and MSC200 electrodes show similar initial charge capacity, and both electrodes show no sign of degradation in the first 5 cycles at 0.1 C. However, the MSC200 electrode steadily loses its capacity with the increase of current densities, reflecting the significant effect of resistance of the electrode material. MSC250 electrode retains 1715, 1506, 1305, 1166, 957 mAh g⁻¹ at each rate from 0.2 C to 5 C. It is noteworthy to mention that the electrode is stabilized with a charge capacity of ~1500 mAh g⁻¹ when the current was restored to 0.5 C. MSC900 only exhibits around half the capacity of MSC250 at various rates, despite

relatively better stability than the MSC200 control. This outstanding rate performance and stable cycling thereafter of MSC250 electrode suggest it not only has efficient electron conduction and fast ion transport, but also shows great electrode structure stability under multi-rate test and long-term cycling. In addition to the rate performance test, another two cells were cycled at 0.5 C, and 1 C for 500 cycles. MSC250 electrode delivers excellent cycling stability with 13% loss over 500 cycles at a rate of 0.5 C (Figure 5.10d). At 1 C, the MSC250 cell retains 62% of its initial capacity after 500 cycles (**Figure 5.12**).

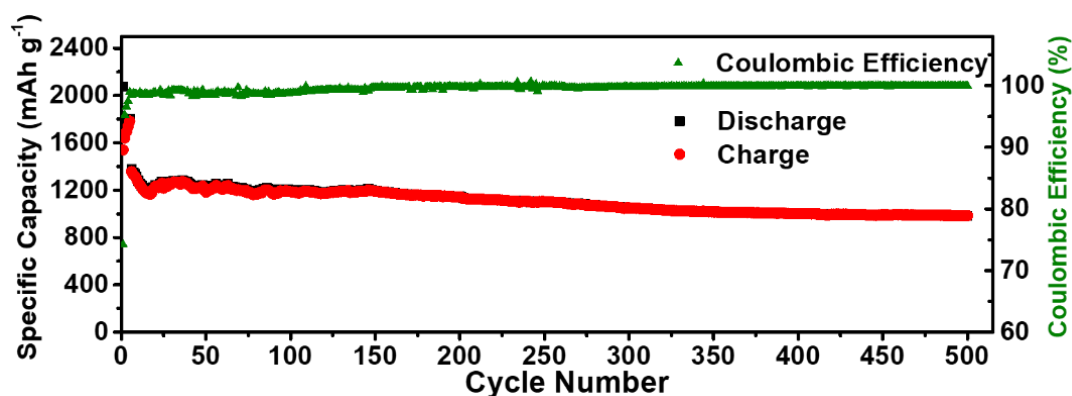


Figure 5.12 Long-term cycling test of MSC250 at 1C, with CE plot.

The CE stabilizes at above 99.8% after initial cycles of activation process for both cells, indicating the high reversibility of lithiation-delithiation process in the electrodes. Cycling performances of MSC200 and MSC900 at 0.5 C are displayed in **Figure 5.13a** and **b**, respectively. MSC200 electrode experiences sharp capacity decay when the rate is switched to 0.5 C after 5 cycles at 0.1 A g⁻¹. Only 60% capacity is retained after 200 cycles. MSC900 shows slightly better capacity retention (67%) over MSC200, however, the final capacity of MSC900 is relatively lower due to its low initial capacity.

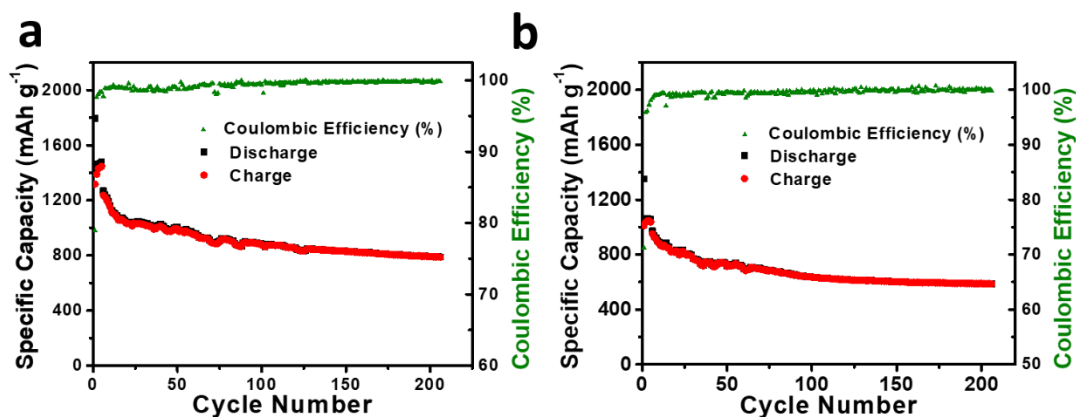


Figure 5.13 Cycling performance of MSC200 and MSC900 at 0.5 C for 200 cycles, with CE plots.

The superior electrochemical performance and structural integrity of the MSC250 electrodes are mainly ascribed to the following characteristics. First, the primary nano-sized Si acting as active material can undergo the volume change over charge and discharge without pulverization. Meanwhile, nano-sized Si reduces the Li diffusion length inside Si and ensures good rate capability of the electrode. Second, the in situ formed carbon-binder cage not only acts as a stable host for Si NPs, but also provides an interconnected conductive network for excellent electronic conductivity. Third, the abundant voids inside MSC250 could effectively accommodate the volume change of Si and help maintain the overall structural integrity of the composite. In addition, micron-size secondary MSC250 particles and their near-normalized size distribution are advantageous over nano-sized materials in terms of packing density and structural stability.

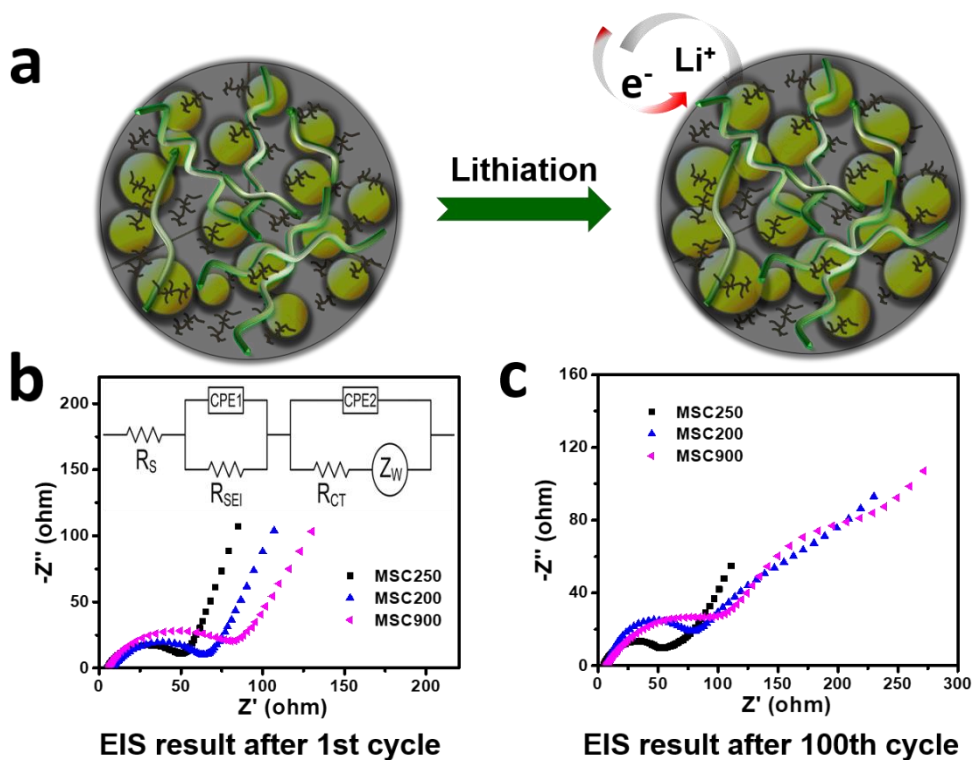


Figure 5.14 a) A plausible illustration of lithiation process of a MSC250 sphere. EIS spectra of MSC250, MSC200, and MSC900 electrodes, b) after first 1st charge, and c) after 100th charge.

The charge mechanism of the MSC250 composite is demonstrated in **Figure 5.14a**. Primary Si NPs undergo significant volume change over lithiation, while the empty space inside the composite accommodates most of the volume change and size of the sphere remains nearly unchanged. It is rational to conclude that the crosslinked and cured PAA/CMC binder and carbon nanotubes fasten the components inside the composite, maintaining the integrity of the structure. Li ions can easily diffuse to Si NPs as there are no concrete barriers blocking the Li-ion diffusion. Electron conduction is facilitated by the conductive network formed with CNTs and KB. Coin cells of MSC250 composite, reference samples MSC200 and MSC900 were tested with a potentiostatic electrochemical impedance spectroscopy (EIS) program after

the first cycle and the 100th cycle. Nyquist plots of MSC250, and reference samples, after 1st cycle, and after 100th cycles are shown in Figure 5.14b and c, with the equivalent circuit insert in Figure 5.14b. The charge transfer resistance of MSC250 is not only the least among the three, but also remains nearly unchanged over cycling, proving the good stability of the electrode and electrode/electrolyte interphase. Morphology of cycled MSC250 sphere is examined by both SEM and TEM as shown in **Figure 5.15a** and b. The spherical shape is retained, although the roughness of the surface is reduced after contact with electrolyte. Elemental mapping confirms the even distribution of the initial elements in the composite, and existence of fluorine from electrolyte.

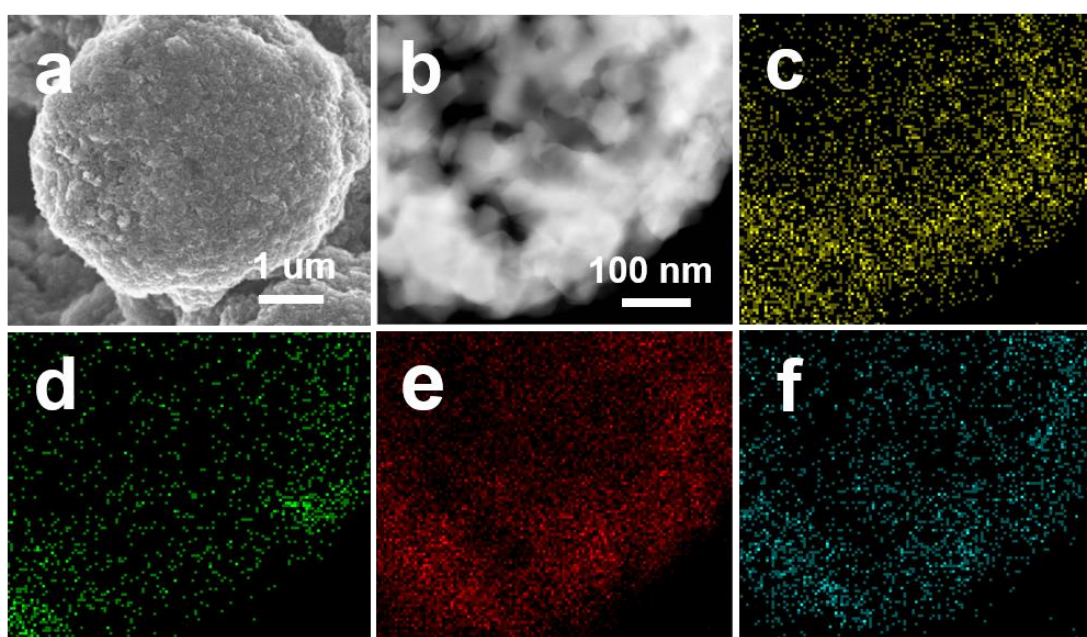


Figure 5.15 SEM, STEM images, and elemental mapping graphs of C, O, Si and F of a MSC250 particle after 100 cycles.

A full-cell LIB with MSC250 as anode and commercial $\text{LiNi}_{1/3}\text{Co}_{1/3}\text{Mn}_{1/3}\text{O}_2$ (NMC) as cathode was fabricated to study the electrochemical properties of a MSC250 full cell. The

commercial NMC electrode was first tested in a half cell using Li as counter electrode to obtain the capacity of the electrode. The charge/discharge voltage range was set to be 3.0 V to 4.3 V. As shown in **Figure 5.16a**, the specific capacity of the electrode is measured to be 163 mAh g⁻¹, which corresponds to an areal capacity of 3067 mAh cm⁻². The average voltage of the discharge plateau is ~3.8 V. This NMC cathode was coupled with a commercial graphite electrode, and a full-cell graphite/NMC LIB was fabricated. All the energy densities are calculated based on electrode area, and all electrodes are single-side coated. The graphite/NMC cell presents an areal energy density of 10 mWh cm⁻², with an average voltage of the discharge plateau at ~3.65 V (Figure 5.16b). The MSC250/NMC full-cell charge/discharge profiles are displayed in Figure 5.16c, and the areal energy density of the cell is 9.8 mWh cm⁻², with an average discharge plateau at ~3.5 V. For all the full-cell LIBs prepared here, the anode capacity is deliberately maintained slightly higher than that of the cathode. Comparing the MSC250/NMC and graphite/NMC cells, the graphite/NMC cell has a narrow advantage in areal energy capacity. This is mostly due to the slightly higher voltage plateau of the graphite/NMC cell. However, when taking the electrode thickness into consideration, the advantages of MSC250 cell are revealed. The thickness of the MSC250 electrode with an areal loading of 2.8 mg is measured to be 32 μm, while that of graphite electrode with an areal loading of 10.7 mg is measured to be 97 μm, three times that of the MSC250 electrode. This reduction of electrode thickness can significantly contribute to the increase of volumetric energy density of an actual LIB with multiple stacks of electrodes, in terms of both volume and weight. The commercial NMC with single-sided coating and mass loading of 19.8 mg cm⁻² has the thickness of 114 μm, while double-sided NMC cathode is 212 μm thick. Revisiting previous

reports with estimates of cell energy densities^{149, 150}, we have calculated the approximate energy densities of cells based on MSC250 anode and commercial graphite anode, respectively. In a hypothetical multi-stack MSC250/NMC full cell (stack number > 10) with both electrodes double-sided, the thickness of the MSC250 anode is 52 μm , thickness of the separator (Celgard 2500) is around 25 μm , and the total thickness of each stack is 289 μm , corresponding to 664 Wh L^{-1} , among the highest values in Li-ion technology. Using the same calculation method, a single stack in a hypothetical graphite/NMC cell is 419 μm in thickness, which can be translated to 477 Wh L^{-1} . A 39% advantage in volumetric energy density over battery with commercial electrodes is obtained with MSC250/NMC-based cell. As shown in Figure 5.16d, This MSC250/NMC full cell retains 88% of its initial capacity after 100 cycles at a charge and discharge rate of 0.1 C, and the CE slowly approaches 100% with the increase of cycle number.

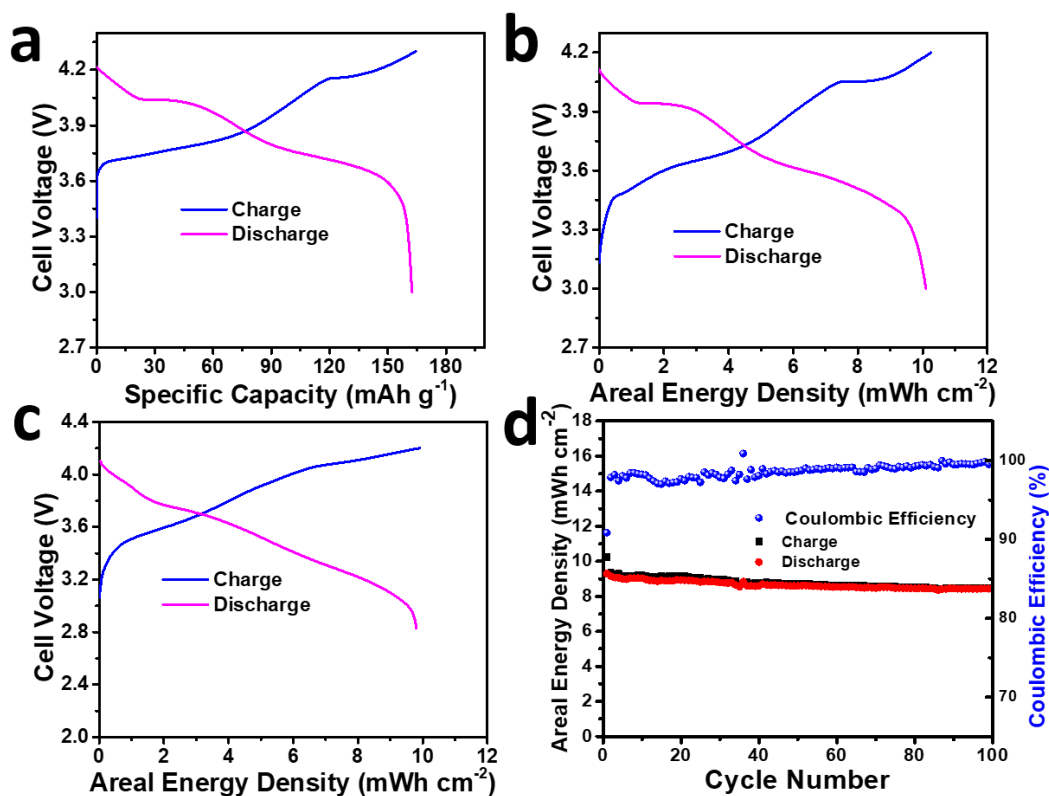


Figure 5.16 a) Charge and discharge profiles of Li/NMC cell, with specific capacity as X-axis. b) Charge and discharge profiles of graphite/NMC cell, with areal energy density as X-axis. c) Charge and discharge profiles of MSC250/NMC cell, with areal energy density as X-axis. d) Cycling performance of MSC250/NMC full cell for 100 cycles at 0.1 C.

Charge and discharge profiles of the cell under multiple rates are shown in **Figure 5.17**. A series of currents from 0.1 C to 1 C were used, and an areal energy density of 6.6 mWh cm^{-2} was retained at 1 C. The good retention of energy density and charge and discharge profiles at high rates indicates the excellent ion transport and electron conduction in the cell. There is a $\sim 0.2 \text{ V}$ gap between the discharge profiles at 0.1 C and 1 C. This might be explained by the intrinsic resistance inside the cell that causes the IR drop and voltage difference.

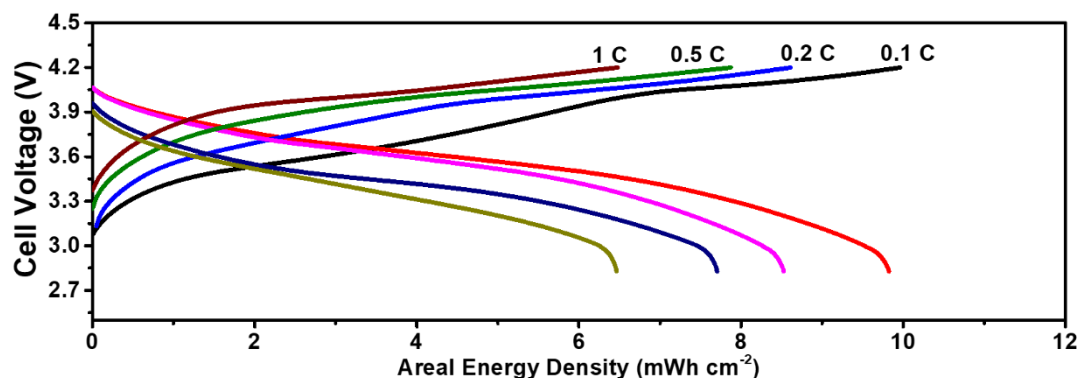


Figure 5.17 Charge/discharge curves of MSC250/NMC cell at current densities from 0.1 C to 1 C.

5.4 Summary

To summarize, we have synthesized a secondary micron-sized sphere, with Si embedded in a matrix formed by crosslinked polymer binders and conductive carbons. With deliberate temperature control according to the thermal properties of polymers, a stable structure is obtained, with crosslinked polymer chains providing the excellent robustness. Voids inside the structure provide necessary buffer room for Si volume change and further contribute to the long-term structural integrity of the secondary sphere. Construction of the micron-sized particle and the good size distribution largely improve the tap density and thus volumetric electrode density. MSC250 anode with $\frac{1}{4}$ the mass or $\frac{1}{3}$ the volume of commercial graphite electrode provides the same capacity, significantly improving volumetric energy densities of LIBs. MSC250 successfully utilizes the advantages of nano-sized Si, while effectively circumventing the associated drawbacks, such as low tap density and discontinuous electric contact. Considering the rational design, facile synthesis, and much enhanced electrochemical

performance, MSC250 can be an exemplary model for the practical implementation of nano Si in commercial LIBs.

6. Engineering a Core-shell Structure with Si Core and Amorphous C-TiO_x as Shell and Support Matrix

6.1 Introduction

Towards the same goal, the following project is targeted to produce a secondary Si agglomerate with a C-TiO_x matrix. This Si material can be seen as the final Si iteration developed with the knowledge gained throughout this thesis. It employs a wet chemistry technique in which the morphology and composition of material is controllable. In addition to the secondary support structure that embeds Si in a larger conductive network, the intimate C-TiO_x coating can serve to protect the Si from continuous SEI formation in a matter superior to the previous two projects.

Titanium-based materials have been proposed as a group of benign and safe electrode materials in the application of LIBs due to the non-toxic nature of titanium element.^{151, 152} TiO₂ have been reported as both an electrode material and coating/stuffing/skeleton material in Si-based composites.^{153, 154} TiO₂ experiences less drastic volume change than Si during lithiation/delithiation process. Other than that, the charge and discharge plateau of TiO₂ (above 1.5 V vs. Li/Li⁺) is much higher than that of Si.¹⁵⁵ One can easily tune the charge and discharge window of a battery with TiO₂/Si anode so that TiO₂ remains at lithiated state over cycling, without repetitive lithiation of TiO₂. TiO₂ is more thermally stable when compared to its carbon counterparts, and thus improves safety of batteries in the case of a thermal runaway.¹⁵⁶ Many types of TiO₂/Si hybrids have been developed via different synthetic routes. There are generally two approaches of combining Si and TiO₂. One is to have TiO₂ coating on Si structures, and

the other one is to employ TiO_2 as template for Si deposition/growth.^{157, 158} Nanostructures that have been reported in both approaches include nanowires, nanotubes, nanoparticles.^{98, 159} Despite the benefits of TiO_2 , one must note that TiO_2 has a low electronic conductivity ($<10^{-4} \text{ S cm}^{-1}$), which has been used as an insulator at room temperature.¹⁶⁰

To fully harvest the benefits of compositing Si with TiO_2 , a carbon-coated TiO_x matrix with Si NPs embedded inside is prepared via a facile synthetic strategy, which not only circumvents the disadvantages of both, but also organically utilizes the advantages of nano-sized Si. Si NPs are firstly coated with a layer of TiO_2 and meanwhile form micron-sized clusters. To enhance the electronic conductivity and improve the mechanical robustness of the TiO_2 coating layer, the preliminary composite is subsequently annealed at an elevated temperature in a reducing atmosphere to partially reduce the TiO_2 to TiO_x where x is between 0-2. In the same annealing step, a carbon-containing precursor gas is introduced at the end, which decomposes and forms a thin carbon coating layer on TiO_x/Si clusters, after which the C- TiO_x/Si composite is obtained. This C- TiO_x/Si composite not only bears the benefits of Si NPs, such as good volume change adaption, shortened Li-ion diffusion and electron conduction paths, but also decreases the specific surface area and improves the tap density of Si. Tap density of the new composite is over four time that of Si NPs. Deliberately tailored and hydrogenated TiO_x matrix can act as a protective coating on Si, avoiding excessive SEI formation, and a buffer matrix that holds together Si NPs and absorb volume change of Si from lithiation/delithiation process. Another carbon coating layer further enhances the conductivity of the composite and ensures sufficient effective contact points between the cluster and conductive network in electrode. Overall, this cluster composite not only provides a matrix that encapsulates Si NPs, but also has excellent

electrical conductivity that facilitates fast electrochemical reaction in the electrode. The protective TiO_x coating layer, as well as the reduced specific surface area can contribute to a more stable SEI that ensures long-term reversible Li storage. Moreover, the formation of micron-sized secondary cluster effectively increases the tap density of the composite over Si NPs, offsetting the drawback from nanonization, and paving way for practical application of Si anodes.

6.2 Experimental Methods

6.2.1 Material Synthesis:

In a typical synthesis process, 400 mg of Si NPs (NanoAmor, $\phi \sim 70$ nm) and 120 ml of anhydrous ethanol were sonicated in a round-bottom flask for 2 hr for Si NPs to disperse in ethanol. After that, 800 μL of titanium n-butoxide (TBOT) (Sigma Aldrich) was added into the flask and stirred for 30 min, followed by dropwise addition of 800 μL distilled deionized water (DDI) over 15 min period. The mixture was refluxed and stirred at 90 $^\circ\text{C}$ in an oil bath for 6 hr before it was removed from the set-up and naturally cooled down. The sample was washed, dried and weighed. The intermediate TiO_2/Si product of around 600 mg can be obtained from each batch. TiO_2/Si was subsequently placed in a tube furnace for the final formation step of TiO_x and carbon coating. Temperature of the furnace was first elevated to 800 $^\circ\text{C}$ and maintained for 2 hr for TiO_2 phase stabilization in an argon atmosphere. Ten percent H_2 in Ar was subsequently passed through the quartz tube to hydrogenate TiO_2 and create oxygen deficiencies in TiO_2 . Finally, toluene vapor was introduced to the system for a short period of time (15 min) for the deposition of carbon. Si/C composite without the inclusion of TiO_x matrix was prepared according to the same procedure of C- TiO_x/Si , except for the addition of TBOT.

C-TiO₂/Si was prepared following the same synthetic routes of C-TiO_x/Si, except for the H₂ introduction during annealing.

6.2.2 *Physical Characterization:*

Morphologies of the samples were obtained from scanning electron microscope (SEM, Zeiss Ultra Plus field emission microscope), and transmission electron microscope (TEM, JEOL 2010F TEM/STEM field emission microscope) featured with high-resolution capability and equipped with an energy-dispersive X-ray spectroscopy (EDX). X-ray diffraction (XRD) patterns were obtained from an Inel XRG 3000 diffractometer (monochromatic Cu K- α X-rays, 0.154 nm). X-ray photoelectron spectroscopy (XPS, Thermo Scientific K-Alpha) was conducted to measure the surface properties of samples and oxidation states of the elements. Thermal gravimetric analysis was carried out in air atmosphere. The nitrogen adsorption isotherms were obtained from a surface area and porosimetry system (Micromeritics ASAP 2020 Plus), with over 3 hr degassing at a temperature of 250 °C.

6.2.3 *Electrochemical Measurements:*

The composition of all working electrodes in this research was as follows: 80% active material, 10% Super-P conductive carbon, and 10% sodium carboxymethyl cellulose binder (In 2% water solution). Height between the casting doctor blade and copper foil was maintained at 120 μ m for all electrodes. Same pressure of 200 pounds per cm² was applied to press all electrodes. Working electrodes were paired with Li counter electrodes and made into CR2032-type coin cells for all electrochemical measurements. All battery-assembly parts and materials were thoroughly dried before being transferred into an argon-filled glovebox (Labstar 10,

Mbraun) for cell assembly. Only one type of electrolyte was used in this research, and the composition was 1 M LiPF_6 in a solution mixture of ethylene carbonate (EC), dimethyl carbonate (DMC), and fluoroethylene carbonate (FEC) (45:45:10, by volume, BASF). Separator placed in between cathode and anode was a polypropylene membrane from Celgard (PP2500, high porosity, 25 μm microporous). Galvanostatic charge/discharge tests were performed on battery testers from Neware, with voltage range from 0.05-1.5 V. Rate capability and long-term cycling stability of each material were obtained from the charge/discharge tests. Potentiostatic electrochemical impedance spectroscopy (EIS) data were collected on an electrochemical workstation (Versa Stat MC, Princeton Applied Research). EIS was conducted in the frequency range of 1 M-0.1 Hz, with a perturbation voltage amplitude of 10 mV.

6.3 Results and Discussions

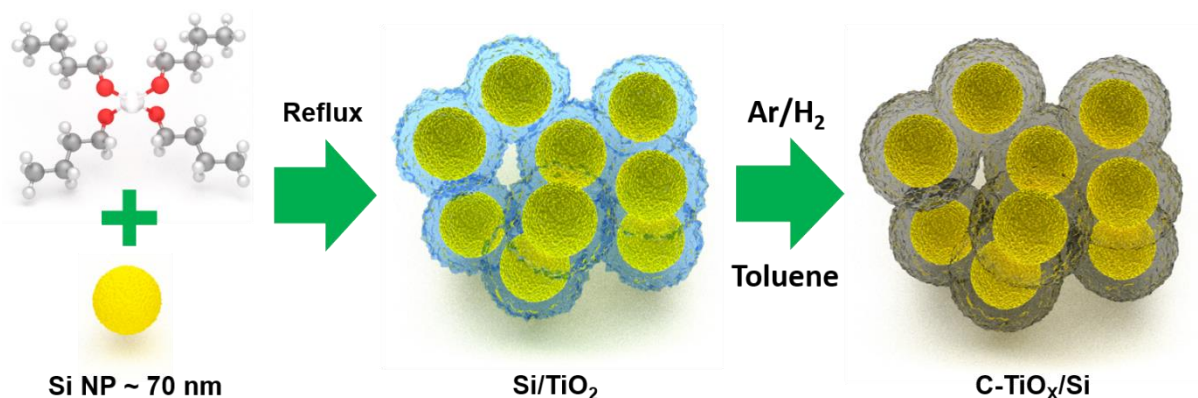


Figure 6.1 Schematic illustration of synthetic procedure of C-TiO_x/Si.

A carbon-coated TiO_x matrix with Si NPs embedded inside is prepared by a two-step synthesis process as illustrated in **Figure 6.1**. A homogenous TiO₂ coating is first achieved via hydrolysis of a Ti precursor under reflux. The intermediate product is later placed in a tube furnace for the subsequent phase stabilization, oxygen deficiency creation, and carbon coating.

Details of a typical synthesis are described in the Material Synthesis section. The micron-sized secondary cluster composite is obtained and denoted as C-TiO_x/Si. Discrete Si NPs agglomerate into micron-sized clusters after the synthesis (**Figure 6.2** a and b). As shown in Figure 6.2c, Si NPs are firmly attached to the secondary cluster by the homogeneous C-TiO_x coating layer. Figure 6.2 d is a TEM image of the edge of a C-TiO_x/Si particle, with focus on the bulge of a single Si NP. Elemental mappings of the highlighted area are displayed in Figure 6.2 e-h, representing elements of C, O, Si, and Ti respectively. It is interesting to note that Si is universally covered by C and titanium oxide layers. Si and Ti elemental mappings display a clear contrast, highlighting the shape of the Si core and the TiO_x shell.

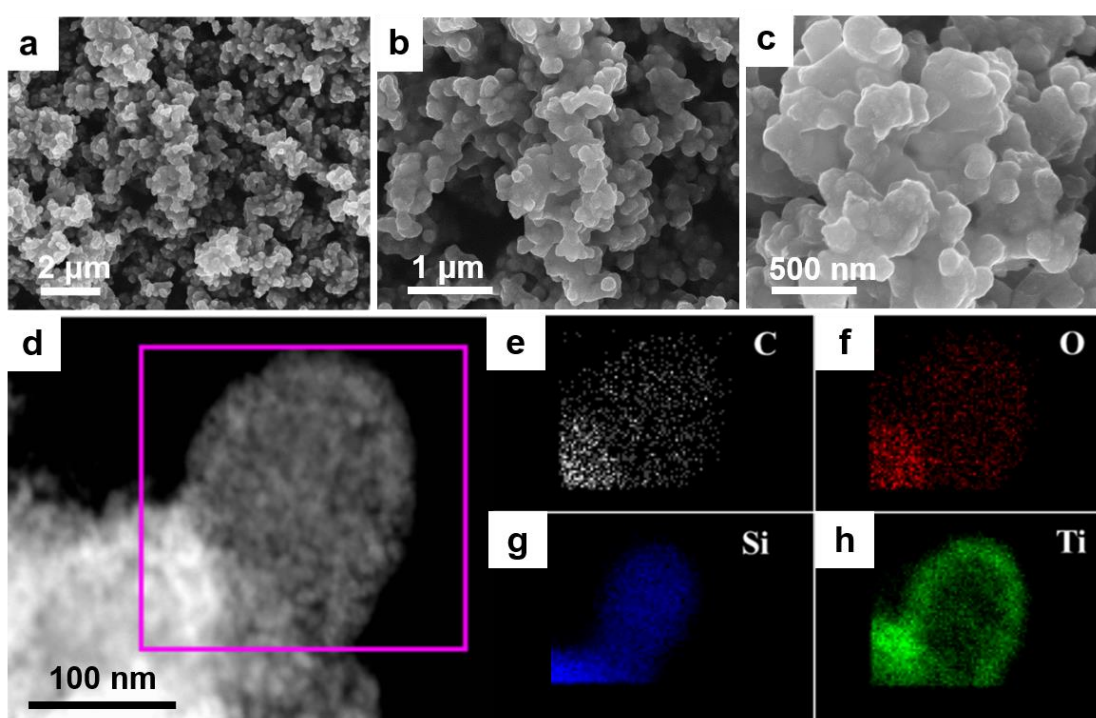


Figure 6.2 a-c) C-TiO_x/Si cluster at magnifications of 20,000X, 50,000X, and 100,000X, respectively. d) TEM image with focus on a single Si NP on C-TiO_x/Si, e-f) C, O, Si, and Ti elemental mappings of the highlighted area in d).

By tuning the ratio of Ti source to Si during the synthesis, amount of TiO_x and the final thickness of the TiO_x coating can be controlled. As shown in **Figure 6.3**, three thicknesses are obtained when initial titanium n-butoxide (TBOT):Si mass ratios of 4:1, 2:1 and 1:1 are used. With an initial TBOT:Si mass ratio of 4:1, thickness of the TiO_x layer is around 30 nm. Excess TiO_2 can be seen existing as small particles, in addition to coatings on Si (**Figure 6.4**). A moderate C- TiO_x thickness of ~ 20 nm is obtained when the mass ratio of Si and TBOT is 1:2. Only a very thin layer of TiO_2 (~ 5 nm) can be observed when the ratio of TBOT to Si is 1:1. The TiO_x/Si structure is not well integrated, with some Si NPs dissociated beyond the cluster structure (**Figure 6.5**). Reflux reaction condition is also a vital factor to the homogeneous coating of TiO_x layer, as it significantly enhances the dispersion of reactants and promotes uniform coating. SEM images of a TiO_x/Si sample prepared under the same condition except for the missing of reflux show that significant amount of TiO_x tends to form particles (**Figure 6.6**), instead of uniformly coating on Si NPs.

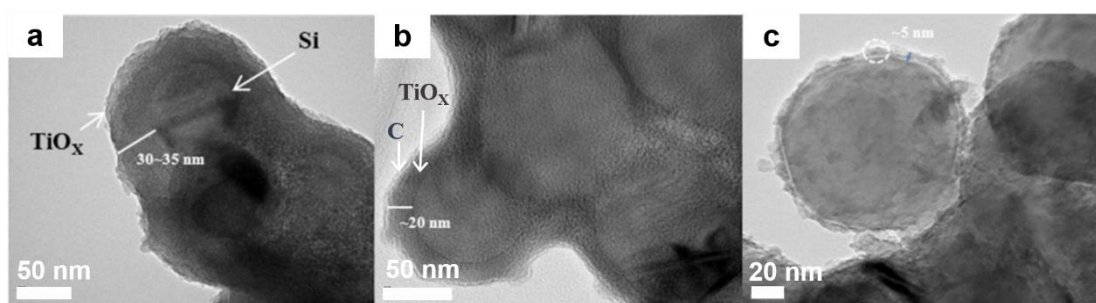


Figure 6.3 a-c) TEM images TiO_x/Si composites synthesized with initial TBOT:Si mass ratios of 4:1, 2:1, and 1:1, respectively.

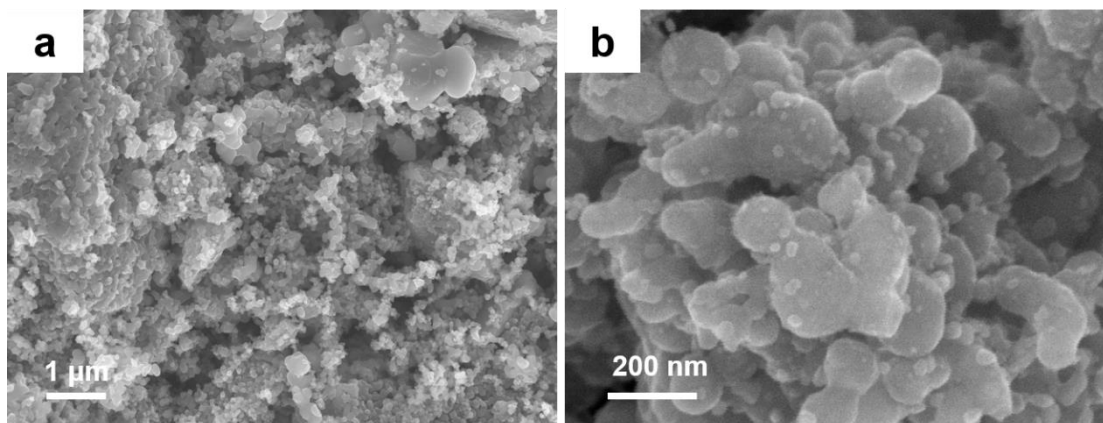


Figure 6.4 SEM images of TiO_x/Si with initial TBOT:Si mass ratio of 4:1.

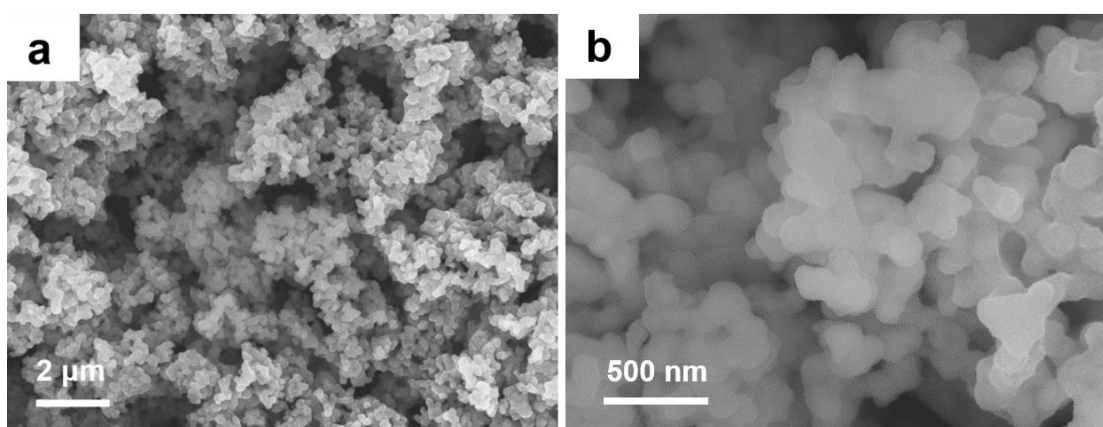


Figure 6.5 SEM images of TiO_x/Si with initial TBOT:Si mass ratio of 1:1.

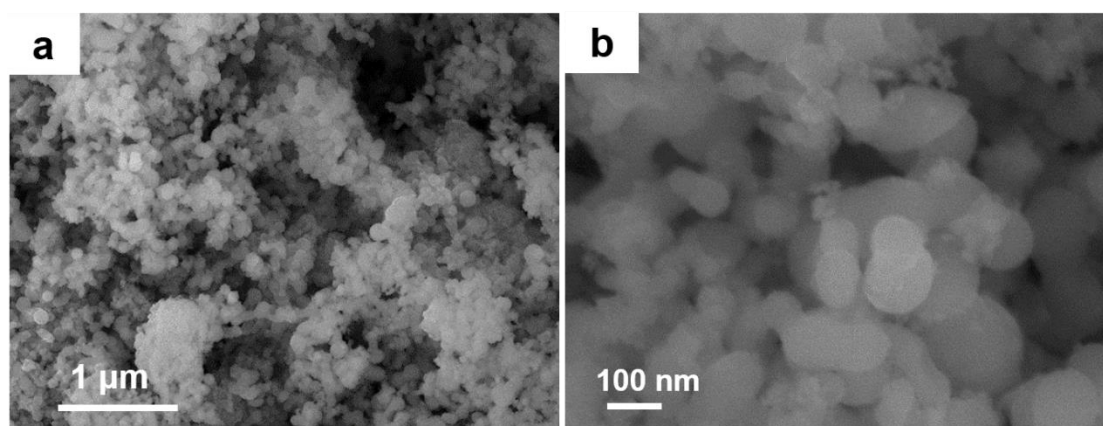


Figure 6.6 SEM images of TiO_x/Si with initial TBOT:Si mass ratio of 2:1, without reflux.

XRD experiments were conducted to investigate the crystallinity changes during different stages of the synthesis. As shown in **Figure 6.7a**, distinct Si peaks can be observed with pure Si NPs. After the first TiO₂ coating process, anatase TiO₂ phase appears in the diffraction pattern, in addition to the original Si peaks (**Figure 6.8**). After heat treatment at 800 °C, it is apparent that Si maintains its crystalline phase, while the crystallinity of TiO₂ is decreased, as indicated by the shorter and broader [101] peak at 25.6 °. After the carbon coating process, no distinct carbon peaks are generated, indicating the amorphous nature of the carbon coating layer. Without hydrogen treatment, the anatase phase of TiO₂ remains after the carbon coating process. In contrast, the anatase peaks of TiO₂ disappear in C-TiO_x/Si after hydrogen treatment, revealing the significant decrease in crystallinity, consistent with previous studies with TiO₂.¹⁶¹

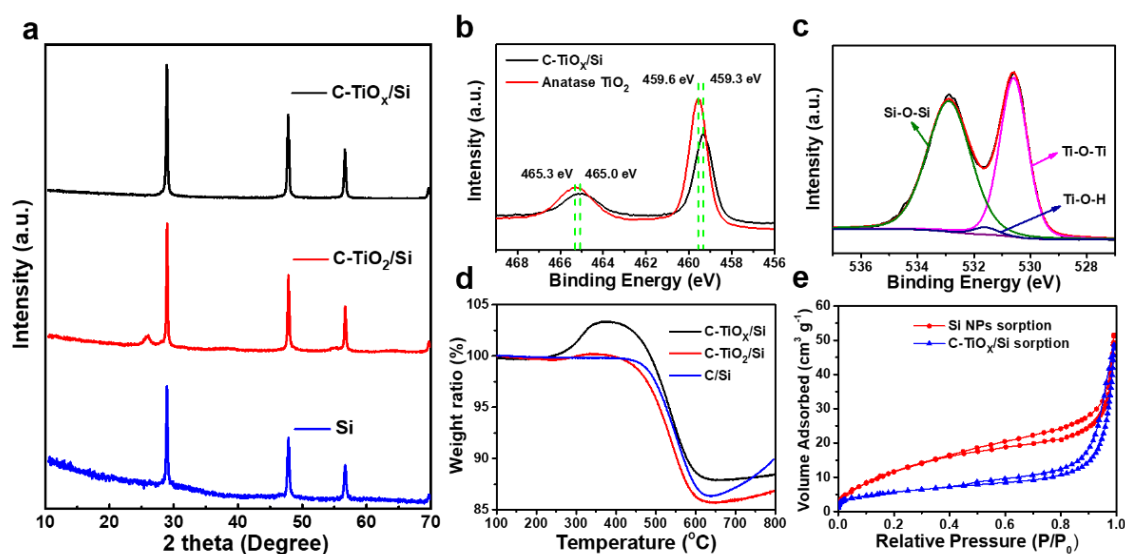


Figure 6.7 a) XRD patterns of Si, C-TiO₂/Si, and C-TiO_x/Si, b) Ti 2p high-resolution XPS spectra of C-TiO_x/Si and anatase TiO₂, c) O 1s high-resolution XPS spectrum of C-TiO_x/Si, d) TGA graphs of C/Si, C-TiO₂/Si, and C-TiO_x/Si, e) nitrogen sorption isotherms of Si and C-TiO_x/Si.

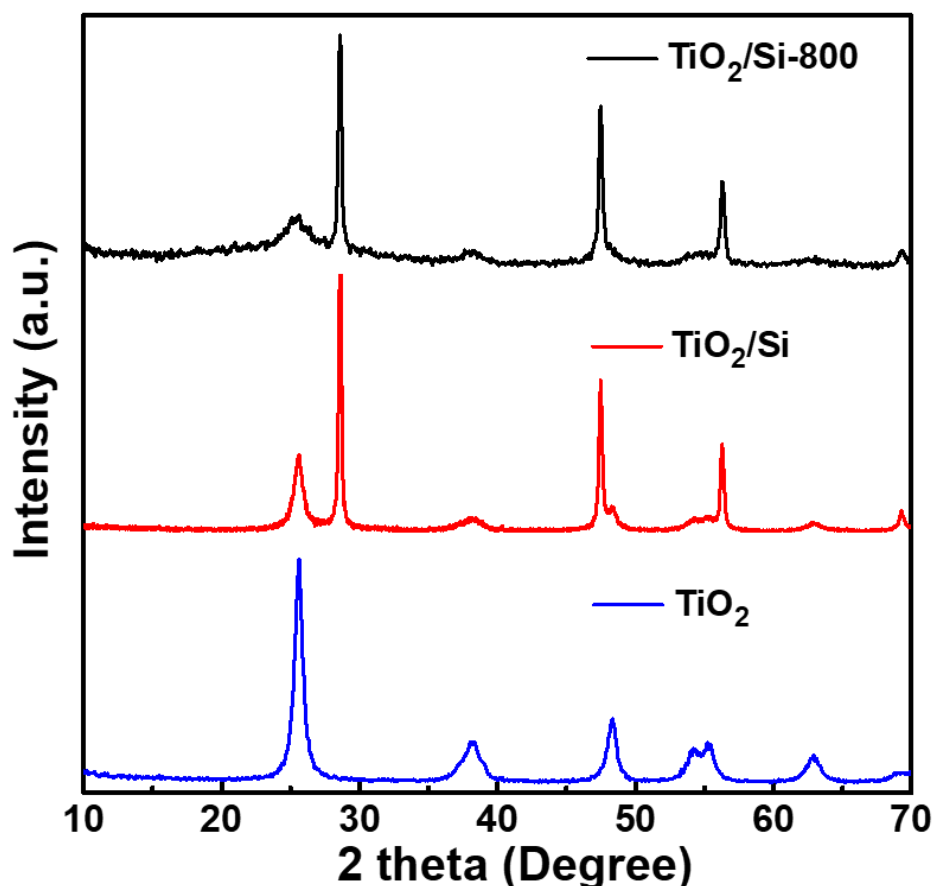


Figure 6.8 XRD patterns of anatase TiO_2 , TiO_2/Si , and TiO_x/Si after heat treatment at 800 °C.

XPS is carried out to further study the effect of hydrogen treatment on the properties of titanium oxide layer. As shown in Figure 6.7b, a brief shift (-0.3 eV) in the binding energies of Ti $2p_{1/2}$ and Ti $2p_{3/2}$ peaks in C- TiO_x/Si compared to the pristine anatase TiO_2 confirms the partial reduction of Ti^{4+} and creation of oxygen vacancies in the titanium oxide layer.¹⁶² A higher density of charge carriers can be achieved as a result of the generation of oxygen vacancies, which can be translated to the enhanced electron conductivity of the synthesized material.¹⁶³ In the O 1s XPS spectra displayed in Figure 6.7c, characteristic Ti-O-Ti XPS peak of O 1s spectra can be clearly identified at ~530.5 eV. A broad peak centering at 531.6 eV can be attributed to the Ti-O-H bond created by the hydrogenation.¹⁶⁴ The existence of SiO_2 is also revealed by the Si-O-Si peak at ~532.9 eV.

TGA is conducted in air with C-TiO_x/Si, C-TiO₂/Si, and C/Si samples. Contents of carbon can be readily observed to be in the range of 13-16% among the three samples (Figure 6.7d), which indicates the good reproducibility of carbon coating with same reaction condition applied. It is noteworthy to mention the weight increase of C-TiO_x/Si sample which commences at around 250 °C. This phenomenon can be ascribed to the saturation of oxygen in TiO_x and formation of TiO₂. TiO_x synthesized via an identical hydrogenation process displays a similar weight increase pattern over the same temperature range in TGA profile (**Figure 6.9**) with C-TiO_x/Si.

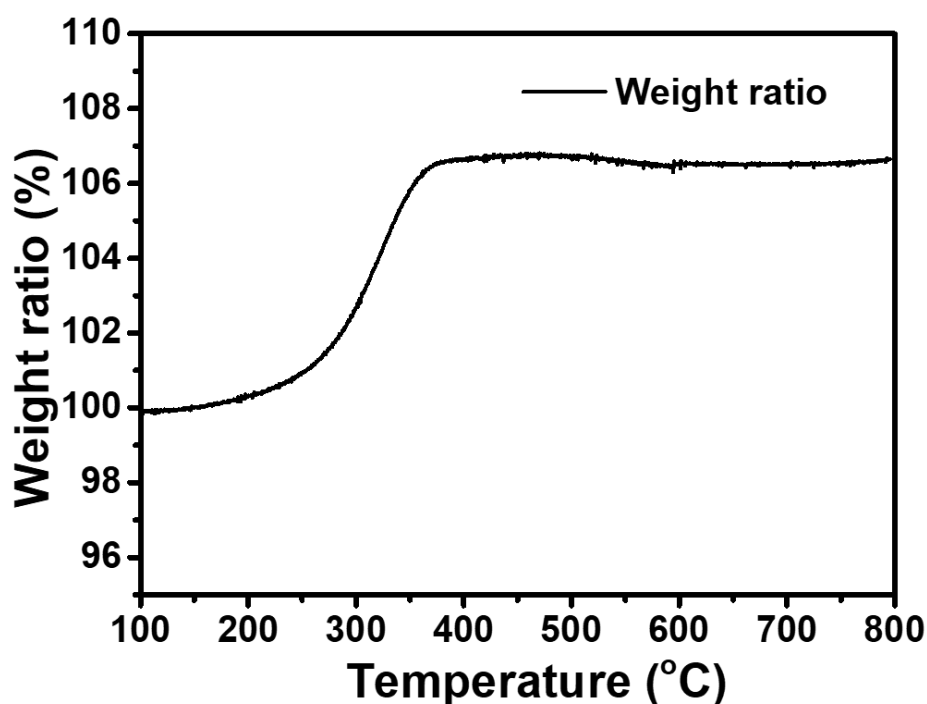


Figure 6.9 TGA graph of TiO_x.

This weight gain is absent in the C/Si profile, proving the sole contribution from TiO_x. The weight increase with C/Si after 600 °C can be attributed to the oxidation of Si, which is barely visible from the C-TiO_x/Si profile, proving the uniform coating of titanium oxide layer that effectively slows Si from being oxidized by the oxidizing atmosphere. Formation of the

integrated Si-based cluster increases the tap density of Si. Photographs of two vials (**Figure 6.10**) containing the same mass of materials (0.4 g) provide a distinct comparison of the C-TiO_x/Si and pristine Si NPs.

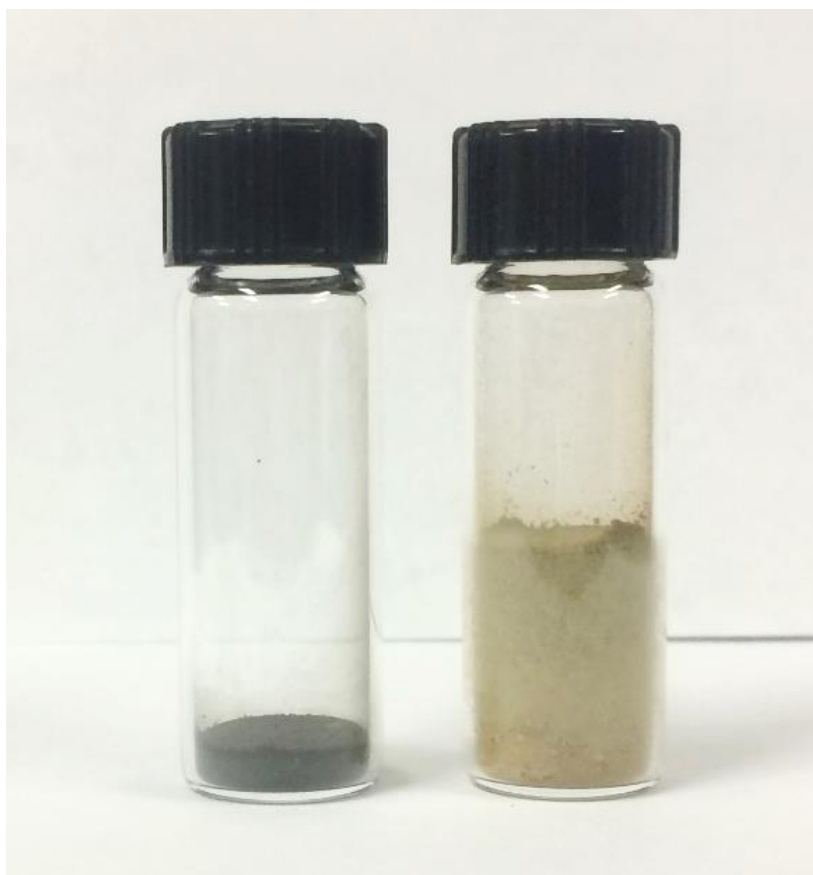


Figure 6.10 Photographs of C-TiO_x/Si and Si NPs with same mass 0.4 g of materials after same condition of mechanical tapping.

Tap density increases from 0.18 g cm⁻³ for Si NPs to 0.88 g cm⁻³ for the micron-sized composite. Nitrogen adsorption/desorption isotherms of C-TiO_x/Si and Si NPs are displayed in Figure 6.8e. The BET surface areas of C-TiO_x/Si and Si NPs are discovered to be 13.44 and 76.68 m² g⁻¹, respectively. A clear decrease in the specific surface area is observed after the synthesis. This result is consistent with previous studies stating that increase of particle size dramatically changes the specific surface area and volumetric density of a material.^{165, 166}

Galvanostatic charge and discharge tests are performed on cells with C-TiO_x/Si and C-TiO₂/Si, respectively. Voltage window of the cells is set to be 0.05-2.5 V in the first three cycles to study the Li⁺ insertion/extraction behaviors of the materials. As shown in **Figure 6.11a** and **b**, an apparent voltage plateau burgeoning from above 0.6 V can be ascribed to the formation of SEI in the C-TiO_x/Si cell. Both C-TiO₂/Si and C/Si cells experience similar SEI formation process in their first discharge. Like many other anodes that have been reported, this plateau is universal in anode materials that have half-cell discharge potential below 1 V. The charge profiles of all three materials are featured with extensive capacity contributions from voltage range from 0.05-0.6 V, which is the characteristic Li⁺ extraction potential of Si. One distinct difference of the profiles between the C-TiO_x/Si and C-TiO₂/Si cells lies at ~2.02 V, where the latter displays a clear plateau, arising from the characteristic extraction behavior of Li⁺ from the octahedral sites of the crystalline anatase TiO₂.¹⁶⁷ This plateau is almost invisible in the C-TiO_x/Si cell, further confirming the hydrogenation effect on the crystalline structure, and thus electrochemical behavior of TiO₂. Another notable difference can be found between the discharge curves of the two materials. There is significant capacity contribution initiating from ~1.75 V in the C-TiO₂/Si discharge profiles, while this feature is absent in the C-TiO_x/Si discharge profiles. This phenomenon can be explained by different lithiation mechanisms with anatase TiO₂ and the largely amorphous TiO_x, which undergo a two-phase reaction and homogeneous lithiation, respectively.¹⁶⁸ The upper charge potential limit is lowered to 1.5 V for both cells after the fourth discharge process to avoid the repetitive lithiation/delithiation of the titanium oxide shells. In the new voltage window of 0.05-1.5V, titanium oxide coatings remain lithiated, providing much enhanced electronic conductivity.¹⁵⁸ Another reason for the

lowering of upper voltage limit in the half-cell testing lies in the fact that practical application requires lower anode lithiation/delithiation potentials (versus. Li/Li^+) to provide higher overall voltages in full-cell LIBs, corresponding to higher energy densities given that same capacity is considered. Li_yTiO_2 is formed when titanium oxide is lithiated, where the y value varies according to the phase and structure of the titanium oxide used. The maximum y value for anatase TiO_2 was found to be 0.5, while y value approaching 1.0 was reported with the amorphous phase.¹⁶⁹ More Li^+ can be hosted in the defect-rich and amorphous TiO_x , facilitating Li-ion diffusion during lithiation/delithiation process of Si.¹⁷⁰ Capacity of the C- TiO_x/Si anode stabilizes at $\sim 1410 \text{ mAh g}^{-1}$ in the first 3 cycles when the voltage window is 0.05-2.5 V and the current density is 100 mA g^{-1} , similar to that of the C- TiO_2/Si . The first-cycle CEs for C- TiO_x/Si and C- TiO_2/Si are 77.1% and 74.3%, respectively. The slight advantage of C- TiO_x/Si can be attributed to the stabilizing effect of the more robust Li_yTiO_2 shell, which promotes the formation of a passivating SEI. Capacities of those two materials are lower than that of the C/Si, which exhibits an initial charge capacity above 2100 mAh g^{-1} (Figure 6.12a). This is mostly due to the higher Si content in the C/Si composite over the other two materials. After the voltage range is adjusted to 0.05-1.5 V, and the current density is maintained at 100 mA g^{-1} , capacities of both C- TiO_x/Si and C- TiO_2/Si cells drop to around 1330 mAh g^{-1} .

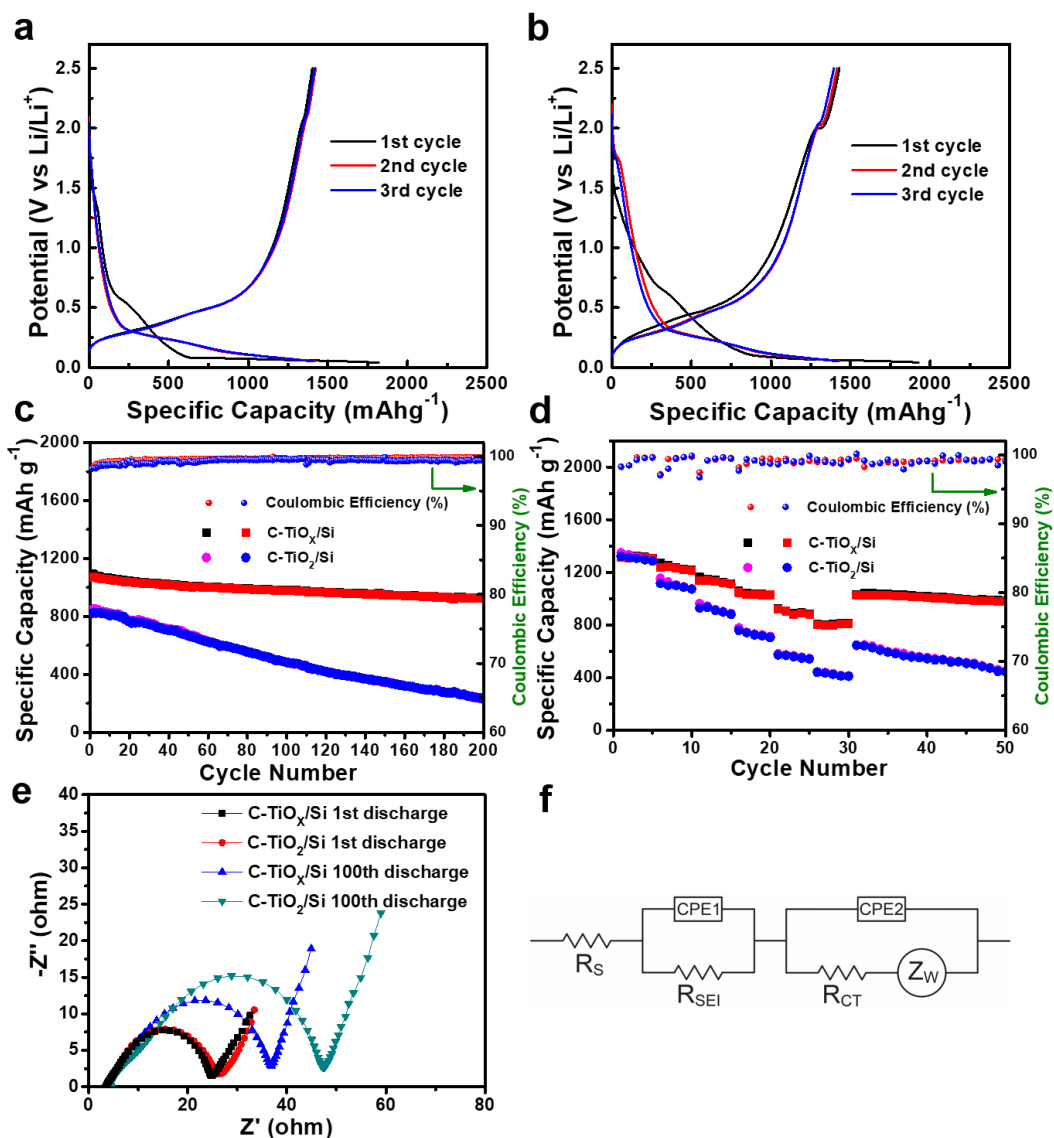


Figure 6.11 Voltage profiles of a) C-TiO_x/Si and b) C-TiO₂/Si for first three cycles at a rate of 0.1 A g⁻¹. c) Cycling performance of C-TiO₂/Si and C-TiO_x/Si at 1 A g⁻¹. d) Rate capability performance of C-TiO₂/Si and C-TiO_x/Si at current densities of 0.1, 0.2, 0.5, 1, 2, 5, and 10 A g⁻¹.

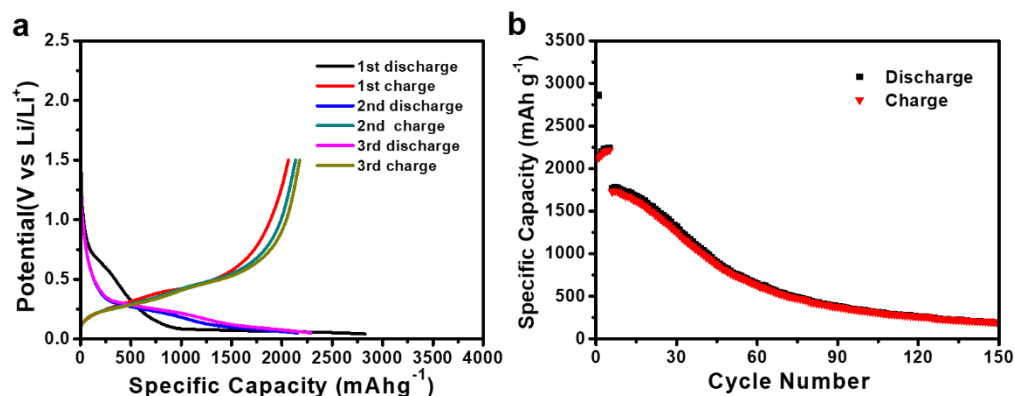


Figure 6.12 a) Voltage profiles of C/Si for first three cycles in the voltage window of 0.05-1.5V at a rate of 0.1 A g⁻¹. b) Cycling performance of C/Si at 1 A g⁻¹ after 5 cycles at 0.1 A g⁻¹.

Cycling stability test is performed at a current density of 1 A g⁻¹ for all cells. As displayed in Figure 6.11c, the initial capacities of C-TiO_x/Si and C-TiO₂/Si cells at 1 A g⁻¹ are 1075 mAh g⁻¹, and 827 mAh g⁻¹, respectively, indicating the superior capacity retaining capability of C-TiO_x/Si at an elevated current density of 1 A g⁻¹. After 200 cycles, capacity retention of 88.1% is achieved for the C-TiO_x/Si cell, with specific capacity being 938 mAh g⁻¹. In comparison, the C-TiO₂/Si cell steadily loses its capacity over cycling, with only 28.2% capacity retention after 200 cycles. As depicted in Figure 6.12b, the C/Si cell shows no sign of capacity decay in the first 5 cycles at a low current density of 100 mA g⁻¹. However, the cell experiences a dramatic capacity decay shortly after the cycling rate is amplified to 1 A g⁻¹. This might be caused by the poor anchoring ability of the C coating on Si surface and thus unstable C/Si structure, which cannot provide effective protection against the inevitable volume change of Si, repetitive SEI formation, and break-up of contact points between Si and the conductive network. A mere 10.8% of the original capacity is left after 150 cycles. As provided in Experimental section, all electrode fabrication parameters were maintained consistent for all

electrodes. Similar mass loading and average electrode thickness of 1.8 mg cm^{-2} and $21.6 \text{ }\mu\text{m}$ are obtained for C-TiO₂/Si and C-TiO_x/Si electrodes, respectively, while C/Si electrodes present a lower mass loading of 1.4 mg g^{-1} and higher thickness of $25.2 \text{ }\mu\text{m}$. Copper foil used in this work has a thickness of $\sim 12 \text{ }\mu\text{m}$. Volumetric densities of cast electrode materials are calculated to be 1.88 g cm^{-3} , and 1.06 g cm^{-3} for C-TiO_x/Si and C/Si electrodes, respectively. Considering the electrochemical performance of these electrodes, it can be concluded that the engineering of C-TiO_x coating matrix not only significantly improves cycling stability of Si, but also greatly increases the volumetric density of the electrode, contributing to enhanced energy density and prolonged durability in a LIB.

The rate performance comparison in Figure 6.11d further corroborates the superior cycling stability of the C-TiO_x/Si electrode, as well as the capacity retention at elevated rates. Specific capacities of 1237, 1142, 1030, 895 and 810 mAh g⁻¹ are obtained at current densities of 0.2, 0.5, 1, 2 and 5 A g⁻¹, respectively. In addition, the C-TiO_x/Si cell gradually stabilizes at each elevated rate. A specific capacity of 1028 mAh g⁻¹ is achieved when the cycling rate is restored to 1 A g⁻¹, similar to the value obtained in the previous rate capability test, indicating excellent structure stability of the material after high-rate lithiation/delithiation. In contrast, the C-TiO₂/Si cell exhibits greater capacity loss over the course of all rate increments. A steady drop in capacity can be observed at each rate. The cell does not recover its capacity when the current density is reversed to 1 A g⁻¹ after rate capability test, and much worse cycling stability is observed at the subsequent cycling test compared to the C-TiO_x/Si cell. Larger capacity gaps between C-TiO_x/Si and C-TiO₂/Si graphs appear when higher rates are applied, confirming the superior rate capability of the C-TiO_x/Si electrode. The following factors regarding the

materials account for the above phenomena. First, the deficiency-rich and largely amorphous nature of the TiO_x , as well as its lithiated derivatives can provide much higher electronic conductivity over the anatase TiO_2 and the corresponding Li_yTiO_2 . The amorphous TiO_x coating possesses much better elasticity and stress-release capability than the anatase TiO_2 , thus can provide a more robust matrix to accommodate the volume change of Si without structural decay. Third, the uniform coating of C- TiO_x layer along with its good structural stability effectively prevents the direct and repetitive contact between Si and electrolyte, and promotes the formation of a stable SEI. The Nyquist plots analyzed from EIS data in Figure 6.11e compare the C- TiO_x/Si cell and C- TiO_x/Si cell after 1st discharge and 100th discharge. The best-fitting equivalent circuit model is displayed in Figure 6.11f. After the 1st discharge, two cells show similar Nyquist plot shape and Ohmic resistance R_s , indicating the consistent and highly-repeatable cell fabrication procedure. The semi-circles obtained from the high-frequency region can be interpreted as the interface (SEI and charge transfer) resistance of the electrode. The near-straight lines after semi-circles from low-frequency region stand for Li^+ diffusion resistance of the electrode.¹⁷¹ The slight difference in the diameter of two semi-circles reflects advantage of the C- TiO_x/Si cell, indicating good charge transfer in titanium oxide shell and SEI. The increase in diameter of the semi-circle in the C- TiO_x/Si plot is much smaller than that in the C- TiO_2/Si plot, which indicates a greater stability of the shell structure and the formed SEI.

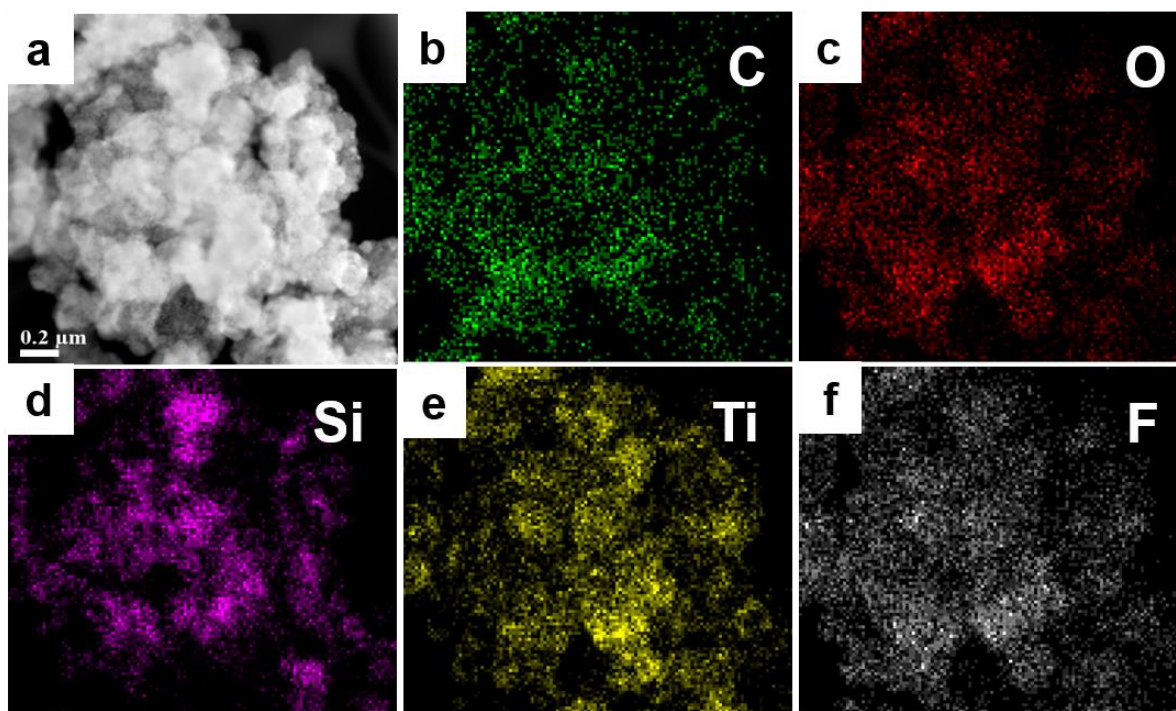


Figure 6.13 a) TEM of a C-TiO_x/Si cluster after cycling, b-f) Elemental mappings of C, O, Si, Ti, and F of the area in a), respectively.

The stable structure of the C-TiO_x/Si cluster is further evidenced by TEM and EDX elemental mapping of the cluster after 100 cycles. As shown in **Figure 6.13a**, Si NPs remain embedded in the robust matrix of carbon and TiO_x, retaining good connectivity between active material and the secondary supporting and conductive cluster. Elemental mappings of C, O, Si, Ti, and F in Figure 6.13b-f largely outline the shape of the cluster. Si mapping in Figure 6.13d can be well overlapped with the Ti signals in Figure 6.13e, further confirming the uniform coating and robust nature of the TiO_x shell. The structure has sufficient stability to withstand the repetitive volume change of Si, which contributes to the prolonged stable cycling of the cell. It is well known that the SEI film is typically composed of LiF, some fluorine-based polymer derived from FEC additive, and other species. Therefore, the F EDX mapping can provide a rough indication of the location of the SEI formations. Interestingly, the F map

(Figure 6.13f) overlaps very well with the Ti map (Figure 6.13e) and also C map (Figure 6.13c). In contrast, the Si map (Figure 6.13d) in fact does not match up well with either F or Ti map. This suggests that the SEI preferentially forms over the protective C-TiO_x shell. This is a crucial characteristic of this material as it promotes the preferential growth of SEI on C or TiO_x over Si. In addition to the core-shell morphology that protects Si, it is possible that other mechanisms might contribute to the preference. One plausible mechanism is that the relative conductive nature of C-TiO_x shell over Si can divert most electron flow through the conductive network formed by C-TiO_x, allowing for electrolyte reduction, instead of through Si. One might argue that carbon will also serve as a preferential surface for SEI growth. However, it is important to note that carbon alone is not able to withstand volume expansion of Si and maintain the structure of the original composite during cycling.

6.4 Summary

In summary, a micron-sized secondary cluster containing Si is developed via the conformal growth of a C-TiO_x coating matrix. Similar to the 2nd project, the transformation from discrete Si NPs into micron-sized clusters significantly improves the tap density of Si and thus contribute to enhanced volumetric density of the electrode. C-TiO_x coating with predominantly amorphous nature not only protects Si from repetitive contact with electrolyte and help form a stable SEI, but also provides a robust structure to host Si and endure the volume changes during lithiation/delithiation. Encapsulation of Si NPs into secondary clusters can effectively secure Si in the original conductive network over cycling and ensure that most Si NPs remain electrochemically active, contributing to prolonged stable cycling of the electrode. Coupled with the simple synthetic approach, the strategy proposed in this research may bear enormous

practical significance for the development of commercially-viable Si anodes.

7. Conclusions and Recommendations

7.1 Conclusions

Si was chosen in this thesis to be the research topic to achieve the objective of boosting the energy density of rechargeable Li-ion batteries. Bearing this in mind, several key strategies were employed to tackle the practical challenges that have been thoroughly reviewed in Chapter 2. Some fundamental considerations in formulating the solutions include taking advantage of nano-sized Si, incorporating conductive carbon materials (graphene, CNTs, amorphous carbon, etc.), constructing conductive and robust host structure for Si, and encapsulating Si with a protective shell and matrix. These considerations were embodied in the designs of experiments in the research projects presented in this thesis.

In Chapter 4, rGO was first utilized to combine with Si NPs. The Si-rGO flakes were further rigidized and interconnected via another step of CVD carbon implantation. The obtained Si-rGO-C composite was rigorously characterized both physically and electrochemically to confirm the successful realization of the desired structure and study the electrochemical performance in a battery. Excellent hydrophilicity of GO and Si NPs contributes to good dispersion in water and subsequent formation of a Si-GO sponge, with Si NPs well distributed on GO sheets. Heat treatment largely reduces GO to rGO, which possesses excellent in-plane electronic conductivity. Final carbon implantation step is essential as it creates an in situ carbon network interconnecting the Si-rGO flakes and further causes the restacking of rGO layers. The Si-rGO-C composite cell maintains a specific capacity over 1400 mAh g⁻¹ at 0.2 C. At 1 C, the cell retains a specific capacity over 840 mAh g⁻¹ after 300 cycles, corresponding to 94% retention of initial capacity. Stabilized cycling of the cell is observed at elevated rates up to 2 C, at which the cell exhibits 770 mAh g⁻¹. The much-enhanced electrochemical performance corroborates the importance of rGO in providing a mechanically stable support and excellent

electronic in-plane conductivity, as well as the formation of conductive network.

In Chapter 5, a micron-sized composite with a mechanically stable and electronically conductive network encasing Si NPs was prepared. The micron-sized spherical structure was formed via a spray-drying process. CNTs and Ketjen black in the composite serve as the conductive agent providing both long-range and short range conductive paths. The partially-cured and cross-linked binders contribute to the excellent mechanical strength and binding ability, supporting the spherical structure and constraining Si NPs in the sphere. Thermal properties of binder polymers were studied in detail to determine an appropriate treatment temperature, at which the polymeric structure is retained, while substantial number of functional groups undergo crosslinking reaction. In this structure, Si NPs are homogeneously and firmly integrated inside the secondary sphere. With this design, volume change of Si can be directed to the voids inside the secondary sphere, which secures Si on its conductive network over cycling, avoiding disconnected active material and loss of capacity that have plagued many nanostructured electrodes. The composite retains 87% (1353mAh g^{-1}) of its initial capacity after 500 cycles at 0.5 C, more than 3 times that of theoretical capacity of graphite anode. The composite also increases the tap density of Si NPs and thus contributes to a higher volumetric energy density of a battery than that with commercial graphite electrode. These results indicate an effective approach to fully take advantage of nanostructured Si and obtain stable cycling performance, without sacrificing the volumetric energy density. More importantly, this technique only requires low temperature throughout the synthesis.

Chapter 6 adopted a core-shell strategy to encapsulate Si NPs with a C-TiO_x shell. This study introduced an effective strategy in harvesting the benefits of nano Si, while eliminating the unfavorable phenomena that arise from nanonization. During the synthesis, TiO₂-coated Si agglomerated into secondary micron-sized clusters, which was also the morphology of the final

product C-TiO_x/Si. The TiO₂ coating was subsequently hydrogenated and transformed to largely amorphous TiO_x before the final carbon layer coating. This composite not only integrates the isolated Si into secondary particles in micron size, but also creates a protective TiO_x layer and conductive carbon coating that target the intrinsic problems with Si anodes. Half-cell batteries made with the composite exhibited an initial capacity of 1330 mA g⁻¹ in the voltage window of 0.05-1.5 V at a current density of 100 mA g⁻¹, and displayed stable long-term cycling with ~88% capacity retention after 200 cycles at 1 A g⁻¹. The C-TiO_x coating not only prevents the repetitive contact between Si and electrolyte, and thus help form a stable SEI, but also provides a conductive and robust host that can endure the volume change of Si and firmly hold Si on the secondary conductive network. Meanwhile, the secondary structure significantly increases the tap density of Si NPs and can ultimately contribute to the improvement in volumetric energy in a LIB.

7.2 Recommendations

Based on the material synthesizes, electrochemical results, and other scientific findings in this study, it is recommended that future work should place more focus on the following aspects:

1. Since the volume expansion is inevitable with Si electrode during lithiation, and it is possible to introduce partially oxidized Si or Si alloy with metals that do not react with Li, so that the intrinsic volume change of SiO_x or Si alloy can be tuned down to 200% or less. Less volume change implies that larger particles can be used without cracking due to stress from volume change. It can be expected that better cycling stability can be achieved when these materials are engineered into composites with the same strategies provided in this thesis, as the volume change shall cause less disturbance to the structure

of secondary composite and conductive network. In addition, the amount of Li inactive compositing material can be reduced, while a good cycling stability can still be maintained.

2. Selection of binder materials may have large impact on the electrochemical performance on Si based materials, Chapter 5 utilizes PAA and CMC for the formation of secondary sphere, and CMC is utilized in all projects as a binder for electrode preparation. The interaction between binder and Si should be further investigated to theorize a clear mechanism on how functional groups in binders can affect the electrode performance. Once successful, binders can be custom designed with desired functional groups and properties for different Si based anodes.
3. Formation mechanism of SEI on different types of coating materials/morphologies on Si should be further studied for researchers to have a better understanding on the significance of material selection in composite materials. The properties that can be of interest for investigation include electronic conductivity, Li insertion/extraction capability, redox potentials vs. Li/Li^+ .
4. A universally-comparable performance evaluation standard should be adopted by academia, and more parameters that are sought by industry should be provided, such as electrode loading, thickness, electrode thickness change during charge and discharge. To achieve the ultimate goal of high energy batteries, electrodes developed with different precursors, through different approaches, from different research groups should be comparable with each other. After all, it is as important to make scientific discoveries and translate them into practical applications.

References

1. U.S. Energy Information Administration "International Energy Outlook 2017". Available online at [https://www.eia.gov/outlooks/ieo/pdf/0484\(2017\).pdf](https://www.eia.gov/outlooks/ieo/pdf/0484(2017).pdf) (2017).
2. U.S. Environmental Protection Agency "DRAFT Inventory of U.S. Greenhouse Gas Emissions and Sinks" Available online at https://www.epa.gov/sites/production/files/2018-01/documents/2018_complete_report.pdf (2018).
3. Etacheri, V., Marom, R., Elazari, R., Salitra, G. & Aurbach, D. Challenges in the Development of Advanced Li-ion Batteries: a Review. *Energy & Environmental Science* **4**, 3243-3262 (2011).
4. Szczech, J.R. & Jin, S. Nanostructured Silicon for High Capacity Lithium Battery Anodes. *Energy & Environmental Science* **4**, 56-72 (2011).
5. U.S. Advanced Battery Consortium LLC. "EV Battery Goals". Available for downloading via link: http://www.uscar.org/guest/article_view.php?articles_id=85
6. McDowell, M.T., Lee, S.W., Nix, W.D. & Cui, Y. 25th Anniversary Article: Understanding the Lithiation of Silicon and Other Alloying Anodes for Lithium-Ion Batteries. *Advanced Materials* **25**, 4966-4984 (2013).
7. Chen, X.L. et al. Conductive Rigid Skeleton Supported Silicon as High-Performance Li-Ion Battery Anodes. *Nano Lett* **12**, 4124-4130 (2012).
8. Teki, R. et al. Nanostructured Silicon Anodes for Lithium Ion Rechargeable Batteries. *Small* **5**, 2236-2242 (2009).
9. Wu, H. et al. Engineering Empty Space between Si Nanoparticles for Lithium-Ion Battery Anodes. *Nano Letters* **12**, 904-909 (2012).
10. Watanabe, N.F., M. Primary cell for electric batteries. *U.S. Patent 3,536,532* (1970).
11. Whittingham, M.S. Lithium Batteries and Cathode Materials. *Chemical Reviews* **104**, 4271-4301 (2004).
12. Whittingham, M.S. Electrical Energy-Storage and Intercalation Chemistry. *Science* **192**, 1126-1127 (1976).

13. Thompson, A.H. & Whittingham, M.S. Transition-Metal Phosphorus Trisulfides as Battery Cathodes. *Materials Research Bulletin* **12**, 741-744 (1977).
14. Murphy, D.W. & Christian, P.A. Solid-State Electrodes for High-Energy Batteries. *Science* **205**, 651-656 (1979).
15. Ozawa, K. Lithium-Ion Rechargeable Batteries with LiCoO₂ and Carbon Electrodes - the LiCoO₂ C System. *Solid State Ionics* **69**, 212-221 (1994).
16. Thackeray, M.M., David, W.I.F., Bruce, P.G. & Goodenough, J.B. Lithium Insertion into Manganese Spinel. *Materials Research Bulletin* **18**, 461-472 (1983).
17. Padhi, A.K., Nanjundaswamy, K.S. & Goodenough, J.B. Phospho-olivines as positive-electrode materials for rechargeable lithium batteries. *Journal Of the Electrochemical Society* **144**, 1188-1194 (1997).
18. Shaju, K.M., Rao, G.V.S. & Chowdari, B.V.R. Performance of layered Li(Ni_{1/3}Co_{1/3}Mn_{1/3})O₂ as cathode for Li-ion batteries. *Electrochimica Acta* **48**, 145-151 (2002).
19. Wu, Y.P., Rahm, E. & Holze, R. Carbon anode materials for lithium ion batteries. *Journal of Power Sources* **114**, 228-236 (2003).
20. Goriparti, S. et al. Review on recent progress of nanostructured anode materials for Li-ion batteries. *Journal of Power Sources* **257**, 421-443 (2014).
21. Tarascon, J.M. & Armand, M. Issues and challenges facing rechargeable lithium batteries. *Nature* **414**, 359-367 (2001).
22. Armand, M. & Tarascon, J.M. Building Better Batteries. *Nature* **451**, 652-7 (2008).
23. Antolini, E. LiCoO₂: formation, structure, lithium and oxygen nonstoichiometry, electrochemical behaviour and transport properties. *Solid State Ionics* **170**, 159-171 (2004).
24. Goodenough, J.B. & Kim, Y. Challenges for Rechargeable Li Batteries. *Chemistry of Materials* **22**, 587-603 (2010).
25. Winter, M. & Brodd, R.J. What are batteries, fuel cells, and supercapacitors? *Chemical Reviews*

- 104**, 4245-4269 (2004).
26. Inaba, M. in *Encyclopedia of Electrochemical Power Sources* 198-208 (Elsevier, Amsterdam, 2009).
 27. Zheng, F., Yang, Y. & Chen, Q. High lithium anodic performance of highly nitrogen-doped porous carbon prepared from a metal-organic framework. *Nature Communications* **5**, 5261 (2014).
 28. Whittingham, M.S. Electrical energy storage and intercalation chemistry. *Science* **192**, 1126-7 (1976).
 29. Yan, K. et al. Ultrathin Two-Dimensional Atomic Crystals as Stable Interfacial Layer for Improvement of Lithium Metal Anode. *Nano Lett* **14**, 6016-6022 (2014).
 30. Bouchet, R. BATTERIES A stable lithium metal interface. *Nature Nanotechnology* **9**, 572-573 (2014).
 31. Zheng, G.Y. et al. Interconnected hollow carbon nanospheres for stable lithium metal anodes. *Nature Nanotechnology* **9**, 618-623 (2014).
 32. Mukherjee, R. et al. Defect-induced plating of lithium metal within porous graphene networks. *Nature Communications* **5**, 3710 (2014).
 33. Shimoi, N. & Tanaka, Y. Improvement in Si active material particle performance for lithium-ion batteries by surface modification of an inductivity coupled plasma-chemical vapor deposition. *Electrochimica Acta* **80**, 227-232 (2012).
 34. Xue, D.J. et al. Improving the Electrode Performance of Ge through Ge@C Core-Shell Nanoparticles and Graphene Networks. *Journal of the American Chemical Society* **134**, 2512-2515 (2012).
 35. Aravindan, V., Lee, Y.-S. & Madhavi, S. Research Progress on Negative Electrodes for Practical Li-Ion Batteries: Beyond Carbonaceous Anodes. *Advanced Energy Materials* **5**, 1402225 (2015).
 36. Ren, H. et al. Multishelled TiO₂ Hollow Microspheres as Anodes with Superior Reversible Capacity for Lithium Ion Batteries. *Nano Lett* **14**, 6679-6684 (2014).

37. Wang, C. et al. High sulfur loading composite wrapped by 3D nitrogen-doped graphene as a cathode material for lithium-sulfur batteries. *Journal of Materials Chemistry A* **2**, 5018-5023 (2014).
38. Zhang, N. et al. 3D Porous gamma-Fe₂O₃@C Nanocomposite as High-Performance Anode Material of Na-Ion Batteries. *Advanced Energy Materials* **5**, 1401123 (2015).
39. Yue, J. et al. General synthesis of hollow MnO₂, Mn₃O₄ and MnO nanospheres as superior anode materials for lithium ion batteries. *Journal of Materials Chemistry A* **2**, 17421-17426 (2014).
40. Wang, D.L. et al. Template-Free Synthesis of Hollow-Structured Co₃O₄ Nanoparticles as High-Performance Anodes for Lithium-Ion Batteries. *Acs Nano* **9**, 1775-1781 (2015).
41. Wang, Y., Su, D.W., Ung, A., Ahn, J.H. & Wang, G.X. Hollow CoFe₂O₄ nanospheres as a high capacity anode material for lithium ion batteries. *Nanotechnology* **23**, 055402 (2012).
42. Zhou, X.S., Yin, Y.X., Wan, L.J. & Guo, Y.G. A robust composite of SnO₂ hollow nanospheres enwrapped by graphene as a high-capacity anode material for lithium-ion batteries. *Journal of Materials Chemistry* **22**, 17456-17459 (2012).
43. Yoshio M, B.R., Kozawa A. Lithium-ion batteries : science and technologies *Springer: New York*. (2009).
44. Mizushima, K., Jones, P.C., Wiseman, P.J. & Goodenough, J.B. Li_xCoO₂ "(0 less than x less than or equal to 1) - a New Cathode Material for Batteries of High-Energy Density. *Materials Research Bulletin* **15**, 783-789 (1980).
45. Kim, D.K. et al. Spinel LiMn₂O₄ Nanorods as Lithium Ion Battery Cathodes. *Nano Lett* **8**, 3948-3952 (2008).
46. Hu, Y.Q., Doeff, M.M., Kostecki, R. & Finones, R. Electrochemical performance of sol-gel synthesized LiFePO₄ in lithium batteries. *Journal of the Electrochemical Society* **151**, A1279-A1285 (2004).
47. Li, J.L., Cao, C.B., Xu, X.Y., Zhu, Y.Q. & Yao, R.M. LiNi_{1/3}Co_{1/3}Mn_{1/3}O₂ hollow nano-micro hierarchical microspheres with enhanced performances as cathodes for lithium-ion

- batteries. *Journal of Materials Chemistry A* **1**, 11848-11852 (2013).
48. Wang, F.X., Xiao, S.Y., Chang, Z., Yang, Y.Q. & Wu, Y.P. Nanoporous $\text{LiNi}_{1/3}\text{Co}_{1/3}\text{Mn}_{1/3}\text{O}_2$ as an ultra-fast charge cathode material for aqueous rechargeable lithium batteries. *Chemical Communications* **49**, 9209-9211 (2013).
 49. Lu, Z.H., MacNeil, D.D. & Dahn, J.R. Layered cathode materials $\text{Li}[\text{Ni}_x\text{Li}_{(1/3-2x/3)}\text{Mn}_{(2/3-x/3)}]\text{O}_2$ for lithium-ion batteries. *Electrochemical and Solid State Letters* **4**, A191-A194 (2001).
 50. Liu, C.F., Neale, Z.G. & Cao, G.Z. Understanding electrochemical potentials of cathode materials in rechargeable batteries. *Materials Today* **19**, 109-123 (2016).
 51. Hayashi, K., Nemoto, Y., Tobishima, S. & Yamaki, J. Mixed solvent electrolyte for high voltage lithium metal secondary cells. *Electrochimica Acta* **44**, 2337-2344 (1999).
 52. Egashira, M., Takahashi, H., Okada, S. & Yamaki, J. Measurement of the electrochemical oxidation of organic electrolytes used in lithium batteries by microelectrode. *Journal of Power Sources* **92**, 267-271 (2001).
 53. Yazami, R. Surface chemistry and lithium storage capability of the graphite-lithium electrode. *Electrochimica Acta* **45**, 87-97 (1999).
 54. Koch, V.R., Dominey, L.A., Nanjundiah, C. & Ondrechen, M.J. The intrinsic anodic stability of several anions comprising solvent-free ionic liquids. *Journal of the Electrochemical Society* **143**, 798-803 (1996).
 55. Fuller, J., Carlin, R.T. & Osteryoung, R.A. The room temperature ionic liquid 1-ethyl-3-methylimidazolium tetrafluoroborate: Electrochemical couples and physical properties. *Journal of the Electrochemical Society* **144**, 3881-3886 (1997).
 56. Stassen, I. & Hambitzer, G. Metallic lithium batteries for high power applications. *Journal of Power Sources* **105**, 145-150 (2002).
 57. Croce, F., Appetecchi, G.B., Persi, L. & Scrosati, B. Nanocomposite polymer electrolytes for lithium batteries. *Nature* **394**, 456-458 (1998).
 58. Appetecchi, G.B. et al. Lithium insertion into carbonaceous materials and transition metal

- oxides from high performance polymer electrolytes. *Electrochimica Acta* **45**, 23-30 (1999).
59. Etacheri, V. et al. Effect of Fluoroethylene Carbonate (FEC) on the Performance and Surface Chemistry of Si-Nanowire Li-Ion Battery Anodes. *Langmuir* **28**, 965-976 (2012).
60. Han, G.B., Ryou, M.H., Cho, K.Y., Lee, Y.M. & Park, J.K. Effect of succinic anhydride as an electrolyte additive on electrochemical characteristics of silicon thin-film electrode. *Journal Of Power Sources* **195**, 3709-3714 (2010).
61. Li, S.Y. et al. Electrochemical performances of two kinds of electrolytes based on lithium bis(oxalate)borate and sulfolane for advanced lithium ion batteries. *Journal of Power Sources* **209**, 295-300 (2012).
62. Dalavi, S., Guduru, P. & Lucht, B.L. Performance Enhancing Electrolyte Additives for Lithium Ion Batteries with Silicon Anodes. *Journal Of the Electrochemical Society* **159**, A642-A646 (2012).
63. Chou, S.L., Pan, Y.D., Wang, J.Z., Liu, H.K. & Dou, S.X. Small things make a big difference: binder effects on the performance of Li and Na batteries. *Physical Chemistry Chemical Physics* **16**, 20347-20359 (2014).
64. Lee, J.H., Paik, U., Hackley, V.A. & Choi, Y.M. Effect of carboxymethyl cellulose on aqueous processing of natural graphite negative electrodes and their electrochemical performance for lithium batteries. *Journal of the Electrochemical Society* **152**, A1763-A1769 (2005).
65. Chong, J. et al. A comparative study of polyacrylic acid and poly(vinylidene difluoride) binders for spherical natural graphite/LiFePO₄ electrodes and cells. *Journal of Power Sources* **196**, 7707-7714 (2011).
66. Li, J., Lewis, R.B. & Dahn, J.R. Sodium carboxymethyl cellulose - A potential binder for Si negative electrodes for Li-ion batteries. *Electrochemical and Solid State Letters* **10**, A17-A20 (2007).
67. Lestrie, B., Bahri, S., Sandu, I., Roue, L. & Guyomard, D. On the binding mechanism of CMC in Si negative electrodes for Li-ion batteries. *Electrochemistry Communications* **9**, 2801-2806 (2007).

68. Hochgatterer, N.S. et al. Silicon/graphite composite electrodes for high-capacity anodes: Influence of binder chemistry on cycling stability. *Electrochemical and Solid State Letters* **11**, A76-A80 (2008).
69. Song, J.X. et al. Interpenetrated Gel Polymer Binder for High-Performance Silicon Anodes in Lithium-ion Batteries. *Advanced Functional Materials* **24**, 5904-5910 (2014).
70. Koo, B. et al. A Highly Cross-Linked Polymeric Binder for High-Performance Silicon Negative Electrodes in Lithium Ion Batteries. *Angewandte Chemie-International Edition* **51**, 8762-8767 (2012).
71. Jeong, Y.K. et al. Millipede-inspired structural design principle for high performance polysaccharide binders in silicon anodes. *Energy & Environmental Science* **8**, 1224-1230 (2015).
72. Guerfi, A., Kaneko, M., Petitclerc, M., Mori, M. & Zaghib, K. LiFePO₄ water-soluble binder electrode for Li-ion batteries. *Journal of Power Sources* **163**, 1047-1052 (2007).
73. Liu, X.H. et al. In situ atomic-scale imaging of electrochemical lithiation in silicon. *Nature Nanotechnology* **7**, 749-756 (2012).
74. Key, B. et al. Real-Time NMR Investigations of Structural Changes in Silicon Electrodes for Lithium-Ion Batteries. *Journal Of the American Chemical Society* **131**, 9239-9249 (2009).
75. Chen, C.Y. et al. In situ Scanning Electron Microscopy of Silicon Anode Reactions in Lithium-Ion Batteries during Charge/Discharge Processes. *Scientific Reports* **6**, 36153 (2016).
76. Yen, Y.C., Chao, S.C., Wu, H.C. & Wu, N.L. Study on Solid-Electrolyte-Interphase of Si and C-Coated Si Electrodes in Lithium Cells. *Journal of the Electrochemical Society* **156**, A95-A102 (2009).
77. Wen, Y. et al. Graphene-Bonded and -Encapsulated Si Nanoparticles for Lithium Ion Battery Anodes. *Small* **9**, 2810-2816 (2013).
78. Roduner, E. Size matters: why nanomaterials are different. *Chemical Society Reviews* **35**, 583-592 (2006).
79. Arico, A.S., Bruce, P., Scrosati, B., Tarascon, J.M. & van Schalkwijk, W. Nanostructured

- materials for advanced energy conversion and storage devices. *Nature Materials* **4**, 366-77 (2005).
80. Beaulieu, L.Y., Eberman, K.W., Turner, R.L., Krause, L.J. & Dahn, J.R. Colossal reversible volume changes in lithium alloys. *Electrochemical and Solid State Letters* **4**, A137-A140 (2001).
 81. Beaulieu, L.Y., Hatchard, T.D., Bonakdarpour, A., Fleischauer, M.D. & Dahn, J.R. Reaction of Li with alloy thin films studied by in situ AFM. *Journal of the Electrochemical Society* **150**, A1457-A1464 (2003).
 82. Li, H., Wang, Z.X., Chen, L.Q. & Huang, X.J. Research on Advanced Materials for Li-ion Batteries. *Advanced Materials* **21**, 4593-4607 (2009).
 83. Ge, M.Y. et al. Scalable Preparation of Porous Silicon Nanoparticles And Their Application for Lithium-ion Battery Anodes. *Nano Research* **6**, 174-181 (2013).
 84. Chen, W., Fan, Z.L., Dhanabalan, A., Chen, C.H. & Wang, C.L. Mesoporous Silicon Anodes Prepared by Magnesiothermic Reduction for Lithium Ion Batteries. *Journal of the Electrochemical Society* **158**, A1055-A1059 (2011).
 85. Yao, Y. et al. Interconnected Silicon Hollow Nanospheres for Lithium-Ion Battery Anodes with Long Cycle Life. *Nano Letters* **11**, 2949-2954 (2011).
 86. Nguyen, H.T. et al. Highly Interconnected Si Nanowires for Improved Stability Li-Ion Battery Anodes. *Advanced Energy Materials* **1**, 1154-1161 (2011).
 87. Xiao, Q.Z., Zhang, Q., Fan, Y., Wang, X.H. & Susantyoko, R.A. Soft silicon anodes for lithium ion batteries. *Energy & Environmental Science* **7**, 2261-2268 (2014).
 88. Song, T. et al. Arrays of Sealed Silicon Nanotubes As Anodes for Lithium Ion Batteries. *Nano Letters* **10**, 1710-1716 (2010).
 89. Ohara, S., Suzuki, J., Sekine, K. & Takamura, T. A thin film silicon anode for Li-ion batteries having a very large specific capacity and long cycle life. *Journal of Power Sources* **136**, 303-306 (2004).
 90. Li, M. et al. Facile spray-drying/pyrolysis synthesis of core-shell structure graphite/silicon-

- porous carbon composite as a superior anode for Li-ion batteries. *Journal Of Power Sources* **248**, 721-728 (2014).
91. Jung, D.S., Hwang, T.H., Park, S.B. & Choi, J.W. Spray Drying Method for Large-Scale and High-Performance Silicon Negative Electrodes in Li-Ion Batteries. *Nano Letters* **13**, 2092-2097 (2013).
 92. Magasinski, A. et al. High-performance lithium-ion anodes using a hierarchical bottom-up approach. *Nature Materials* **9**, 353-358 (2010).
 93. Kim, H., Seo, M., Park, M.H. & Cho, J. A Critical Size of Silicon Nano-Anodes for Lithium Rechargeable Batteries. *Angewandte Chemie-International Edition* **49**, 2146-2149 (2010).
 94. Mazouzi, D., Lestriez, B., Roue, L. & Guyomard, D. Silicon Composite Electrode with High Capacity and Long Cycle Life. *Electrochemical and Solid State Letters* **12**, A215-A218 (2009).
 95. Liu, Y. et al. Silicon/carbon composites as anode materials for Li-ion batteries. *Electrochemical and Solid State Letters* **7**, A369-A372 (2004).
 96. Du, Z.J. et al. Facile fabrication of reticular polypyrrole-silicon core-shell nanofibers for high performance lithium storage. *Journal of Materials Chemistry* **22**, 11636-11641 (2012).
 97. Klankowski, S.A. et al. A high-performance lithium-ion battery anode based on the core-shell heterostructure of silicon-coated vertically aligned carbon nanofibers. *Journal of Materials Chemistry A* **1**, 1055-1064 (2013).
 98. Jeong, G. et al. Core-Shell Structured Silicon Nanoparticles@TiO₂-x/Carbon Mesoporous Microfiber Composite as a Safe and High-Performance Lithium-Ion Battery Anode. *Acs Nano* **8**, 2977-2985 (2014).
 99. Novoselov, K.S. et al. Electric field effect in atomically thin carbon films. *Science* **306**, 666-669 (2004).
 100. Novoselov, K.S. et al. A roadmap for graphene. *Nature* **490**, 192-200 (2012).
 101. Bonaccorso, F. et al. Graphene, related two-dimensional crystals, and hybrid systems for energy conversion and storage. *Science* **347**, 6217 (2015).

102. Stankovich, S. et al. Graphene-based composite materials. *Nature* **442**, 282-286 (2006).
103. Yoo, E. et al. Large reversible Li storage of graphene nanosheet families for use in rechargeable lithium ion batteries. *Nano Letters* **8**, 2277-2282 (2008).
104. Li, X.F. et al. Superior cycle stability of nitrogen-doped graphene nanosheets as anodes for lithium ion batteries. *Electrochemistry Communications* **13**, 822-825 (2011).
105. Wang, D.H. et al. Self-Assembled TiO₂-Graphene Hybrid Nanostructures for Enhanced Li-Ion Insertion. *Acs Nano* **3**, 907-914 (2009).
106. Li, N., Chen, Z.P., Ren, W.C., Li, F. & Cheng, H.M. Flexible graphene-based lithium ion batteries with ultrafast charge and discharge rates. *Proceedings Of the National Academy Of Sciences Of the United States Of America* **109**, 17360-17365 (2012).
107. Prato, M., Kostarelos, K. & Bianco, A. Functionalized carbon nanotubes in drug design and discovery. *Accounts Of Chemical Research* **41**, 60-68 (2008).
108. Zhang, W.X., Zhang, Z.Z. & Zhang, Y.G. The application of carbon nanotubes in target drug delivery systems for cancer therapies. *Nanoscale Research Letters* **6**, 555 (2011).
109. Dillon, A.C. Carbon Nanotubes for Photoconversion and Electrical Energy Storage. *Chemical Reviews* **110**, 6856-6872 (2010).
110. Frackowiak, E. & Beguin, F. Electrochemical storage of energy in carbon nanotubes and nanostructured carbons. *Carbon* **40**, 1775-1787 (2002).
111. Chen, Z. et al. Highly Active and Durable Core-Corona Structured Bifunctional Catalyst for Rechargeable Metal-Air Battery Application. *Nano Letters* **12**, 1946-1952 (2012).
112. Mauter, M.S. & Elimelech, M. Environmental applications of carbon-based nanomaterials. *Environmental Science & Technology* **42**, 5843-5859 (2008).
113. Tan, C.W. et al. Energy and environmental applications of carbon nanotubes. *Environmental Chemistry Letters* **10**, 265-273 (2012).
114. Abel, P.R. et al. Nanostructured Si(i-x)Ge_x for Tunable Thin Film Lithium-Ion Battery Anodes. *Acs Nano* **7**, 2249-2257 (2013).

115. Fleischauer, M.D., Obrovac, M.N. & Dahn, J.R. Al-Si thin-film negative electrodes for Li-ion batteries. *Journal of the Electrochemical Society* **155**, A851-A854 (2008).
116. Electrode compositions based on an amorphous alloy having a high silicon content 3M. *US Pat.*, 7732095 B2, 2011.
117. Kim, H., Han, B., Choo, J. & Cho, J. Three-Dimensional Porous Silicon Particles for Use in High-Performance Lithium Secondary Batteries. *Angewandte Chemie-International Edition* **47**, 10151-10154 (2008).
118. Liu, N. et al. A Pomegranate-Inspired Nanoscale Design for Large-Volume-Change Lithium Battery Anodes. *Nature Nanotechnology* **9**, 187-192 (2014).
119. Liu, Y. et al. Electrochemical behaviors of Si/C composite synthesized from F-containing precursors. *Journal of Power Sources* **189**, 733-737 (2009).
120. Liu, N. et al. A Yolk-Shell Design for Stabilized and Scalable Li-Ion Battery Alloy Anodes. *Nano Letters* **12**, 3315-3321 (2012).
121. Lee, J.K., Smith, K.B., Hayner, C.M. & Kung, H.H. Silicon nanoparticles-graphene paper composites for Li ion battery anodes. *Chemical Communications* **46**, 2025-2027 (2010).
122. Fan, Y., Zhang, Q., Xiao, Q.Z., Wang, X.H. & Huang, K. High performance lithium ion battery anodes based on carbon nanotube-silicon core-shell nanowires with controlled morphology. *Carbon* **59**, 264-269 (2013).
123. Wu, H. et al. Stable Li-ion battery anodes by in-situ polymerization of conducting hydrogel to conformally coat silicon nanoparticles. *Nature Communications* **4**, 1943 (2013).
124. Lee, J.I. et al. High-performance silicon-based multicomponent battery anodes produced via synergistic coupling of multifunctional coating layers. *Energy & Environmental Science* **8**, 2075-2084 (2015).
125. Goldstein, J., Newbury, D.E., Joy, D.C., Lyman, C.E., Echlin, P., Lifshin, E., Sawyer, L., Michael, J.R. Scanning electron microscopy and X-ray microanalysis. *Springer* (2003).
126. Feng, K. et al. Implementing an in-situ carbon network in Si/reduced graphene oxide for high performance lithium-ion battery anodes. *Nano Energy* **19**, 187-197 (2016).

127. Zhou, X.S., Yin, Y.X., Wan, L.J. & Guo, Y.G. Self-Assembled Nanocomposite of Silicon Nanoparticles Encapsulated in Graphene through Electrostatic Attraction for Lithium-Ion Batteries. *Advanced Energy Materials* **2**, 1086-1090 (2012).
128. Zhou, X.S., Yin, Y.X., Wan, L.J. & Guo, Y.G. Facile Synthesis of Silicon Nanoparticles Inserted into Graphene Sheets as Improved Anode Materials for Lithium-ion Batteries. *Chemical Communications* **48**, 2198-2200 (2012).
129. Chabot, V. et al. Graphene Wrapped Silicon Nanocomposites for Enhanced Electrochemical Performance in Lithium Ion Batteries. *Electrochimica Acta* **130**, 127-134 (2014).
130. Kwon, S.M., Kim, H.S. & Jin, H.J. Multiwalled carbon nanotube cryogels with aligned and non-aligned porous structures. *Polymer* **50**, 2786-2792 (2009).
131. Akhavan, O. & Ghaderi, E. Escherichia Coli Bacteria Reduce Graphene Oxide to Bactericidal Graphene in a Self-limiting Manner. *Carbon* **50**, 1853-1860 (2012).
132. Chang, J.B. et al. Multilayered Si Nanoparticle/Reduced Graphene Oxide Hybrid as a High-Performance Lithium-Ion Battery Anode. *Advanced Materials* **26**, 758-764 (2014).
133. Yang, D. et al. Chemical Analysis of Graphene Oxide Films After Heat and Chemical Treatments by X-ray Photoelectron and Micro-Raman Spectroscopy. *Carbon* **47**, 145-152 (2009).
134. Pollak, E., Salitra, G., Baranchugov, V. & Aurbach, D. In Situ Conductivity, Impedance Spectroscopy, and ex Situ Raman Spectra of Amorphous Silicon during the Insertion/Extraction of Lithium. *Journal of Physical Chemistry C* **111**, 11437-11444 (2007).
135. Lin, Y.M. et al. High Performance Silicon Nanoparticle Anode in Fluoroethylene Carbonate-based Electrolyte for Li-ion Batteries. *Chemical Communications* **48**, 7268-7270 (2012).
136. Chan, C.K. et al. High-performance lithium battery anodes using silicon nanowires. *Nature Nanotechnology* **3**, 31-35 (2008).
137. Wen, Z.H. et al. Silicon Nanotube Anode for Lithium-ion Batteries. *Electrochemistry Communications* **29**, 67-70 (2013).
138. Rahman, M.A., Song, G.S., Bhatt, A.I., Wong, Y.C. & Wen, C.E. Nanostructured Silicon

- Anodes for High-Performance Lithium-Ion Batteries. *Advanced Functional Materials* **26**, 647-678 (2016).
139. Liu, H.K., Guo, Z.P., Wang, J.Z. & Konstantinov, K. Si-based anode materials for lithium rechargeable batteries. *Journal of Materials Chemistry* **20**, 10055-10057 (2010).
 140. Yin, Y.X., Xin, S., Wan, L.J., Li, C.J. & Guo, Y.G. Electrospray Synthesis of Silicon/Carbon Nanoporous Microspheres as Improved Anode Materials for Lithium-Ion Batteries. *Journal of Physical Chemistry C* **115**, 14148-14154 (2011).
 141. Yang, J.P. et al. Yolk-shell silicon-mesoporous carbon anode with compact solid electrolyte interphase film for superior lithium-ion batteries. *Nano Energy* **18**, 133-142 (2015).
 142. Li, S. et al. Silicon/carbon composite microspheres with hierarchical core-shell structure as anode for lithium ion batteries. *Electrochemistry Communications* **49**, 98-102 (2014).
 143. Ashuri, M., He, Q.R. & Shaw, L.L. Silicon as a potential anode material for Li-ion batteries: where size, geometry and structure matter. *Nanoscale* **8**, 74-103 (2016).
 144. Choi, J.W. & Aurbach, D. Promise and reality of post-lithium-ion batteries with high energy densities. *Nature Reviews Materials* **1**, 16013 (2016).
 145. Xu, Q. et al. Watermelon-Inspired Si/C Microspheres with Hierarchical Buffer Structures for Densely Compacted Lithium-Ion Battery Anodes. *Advanced Energy Materials* **7**, 1601481 (2016).
 146. Bridel, J.S., Azais, T., Morcrette, M., Tarascon, J.M. & Larcher, D. Key Parameters Governing the Reversibility of Si/Carbon/CMC Electrodes for Li-Ion Batteries. *Chemistry Of Materials* **22**, 1229-1241 (2010).
 147. Xie, L. et al. The Electrochemical Performance of Carboxymethyl Cellulose Lithium as a Binding Material for Anthraquinone Cathodes in Lithium Batteries. *Journal Of the Electrochemical Society* **159**, A499-A505 (2012).
 148. Feng, K. et al. Silicon-Based Anodes for Lithium-Ion Batteries: From Fundamentals to Practical Applications. *Small* **14**, 1702737 (2018).
 149. Hagen, M. et al. Lithium-Sulfur Cells: The Gap between the State-of-the-Art and the

- Requirements for High Energy Battery Cells. *Advanced Energy Materials* **5**, 1401986 (2015).
150. Pope, M.A. & Aksay, I.A. Structural Design of Cathodes for Li-S Batteries. *Advanced Energy Materials* **5**, 1500124 (2015).
 151. Liu, Y. & Yang, Y.F. Recent Progress of TiO₂-Based Anodes for Li Ion Batteries. *Journal Of Nanomaterials* **2016**, 15 (2016).
 152. Zhang, Y.Y., Tang, Y.X., Li, W.L. & Chen, X.D. Nanostructured TiO₂-Based Anode Materials for High-Performance Rechargeable Lithium-Ion Batteries. *Chemnanomat* **2**, 764-775 (2016).
 153. Tang, Y. et al. Mechanical Force-Driven Growth of Elongated Bending TiO₂-based Nanotubular Materials for Ultrafast Rechargeable Lithium Ion Batteries. *Advanced Materials* **26**, 6111-6118 (2014).
 154. Wu, Q.L., Tran, T., Lu, W.Q. & Wu, J. Electrospun silicon/carbon/titanium oxide composite nanofibers for lithium ion batteries. *Journal Of Power Sources* **258**, 39-45 (2014).
 155. Brumbarov, J. & Kunze-Liebhauser, J. Silicon on conductive self-organized TiO₂ nanotubes - A high capacity anode material for Li-ion batteries. *Journal Of Power Sources* **258**, 129-133 (2014).
 156. Luo, W. et al. Silicon/Mesoporous Carbon/Crystalline TiO₂ Nanoparticles for Highly Stable Lithium Storage. *Acs Nano* **10**, 10524-10532 (2016).
 157. Maroni, F., Carbonari, G., Croce, F., Tossici, R. & Nobili, F. Anatase TiO₂ as a Cheap and Sustainable Buffering Filler for Silicon Nanoparticles in Lithium-Ion Battery Anodes. *Chemsuschem* **10**, 4771-4777 (2017).
 158. Lotfabad, E.M. et al. ALD TiO₂ coated silicon nanowires for lithium ion battery anodes with enhanced cycling stability and coulombic efficiency. *Physical Chemistry Chemical Physics* **15**, 13646-13657 (2013).
 159. Sushko, M.L., Rosso, K.M. & Liu, J. Mechanism of Li⁺/Electron Conductivity in Rutile and Anatase TiO₂ Nanoparticles. *Journal Of Physical Chemistry C* **114**, 20277-20283 (2010).
 160. Park, S.J., Kim, Y.J. & Lee, H. Synthesis of carbon-coated TiO₂ nanotubes for high-power lithium-ion batteries. *Journal of Power Sources* **196**, 5133-5137 (2011).

161. Yang, J.P. et al. Amorphous TiO₂ Shells: A Vital Elastic Buffering Layer on Silicon Nanoparticles for High-Performance and Safe Lithium Storage. *Advanced Materials* **29**, 1700523 (2017).
162. Ren, R. et al. Controllable Synthesis and Tunable Photocatalytic Properties of Ti(3+)-doped TiO₂. *Scientific Reports* **5**, 10714 (2015).
163. Eom, J.-Y et al. Black titanium oxide nanoarray electrodes for high rate Li-ion microbatteries. *Journal of Materials Chemistry A* **3**, 11183-11188 (2015).
164. Mehta, M. et al. Hydrogen treated anatase TiO₂: a new experimental approach and further insights from theory. *Journal of Materials Chemistry A* **4**, 2670-2681 (2016).
165. Wu, M.Y. et al. In Situ Formed Si Nanoparticle Network with Micron-Sized Si Particles for Lithium-Ion Battery Anodes. *Nano Letters* **13**, 5397-5402 (2013).
166. Chae, S. et al. Micron-sized Fe-Cu-Si ternary composite anodes for high energy Li-ion batteries. *Energy & Environmental Science* **9**, 1251-1257 (2016).
167. Ortiz, G.F. et al. Alternative Li-Ion Battery Electrode Based on Self-Organized Titania Nanotubes. *Chemistry Of Materials* **21**, 63-67 (2009).
168. Bin Wu, H., Lou, X.W. & Hng, H.H. Titania Nanosheets Hierarchically Assembled on Carbon Nanotubes as High-Rate Anodes for Lithium-Ion Batteries. *Chemistry-a European Journal* **18**, 3132-3135 (2012).
169. Ryu, W.H., Nam, D.H., Ko, Y.S., Kim, R.H. & Kwon, H.S. Electrochemical performance of a smooth and highly ordered TiO₂ nanotube electrode for Li-ion batteries. *Electrochimica Acta* **61**, 19-24 (2012).
170. Wang, M.S., Song, W.L. & Fan, L.Z. Interconnected TiO_x/carbon hybrid framework incorporated silicon for stable lithium ion battery anodes. *Journal of Materials Chemistry A* **3**, 12709-12717 (2015).
171. Tian, H.J., Tan, X.J., Xin, F.X., Wang, C.S. & Han, W.Q. Micro-sized nano-porous Si/C anodes for lithium ion batteries. *Nano Energy* **11**, 490-499 (2015).